Modeling Morphology Evolution for Nanostructured Electrochemical Systems

by

Stephen J. DeWitt

A dissertation submitted in partial fulfillment
of the requirements for the degree of
Doctor of Philosophy
(Applied Physics)
in The University of Michigan
2015

Doctoral Committee:

Associate Professor Katsuyo Thornton, Chair
Associate Professor Bart Bartlett
Professor John Kieffer
Professor Johannes Schwank
Professor Levi Thompson

For Sarah, my wonderful and patient wife

ACKNOWLEDGEMENTS

First, I would like to thank my advisor, Professor Katsuyo Thornton, for everything that she has done for me over the past six years, including teaching me to be a thorough and ethical researcher. I also appreciate that she trusted me enough to let me determine my own research project for the first four years of my graduate education, while still giving me enough guidance that I never got too far off track. I would also like to thank the members of my committee, Professor Bart Bartlett, Professor John Kieffer, Professor Johannes Schwank, and Professor Levi Thompson for all of their comments and suggestions regarding my work.

I am grateful for the many past and current members of the Thornton group, for their camaraderie and support over the years. I would especially like to thank Drs. Hui-Chia Yu, Hsun-Yi Chen, and Larry Aagesen for generously taking the time to answer the many questions I have asked them. I would also like to thank Dr. Raul Enrique for his comments on how to improve several of the sections in this dissertation.

This dissertation would not have been possible without the unceasing support of my family and friends. I would like to thank the friends I met during my time in graduate school, including Anna, Hakan, Tim, Ashley, Cyril, Matt, Monica, Rob,

Justin, and Jimmy, for their solidarity in the face of challenging days and the many good times we shared. I am thankful for the constant support, enthusiasm, and empathy of my in-laws, Steve and Kim Benoit. I am grateful to my parents for their unconditional love and for raising me to be the person I am today. Last, but certainly not least, I would like to thank my wife, Sarah, who has been at my side through this whole process, encouraging me every step of the way.

TABLE OF CONTENTS

LIST OF FIGURES

Figure

ABSTRACT

Modeling Morphology Evolution for Nanostructured Electrochemical Systems

by

Stephen J. DeWitt

Chair: Katsuyo Thornton

In this dissertation, we examine the morphological evolution of two nanostructured electrochemical systems, the growth of anodic alumina and the electrodeposition/electrodissolution of magnesium. These systems are investigated through one-dimensional and three-dimensional continuum simulations.

Anodic alumina films are grown through an electrochemical oxidation process, exhibiting morphologies including barrier films and nanoporous films. A new model of anodization is developed in which a thin space charge region forms at the oxide/electrolyte interface, explaining experimental observations of embedded interfacial charge. Ionic transport through the oxide is described through a newly proposed counter-site defect mechanism. A one-dimensional model is parameterized and validated using experimental data in the literature. Predictions of the embedded charge as a function of applied current density and electrolyte pH are presented. The model

is extended to multiple dimensions to simulate the growth of anodic nanopores. The simulations capture much of the experimental behavior for a range of applied potentials and electrolyte pH values. Most importantly, the simulated pore geometry is insensitive to the electrolyte pH, while still exhibiting the expected decreased growth rate for increasing pH. This improvement over previous models stems from the treatment of adsorbed oxygen and hydroxide species at the oxide/electrolyte interface.

The second system examined is the electrodeposition/electrodissolution of magnesium. A new model of electrodeposition and electrodissolution is developed, which incorporates Butler-Volmer kinetics, facet evolution, and dilute solution theory. Three-dimensional simulations of the growth of magnesium deposits yield in-plane and out-of-plane hexagonal plates, consistent with experimental observations. Simulations predict that the deposits become narrower and taller with increasing current density due to the depletion of the electrolyte concentration near the deposits. Increasing the distance between the deposits causes increased depletion of the electrolyte surrounding the deposit. Different morphologies after one deposition-dissolution cycle, a flatted-topped hexagonal pyramid and a hexagonal plate, are predicted for two types of orientation dependence for the dissolution reaction. These predictions can be tested experimentally to identify the mechanisms governing the morphological evolution of magnesium.

This work represents a step toward quantitatively predictive simulations of electrochemical systems through the development of improved models, their numerical implementation, and physical insights gained through simulations.

CHAPTER I

Introduction

1.1 General Background and Motivation

Electrochemical processes and technologies play an increasingly important role in modern society. Some of these electrochemical technologies are clearly visible in everyday life, such as the Li-ion batteries that power cell phones and laptop computers or corrosion, which costs the US economy approximately 3% of GDP each year.[1] However, other important electrochemical phenomena are less visible, like electrodeposited copper interconnects in computer chips. Electrochemical processes can also be used to transform sunlight into electricity or chemical fuel (photoelectrochemical cells), transform chemical fuel into electricity (fuel cells), sense gas concentrations (as in carbon monoxide detectors) or produce chemical species (as in the production of chlorine).[2,3]

In all of these instances, the fundamental electrochemical processes can be described in terms of the interactions between two electrodes, an electrolyte, and an external electrical circuit. A schematic diagram of an electrochemical cell can be found

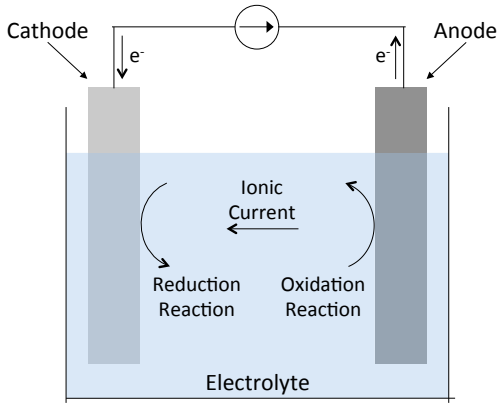

Figure 1.1: A schematic diagram of a generic two-electrode electrochemical cell.

in Fig. 1.1. Electrochemical reactions occur at the interface between the electrodes and the electrolyte. In an electrochemical cell, reduction and oxidation reactions occur on different electrodes. In a reduction reaction, electrons are transferred from the electrode to the reacting species in the electrolyte, while in an oxidation reaction, electrons are transferred from the reacting species in the electrolyte to the electrode.[2] The electrode where the reduction reaction takes place is called the cathode, and the electrode where the oxidation reaction takes place is called the anode. Electrons are mobile in the electrodes and external circuit, while only ions are mobile in the electrolyte. Because electrons cannot travel through the electrolyte, the electron generated by the reduction reaction travels through the external circuit and is consumed as part of the oxidation reaction, as is shown in Fig. 1.1. Ions in the electrolyte carry current through the electrolyte between the electrodes to complete the circuit.[2]

Even for electrochemical devices on the scale of centimeters to meters, the structure of the active components is often on the nanoscale, as shown in Fig. 1.2. Li-ion battery cathodes often consist of ceramic nanoparticles mixed with carbon

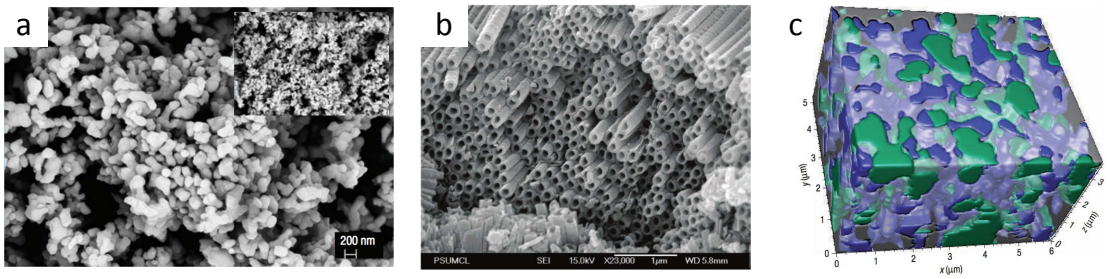

Figure 1.2: Examples of nanostructured electrochemical systems. (a) A Na_2FePO_4F Li-ion battery cathode, reproduced from Ref. 4. (b) Anodic TiO_2 nanotubes, reproduced from Ref. 5. (c) A reconstruction of a Ni-yttria-stabilized zirconia fuel cell anode where the Ni is shown in green, the yttria-stabilized zirconia is shown in gray, and pores are shown in blue, reproduced from Ref. 6.

nanoparticles and binder agents, as shown in Fig. 1.2a.[4,7] Anodic oxide films, grown through an electrochemical oxidation process called anodization, can self-organize into nanotubular structures with controllable feature sizes on the order of of tens of nanometers, as seen in Fig. 1.2b.[5] Figure 1.2c shows a 3D reconstruction of a typical Ni-yttria-stabilized zirconia (YSZ) fuel cell anode, where the complex morphology facilitates the transport of electrons, O^{2-} ions, and gaseous species.[6]

Because these active components are on the nanoscale, understanding and controlling electrochemical devices requires an understanding of the physical mechanisms occurring on the nanoscale. The electrochemical reaction rate varies along the electrode/electrolyte interface as a result of local variation of quantities such as the ion concentration in the electrolyte and the electric potential. These phenomena are intrinsically linked to the morphology of the electrodes and must be taken into account to understand, predict, and optimize the behavior of the cell.[8,9]

In many electrochemical processes, the electrode morphology itself evolves in time.

This morphological evolution can come from one of several sources. Species from the electrolyte can be deposited onto the electrode, as occurs during electrodeposition. Conversely, the electrode can be electrochemically dissolved, as in electropolishing. Species from the electrolyte can also react with the electrode material to form a new compound, as in anodization, where an oxide is grown on the electrode. Often, the objective of the electrochemical processing is to obtain a particular morphology. For example, in anodization, often a specific nanoporous or nanotubular structure is desired. A second example is for metal anodes for rechargeable batteries, the metal needs to be able to be deposited and dissolved over hundreds or thousands of cycles without forming deleterious structures such as dendrites that can short the cell.

Simulations are powerful tools for exploring and predicting phenomena in electrochemical systems that are difficult to observe experimentally. Simulations of electrochemical phenomena can be loosely separated into two categories: atomic simulations and continuum simulations. Atomistic simulations include density function theory (DFT) and molecular dynamics (MD) approaches, which provide detailed information regarding relatively small collections of atoms for either short periods of time (MD) or at a single point in time (DFT).[10] These approaches have been widely applied for simulations of electrochemical systems and can be used to screen potential electrode and electrolyte materials,[11,12] predict material structures,[13,14] determine transport parameters,[15] and understand reaction pathways.[16]

Continuum methods do not consider the discrete nature of atoms, but can be used to simulate systems with length scales above several nanometers and a wide range of time scales.[10] These length and time scales make continuum models attractive

for examining electrochemical nanostructural evolution. Continuum simulations typically require the solution of coupled partial differential equations. Solving partial differential equations requires the application of boundary conditions, which can be difficult for systems with complex or evolving boundaries. A common method to solve partial differential equations in a irregular domain is to use the finite element method with a body-fitted grid.[17] However, in an evolving domain, a body-fitted grid warps to account for interfacial motion, and therefore the domain must be continually remeshed to maintain numerical accuracy.[17] To avoid the computationally expensive process of continually remeshing the domain, several numerical methods for use on a fixed grid have been developed. These methods include: the immersed boundary method,[18] the immersed interface method,[17,19] the smoothed boundary method,[20,21] phase field methods,[22] and level set methods.[23] In the context of electrochemical simulations, the smoothed boundary method has been used to simulate the cycling of Li-ion battery cathodes.[9,24] Phase field methods have been used to model electrodeposition[25–28] and to model phase transformations within Li-ion battery cathodes[29,30] and anodes.[31] Level set methods have been applied to model electrodeposition[32] and electrochemical etching.[33]

1.2 Dissertation Overview

In this dissertation, we present models and simulation results for two electrochemical systems with evolving interfaces: the growth and self-ordering of anodic alumina nanopores and the cycling of magnesium battery anodes. Between these model systems, two different types of behavior are captured. The alumina film formed

on the aluminum substrate during anodization is an electronic insulator and the current through the film is carried by the ions of the film. Alternatively, for Mg battery anodes, the electrodeposited/dissolved Mg is an electronic conductor and thus becomes an extension of the metal anode. The development of methods to simulate these two systems would be applicable to a variety of other systems, including Li metal battery anodes, the electrodeposition of Cu for integrated circuit interconnects, and corrosion.

The primary objectives are similar for modeling and simulating these two electrochemical systems: to develop an improved model of the system that captures the essential experimental observations and to explore the connection between experimentally controllable parameters and the morphology of the electrochemically grown material. More detailed objectives for each system are based on the unique features of the systems and the pressing questions in each subfield, as described below.

The first example system discussed in this dissertation is the growth of anodic alumina films, where an aluminum substrate is electrochemically oxidized to form a layer of alumina on the substrate. Under certain anodizing conditions, the alumina film grows such that a self-ordered array of cylindrical pores run perpendicular to the surface of the substrate. These pores have feature sizes on the order of tens of nanometers with geometry that can be controlled by tailoring the anodizing conditions. The ordered, nanoscale features are attractive for a range of applications, particularly in energy conversion and storage. Several models have been developed to explain the growth and self-ordering of porous anodic alumina films, which have shed light on some of the mechanisms governing anodic oxide film growth, but many fundamental

questions remain. These questions include:

1. What is the role (if any) of space charge on the reaction rates and ionic transport?
2. What is the mechanism for ionic transport through the bulk oxide?
3. How can the experimental dependencies on the electrolyte pH be explained?
4. Can the reaction rates alone explain pore formation?

In this dissertation, we provide answers to each of these questions.

The second of the example systems treated in this dissertation is the electrodeposition and electrodissolution of magnesium for metallic magnesium battery anodes. Magnesium batteries are a promising alternative to Li-ion batteries due to their potential for higher volumetric energy density, safer operation, and lower cost.[34] In particular, while metallic lithium anodes are prone to dendrite formation, leading to failure of the battery, metallic magnesium anodes do not form dendrites. Instead, electrodeposited magnesium forms compact, faceted films, with grain sizes on the order of 1 μm.[35] Previous computational models have described electrodeposition, often using the phase-field or level set methods. However, none of these models are directly applicable to the magnesium anodes because they cannot describe the formation and evolution of the facets. The key questions this dissertation addresses regarding metallic magnesium battery anodes are:

1. Why does electrodeposited lithium form dendrites, but electrodeposited magnesium does not?
2. How do magnesium deposits evolve over the course of a deposition-dissolution cycle?

3. How can one model the evolution of the facets observed during the electrodeposition of magnesium?

The dissertation contains seven chapters: (I) Introduction, (II) Anodic Oxide Films: Background, (III) One-Dimensional Model for Anodic Film Growth on Aluminum with Coupled Bulk Transport and Interfacial Reactions, (IV) Multidimensional Extension of the Anodization Model and Simulations of Anodic Nanopore Growth Using the Smoothed Boundary and Level Set Methods, (V) Rechargeable Magnesium Batteries: Background, (VI) Phase-Field Model for the Electrodeposition and Electrodissolution of Magnesium, and (VII) Summary, Future Work, and Contributions.

Chapter II presents a review of anodic oxide film morphology, the mechanisms involved during film growth, the applications of anodic oxide films in energy conversion and storage, and previous models of anodic oxide film growth.

In Chapters III and IV, we present an improved model of the anodization of aluminum and apply it to address fundamental questions regarding the growth and self-ordering of anodic oxide nanostructures. Chapter III presents a one-dimensional (1D) model of anodic oxide film growth. In the model, a thin space charge region at the oxide/electrolyte interface couples the bulk ionic transport with the interfacial reactions. The model is parameterized and validated using experimental data from the literature. The model then is used to make predictions of the pH and current dependence of the charge trapped at the oxide/electrolyte interface after anodization is completed. This 1D model is extended to multiple dimensions in Chapter IV. The model is implemented numerically using the smoothed boundary and level set methods. The anodization model is shown to exhibit a preferred pore geometry, as

is expected from experiments. The simulated dependence of the geometry on the applied potential and electrolyte pH is found to agree well with experimental results from the literature. In particular, the pH dependence of the geometry is captured more accurately than in previous models.

Chapter V provides background on metallic magnesium batteries, with an emphasis on the morphology during the early stages of deposition. This chapter also discusses previous models of electrodeposition.

Chapter VI presents simulations of the electrodeposition and electrodissolution of magnesium on a noble substrate. A new model of electrodeposition is presented, which incorporates Butler-Volmer kinetics, facet evolution, a spatially varying potential in the electrolyte, and a time-dependent concentration in the electrolyte. The model is capable of describing the growth of the hexagonal plates observed experimentally. The deposit morphology and electrolyte concentration in the vicinity of the deposit are both shown to depend on the applied current density. Predictions of the deposit morphology after one deposition-dissolution cycle are presented, which would enable identification of the source of the orientation-dependent growth.

Chapter VII summarizes the research presented in the previous chapters and describes future directions of research that build on the modeling approaches and numerical frameworks developed in this dissertation. This chapter also discusses the ways in which this work contributes new knowledge to the field.

CHAPTER II

Anodic Oxide Films: Background

Anodic oxide films, formed by the electrochemical oxidation of a metal substrate, display a wide range of morphologies including compact barrier films, nanoporous films, nanotubular films, and more complex morphologies such as nanolace. The film grows as oxygen ions from the electrolyte react with the atoms from the metal substrate to form new oxide. The current is transported through the growing film by the combined migration of both metal and oxygen ions.

Anodization has been an important industrial process since the early 20th century.[36,37] Traditionally, anodic films have been utilized as the dielectric layer in electrolytic capacitors and to improve the corrosion resistance, abrasion resistance,

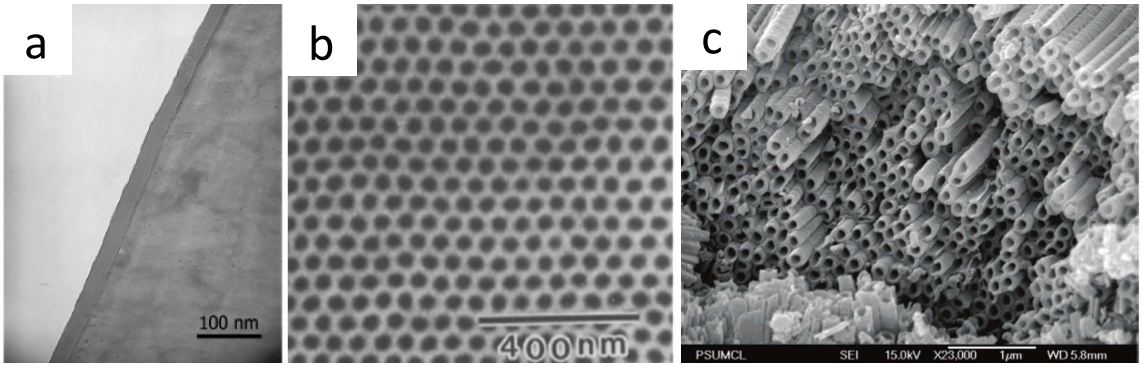

Figure 2.1: Typical anodic nanostructures: (a) cross section of a barrier film, reproduced from Ref. 40, (b) top-down view of a nanoporous film with the barrier layer etched away, reproduced Ref. 41, and (c) nanotubular film broken in half, reproduced from Ref. 5.

and dye absorption of metals.[36] Since the development of highly ordered anodic nanostructures in 1995,[38] anodic films have found an increasing range of possible applications. Especially promising are the applications of anodic films for energy generation and storage, such as in solar cells, batteries, and supercapacitors. Other applications include sensors, membranes, and medical devices.[39] In this chapter we present a brief summary of the anodic nanostructure morphologies, the mechanisms involved in anodic film growth, computational models of anodic nanostructure growth, and the energy applications of anodic nanostructures.

2.1 Experimental Morphologies

2.1.1 Barrier Films

The anodic oxide films with the simplest morphology are barrier films. As shown in Fig. 2.1a, barrier films are compact films that grow conformally on the substrate. These films can grow up to hundreds of nanometers thick, usually limited by the dielectric breakdown voltage of the oxide.[36] Anodic barrier films can form on a number of metallic substrates including Al, Fe, Hf, Nb, Ta, Ti, W, and Zr.[37] These films grow in electrolytes that do not form soluble complexes with the metal cations in the substrate, thus preventing the dissolution of the oxide at the oxide/electrolyte interface.[36] While the thin, compact nature of these films does not lend itself to applications in energy storage and generation, the simple geometry of barrier films provides a model system to examine the mechanisms governing anodization.

2.1.2 Nanoporous Films

Nanoporous anodic films exhibit cylindrical channels that extend from the film surface down toward the film/substrate interface, as seen in Fig. 2.1b. These films grow in electrolytes that form soluble complexes with the metal substrate cations. For example, nanoporous alumina films grow in a variety of acidic electrolytes, including chromic, oxalic, phosphoric, and sulfuric acids.[36] Other substrates that can yield nanoporous anodic films include Nb,[42] Ta,[43] W,[44] and Sn.[45]

Although porous aluminum oxide (PAO) films have been studied since the 1850s,[46] the first direct observation of the porous structure was by Keller, Hunter, and

Robinson in 1953.[47] The nanopores nucleate randomly across the substrate surface and eventually self-organize into a hexagonal array perpendicular to the plane of the substrate, yielding a porous structure that is disordered near the film surface (where the pores initially formed) but becomes ordered at some depth.[41,48]

In 1996, Masuda and Satoh pioneered a two-step anodization process to grow nanoporous films that are well ordered throughout the entire film.[49] In this process, the substrate is anodized until the pores are well ordered at the base of the film. The oxide is then dissolved, leaving behind a dimpled substrate surface. The substrate is then anodized a second time, and the growth of the pores is directed by the depressions in the substrate. The pores nucleate as a well-ordered array with the optimal inter-pore spacing and grow into straight pores oriented perpendicular to the substrate surface. In addition, nano-indentation[50] and a focused ion beam (FIB)[51] have been applied to direct the growth of the pores.

The geometry of the nanopores depends on the substrate material, the electrolyte, and the applied potential/applied current, as has been systematically examined by Friedman et al.[52] For ordered anodic alumina nanopores, the inter-pore spacing can range from 20 to 500 nm,[52,53] the pore diameters can range from 7 to 250 nm,[47,52–54] and the barrier thickness can range from 5 to 225 nm,[54,55] all of which increases approximately linearly with the applied potential.[52,55] The interpore spacing and pore diameter are essentially independent of the electrolyte pH.[52] The pore growth rate ranges between 0.1 and 16 nm/s and increases as the applied potential increases and as the pH decreases.[50–52] Nanoporous films can be much thicker than barrier films, up to 100 m thick.[56] The chemical (open-circuit) dissolution rate of the oxide

determines the maximum film thickness. The electrolyte slowly dissolves the walls of the growing pores, tapering them to a point. The maximum thickness is reached once the chemical dissolution at the top of the film matches the electrochemical growth at the base of the film.[57,58]

The morphologies of nanoporous films on other substrates have not been examined as comprehensively. Well-ordered nanoporous films on Ta and Nb and disordered nanoporous films on W and Sn have been reported, with pore feature sizes on the order of tens of nanometers.[42–45]

2.1.3 Nanotubular Films

Nanotubular films are another commonly observed anodic nanostructure. As seen in Fig. 2.1c, nanotubular films have a cylindrical central pore, like nanoporous films, but also have voids between the cells, separating the nanotubes from each other. As in nanoporous films, two-step anodization improves the ordering of the nanostructure.[59]

The first anodic nanotubular films were developed by Zwilling et al. in 1999 using Ti and a Ti-Al alloy as the substrates.[60] Since then nanotubular films have been grown on Zr,[61] Hf,[62] and Fe,[63] as well as a variety of alloy systems.[46] For these materials, F^- or Cl^- ions in the electrolyte are required to form soluble complexes with the substrate metal ions.[46,64]

For nanotubular films grown on Ti, Fe, Zr, or Hf substrates, typical pore diameters range from 15 to 150 nm with wall thicknesses between 10 and 30 nm and barrier thicknesses from 20 to 80 nm.[61–63,65–67] As in nanoporous alumina films, the pore diameter and barrier thickness has been shown to increase linearly with the applied

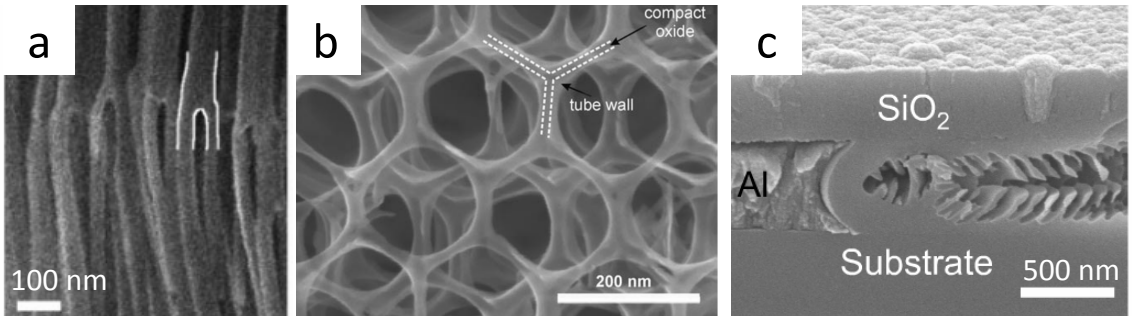

Figure 2.2: Examples of more complex anodic oxide nanostructures: (a) branched nanopores, reproduced from Ref. 69, (b) nanolace, reproduced from Ref. 70, (c) dendritic nanopores, reproduced Ref. 71.

potential.[65,67] The nanotube wall thickness is essentially independent of the applied potential.[65,66] Nanotubular titania films have been grown up to 1 mm in thickness,[68] enabled by the use of organic electrolytes with decreased chemical dissolution of the oxide.[58]

2.1.4 Films with More Complex Morphologies

Beyond the standard morphologies, films with more complex morphologies have been developed, including modulated-diameter structures, branched structures, nanobamboo, perforated nanopores, nanolace, dendritic nanopores, and pores with nonhexagonal lattices. Examples of these morphologies can be seen in Fig. 2.2. These morphologies can be generated by changing the potential during growth, by partially etching the film, by constraining the geometry during anodization, or by patterning the substrate surface before anodization. Nanoporous alumina films with periodically modulated pore diameters have been developed by switching between a low applied

potential and a high applied potential.[72] A similar approach can be applied to form nanobamboo structures.[70] A potential decrease by a factor of $1/\sqrt{n}$ during anodization causes each pore to split into n branches (see Fig. 2.2a).[69] By etching nanoporous films with modulated pore diameters, it is possible to generate morphologies such as periodically perforated nanopores[73] and nanolace (see Fig. 2.2b).[70] Nanopores with horizontal dendritic structures can be formed by anodizing Al inside an SiO_2 mask (see Fig. 2.2c).[71] Finally, FIB or nanoindentation prepatterning of the substrate to guide pore nucleation can yield pores with square or snowflake lattices.[51,72]

2.2 Mechanisms Governing Growth and Self-Organization

2.2.1 Fundamental Processes Governing Anodic Film Growth

The range of nanostructures described in the previous section is the result of the combination of several fundamental processes: reactions at both the oxide/electrolyte and metal/oxide interfaces, ionic transport through the oxide, stress generation and its effects, and space charge accumulation. Understanding these underlying processes and their interactions would enable further optimization of the morphologies and properties of anodic oxide films.

2.2.1.1 Interfacial Reactions

At the oxide/electrolyte interface, a series of simultaneous reactions occur, involving both O and metal species. These reactions result in O^{2-} ions entering the film from the electrolyte and in metal ion complexes such as TiF_6^{2-} exiting the film.[58,74]

For anodic alumina, the pathways for these reactions have been studied in detail by Våland and Heusler by measuring the pH-dependent reaction fluxes of O and Al species.[74] Anions from the electrolyte (e.g. PO_4^{3-}, F^-) can also react at the oxide/electrolyte interface and become incorporated into the film, comprising up to 14 wt.% of the film.[58,75] In contrast to the multiple reactions at the oxide/electrolyte interface, the reaction at the metal/oxide interface is much simpler. Metal atoms from the substrate react to become ions and then enter the oxide, which may combine with incoming oxygen ions to form a new oxide.[56]

2.2.1.2 Ionic Transport

Tracer experiments using implanted noble gas atoms indicate that anodic films grown on Al, Ti, Ta, Nb, and W substrates grow at both the oxide/electrolyte and metal/oxide interfaces, while films grown on Zr and Hf substrates only grow at the metal/oxide interface.[76–79] Thus, for most anodization systems, both anions and cations carry the current through the film. Experiments using isotopically labeled oxygen as well as an experiment with substrates consisting of layers of Nb and either Ta or Al indicate that all of the ions in the film participate in conduction, rather than isolated defects moving through an otherwise stationary lattice and that the ionic transport occurs through a series of short jumps.[80–82] Empirically, the ionic current follows an exponential relationship, known as the high-field transport equation,[36]

$$i = Aexp(BE) \tag{2.1}$$

which relates the current density to the applied electric field, E, by means of the temperature-dependent constants A and B. This empirical relationship has been interpreted as describing the motion of ions over a potential energy barrier.[83–85] In this case, $B(q_n a_n)/kT$, where the subscript n denotes the ionic species, q_n is the charge of the ion, $2a_n$ is the ionic jump distance, k is Boltzmann's constant, and T is the temperature. The total current density is then given by the sum of the partial current densities of each mobile species.

Experiments suggest that the anions and cations move through the film via a cooperative process, rather than through independent processes. The experimental values of B for anodized Al[86,87] yield $q_n a_n$ values that are much too high for a single ion hopping to an adjacent site on its sublattice.[88] Moreover, both oxygen and the metal carry a substantial fraction of the current over a wide range of applied electric fields,[76,78,79] which requires $q_n a_n$ to be similar for Al^{3+} and O^{2-} ions. However, this is unlikely given different ionic charge and the similar atomic spacings of Al^{3+} and O^{2-} ions in anodic alumina.[81] In response to this evidence against independent transport, several models of cooperative transport have been proposed.[89–91] In particular, the defect cluster model[89] resolves these issues by assuming that transport is facilitated by mobile defects that consist of both anions and cations, with an effective charge greater than the individual ions in the system. Further insight into the ionic transport mechanism can be achieved by a combination of atomistic simulations of ion transport and new, more accurate measurements of $i(E)$ and the fraction of the current carried by each ion for a range of current densities.

2.2.1.3 Stress Generation and its Effects

Stresses are generated inside the film during anodization, as has been documented for multiple material systems.[92–95] The stresses in the film can be separated into electrostriction, which is compressive and is only present while the current is applied, and the residual stresses, which remain in the film at the open circuit condition. The dependence of the residual stresses on the applied current has been studied extensively for anodized Al films.[93–95] The residual stresses are tensile at low current densities and compressive at high current densities, with a zero-stress transition point at approximately 4 mA/cm^2. This compressive shift has been attributed to the increased generation of new oxide within the oxide bulk (rather than at the interfaces) as the current density increases.[95] The stresses within the film have been linked to plastic flow from the nanopore/nanotube base to the nanopore/nanotube walls, which has been observed through the motion of W tracer atoms.[96]

2.2.1.4 Space Charge Accumulation

The consideration of space charge within anodic oxides is important both during and after anodization. Simulations have shown that space charge within the oxide can significantly affect ionic transport.[97,98] Space charge that is trapped in the film after anodization leads to a built-in electric field that may influence the behavior of anodic oxide nanostructures, especially in electronic applications.[99] The charge trapped in the oxide film after anodization can be calculated from measurements of the potential along the surface of the film.[40,100] The trapped charge, negative at the oxide/electrolyte interface and positive at the metal/oxide interface, is on the order

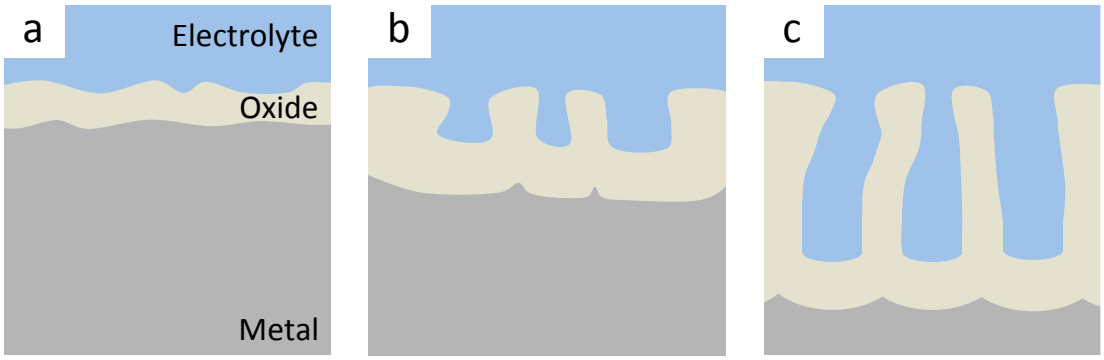

Figure 2.3: Schematic diagram of the three stages of anodic nanopore growth: (a) barrier formation, (b) pore initiation, and (c) steady state growth.

of 1×10^{12} e/cm^2 near each interface. The excess charge has been attributed to locally nonstoichiometric ratios between the metal and oxygen and stress-induced electron traps.[40,100]

2.2.2 Mechanisms Governing Anodic Nanostructure Self-Organization

Anodic nanopores/nanotubes grow in three stages: barrier formation, pore nucleation, and steady state growth, as seen in Fig. 2.3. During barrier formation, a nearly flat film grows on the substrate as a result of an oxide growth reaction at the metal/oxide interface and competing oxide growth and oxide dissolution reactions at the oxide/electrolyte interface. The rates of these reactions depend on the electric field. As the barrier forms, the film reaches a preferred thickness at which the growth rate at the metal/oxide interface matches the net dissolution rate at the oxide/electrolyte interface. As the barrier film approaches its preferred thickness, slight variations along the interfaces cause the current to focus on thin regions of the film. These

regions grow into the substrate more quickly than neighboring areas, leading to the formation of pore nuclei.[101–103] As the pore nuclei grow into the substrate, a larger fraction of the current passes through the pore regions, rather than the neighboring flat regions, until all of the current passes through the base of the pores. Eventually, interactions between the pores cause them to self-order and they reach the steady state growth stage, where an array of equally sized pores grows into the substrate at a constant velocity.[48,102–104]

The source of the interactions that cause the ordering process is an active area of research. One proposed source of the ordering is competitive growth due to the field-dependence of the interfacial reactions. Under this theory, the preferred pore geometry is the one that leads to an electric field that maximizes the pore growth rate. Through a competitive growth process, eventually only the pores with this preferred geometry remain.[102,103,105] However, this competition between growing pores may not be sufficient to explain the high degree of ordering and the limited window of applied potentials at which highly ordered structures can be attained.[71,106–108] Pore ordering may also be guided by repulsive forces due to volume expansion during oxide formation,[71,108] which is supported by experiments showing that stress applied to the substrate during anodization can suppress ordering.[109] The pore geometry has also been proposed to result from a balance between volume expansion at the metal/oxide interface and plastic flow away from the interface.[71,110] Stress-dependent reaction rates have also been proposed to guide pore ordering.[106,107,111]

For nanotubular films, the tubes separate from each other between pore nucleation and steady state growth due to preferential chemical dissolution of F^--rich oxide at

the cell edges.[58] The F^- ions segregate to the outer edges of the film because they travel through the oxide more quickly than the O^{2-} ions. Mechanical stresses at the junction between cells[105] and void formation to due ionic transport[112] have also been suggested as contributing factors to tube separation.

2.3 Computational Models of Anodic Oxide Films

Several models have been developed to describe the growth of nanoporous anodic alumina films, but none have been able to capture the full range of experimental behavior. Parkhutik and Shershulsky[102] developed an influential analytic model of steady-state pore growth, assuming the pore base to be a spherical cap. In this model, competing oxidation and dissolution reactions at the oxide/electrolyte interface were described by two Tafel expressions, the potential was calculated using Laplace's equation, and the reaction rate at the metal/oxide interface was calculated from current continuity. Thamida and Chang[103] developed a model closely related to that of Parkhutik and Shershulsky and calculated the fastest-growing steady-state geometry using a hodograph transformation technique, which allowed them to examine arbitrary geometries. They also applied linear stability analysis to study the initial stages of pore formation. Both the Parkhutik and Shershulsky and the Thamida and Chang models predict a linear relationship between the applied potential and the cell size and pore diameter, in accordance with experimental observations. However, both models also predict that that the cell size increases with increasing pH, which is in disagreement with the aforementioned experimental observations that the cell size is insensitive to electrolyte pH. Cheng and Ngan[104] performed two-dimensional

(2D) simulations of pore growth from templated substrates using a variant of the Thamida and Chang model. Unlike the calculations of the steady-state geometry for the pore base and the linear stability analysis calculations, the approach taken by Cheng and Ngan permits the direct simulation of the pore ordering process, from pore initiation to steady-state growth. Houser and Hebert developed an alternate model where the film growth is assumed to be primarily controlled by high-field ionic transport through the film, not by the reaction rates at the interfaces.[97,113] They conducted simulations of steady-state pore growth with a fixed geometry based on an experimental pore morphology, which indicated that the bulk space charge formation must be accounted for in the calculation of the potential, unlike the models mentioned previously. Houser and Hebert also simulated the effect of plastic flow during anodization,[113] supporting previous experimental evidence that oxide material flows from the barrier region to the pore walls.[110] A more detailed review of models and simulations for anodic nanostructure formation can be found in Ref. 114.

2.4 Applications for Energy Generation and Storage

2.4.1 Solar Cells

Anodic nanostructured films are promising materials for solar cells because their highly ordered, high-aspect-ratio geometry facilitates transport of photogenerated electrons and holes to their respective current collectors. Anodic nanostructured films have been investigated for use in a variety of solar cells, including dye-sensitized solar cells (DSSCs), photoelectrochemical cells (PECs), and solid-state organic solar

cells. In DSSCs, incoming photons are absorbed by dye molecules attached to the surface of the electrode, generating excited electrons. The dye transfers the excited electron to the semiconductor electrode, and then receives a replacement electron from a redox couple in the electrolyte. The photoanode is typically fabricated using compacted nanoparticulate TiO_2, with a maximum reported efficiency of 13%.[115] Anodic nanotubular TiO_2 offers the potential for improved performance because the nanotubes provide straight electron transport paths to the current collector, without the interparticle trap sites that slow electron transport for nanoparticulate films.[39,116] Beginning with the 2.9% solar conversion efficiency first reported in 2006,[117] the efficiency of nanotubular TiO_2-based DSSCs has been steadily increasing and is currently up to 9.8%.[118] Nanotubular electrodes have been shown to have lower electron recombination rates than nanoparticulate electrodes, as expected, but the transport times are not improved,[119] likely as a result of defects caused by F^- anions incorporated into the film from the electrolyte.[120] The elimination of these impurities provides a pathway to substantially improved performance of anodic nanotubular TiO_2 DSSCs. PAO templates have also been applied to build DSSCs with nanotubular TiO_2[121] although the resulting devices have shown lower efficiencies than those using anodized TiO_2.

Anodic nanostructures have also been applied for PECs, where the energy from absorbed photons is used to form a fuel such as H_2. The ideal photoelectrode for a PEC absorbs a large fraction of the solar spectrum, has good charge transfer and charge transport characteristics, and is stable in aqueous electrolytes. PECs based on GaAs/$GaInP_2$ photoelectrodes have efficiencies of up to 16.5%, but degrade

after one day of use.[122] TiO_2 photoelectrodes are stable and have sufficient charge transport properties, but the large band gap limits the theoretical efficiency to 2.2%.[123] However, anodic TiO_2 nanotubes can be doped with C to reduce the band gap, leading to efficiencies up to 8.5%.[65] Fe_2O_3-based photoelectrodes have a near-ideal band gap, but suffer from poor hole transport capability.[124] Fe_2O_3 nanotubes grown on PAO templates have reached efficiencies of up to 5%, where the thin walls of the nanotubes decrease the distance the holes must travel to reach the electrolyte, reducing recombination.[124] The photocurrent for these template nanotubes is among the highest reported photocurrents for hematite-based PECs and is much higher than reported values for anodized Fe_2O_3 nanotubes.[63,125,126] Tandem cells pairing a DSSC with the Fe_2O_3 photoelectrode may provide a route the higher efficiencies required for the widespread use of PECs.[122]

Beyond DSSCs and PECs, anodic nanostructures have also been used in organic solid-state solar cells. Anodic TiO_2 has been utilized as an electron acceptor in both standard bulk heterojunction and double bulk heterojunction solar cells, yielding efficiencies of up to 4.1%.[127,128] In addition to the straight path for electron transport provided by the nanotubular structure, the nanoscale confinement of the polymer orients its bonds for improved hole transport.[128] This confinement effect has also been explored for organic solar cells fabricated using PAO templates.[129]

2.4.2 Li-Ion Battery Anodes

Anodic TiO_2 and Fe_2O_3 nanostructures have been examined as Li-ion battery anodes, and PAO has been used as an anode template. The nanotubular morphologies

attainable through anodization enhance the kinetics of the anode. The thin nanotube wall enables high charge/discharge rates because it reduces the transport distance during intercalation/deintercalation.[130] Anodic nanostructures are especially promising for microbatteries, where their 3D nanostructure provides a much higher areal energy density than the traditional flat-film anodes.[131] Microbatteries have applications in fast-growing sectors such as implantable biomedical devices, microelectromechanical systems (MEMS), radio-frequency identification (RFID) chips, and miniaturized sensors.[131]

As a Li-ion battery anode, TiO_2 has three primary advantages: (1) a higher operating potential than the currently used carbon anodes, which decreases the risk of dendrite-induced catastrophic failure,[130,131] (2) a low volumetric change (on the order of 3%) during lithiation and delithiation, providing the opportunity for a long cycle life,[132] and (3) low cost and earth abundance.[133] Anodic nanotubular TiO_2 battery anodes were first studied by Liu et al. in 2008.[133] Since then, reversible capacities of up to 310 mAh/g[134] for pure TiO_2 and 350 mAh/g for TiO_2 covered with MnO_2 nanosheets[135] have been reported, which is competitive with the theoretical maximum capacity of carbon-based anodes, 372 mAh/g.[34] The coulombic efficiency of the TiO_2 anode has been shown to be nearly 100% up to very high charge/discharge rates of 32C and for over 1000 cycles.[134,136] Many investigations have focused on the crystal structure of the TiO_2 nanotubes, with mixed results on whether annealing improves[133] or degrades[130] the cyclability of the anode. Amorphous TiO_2 nanotubes can undergo an irreversible phase transformation to a face-centered-cubic phase during the first lithiation cycle, improving the capacity.[134] Nanotubes with smaller

feature sizes have been found to have better performance than those with larger feature sizes.[137] Besides MnO_2, other combinations of TiO_2 and other materials have been investigated, including anodic nanotubes grown from a Ti-Co alloy,[138] Fe_2O_3 deposited into TiO_2 nanotubes,[139] and either Al or Ni nanorods from a PAO template covered in TiO_2.[140,141]

Fe_2O_3 and Fe_3O_4 nanostructures fabricated using anodization have also been utilized as anodes for Li-ion batteries. Iron oxides are attractive materials for battery anodes due to a combination of low cost, high theoretical capacity (1005 mAh/g), and high electrical conductivity.[142,143] Li-ion battery anodes constructed purely from anodized Fe_2O_3 nanotubes (either amorphous or annealed into α-Fe_2O_3) have been shown to have poor cyclability.[142,144,145] Composite anodes that incorporate carbon species have been shown to significantly increase the capacity and cyclability of Fe_2O_3/Fe_3O_4 nanotubes.[142,144] For example, a Fe_2O_3/Fe_3C/graphene composite anode has been shown to have a reversible capacity of 1118 mAh/g at 0.17 C and 503 mAh/g at 6.6 C over 1000 cycles.[144] Cu nanorods fabricated using a porous anodic alumina template and then coated with Fe_3O_4 have been shown to have a stable reversible capacity above 800 mAh/g (presumably neglecting the mass of the Cu) for at least 50 cycles at C/8.[143]

2.4.3 Supercapacitors

Anodic nanostructures, mostly PAO templates, have also been used to fabricate supercapacitors. Supercapacitors are electrochemical energy storage devices that store energy in the electrochemical double layer and in some cases through pseudoca-

pacitance that involves redox reactions at the electrode surface.[146] The nanotubular and nanorod structures from anodic films improve supercapacitor performance by increasing the surface area of the electrodes and providing short, straight-line diffusion paths in the electrolyte.[147,148] The active material is also in direct electrical contact with the current collector, making conductive additives and binders unnecessary.[146] Traditional materials for supercapacitors include graphite, which has a limited specific capacitance of less than 400 F/g due to a lack of pseudocapacitance, and RuO_2, which can yield a large specific capacitance but is very expensive.[146,149]

Supercapacitors have been made from metal oxide, metal hydroxides, and conductive polymers using anodic nanostructures. Electrodes using anodic oxide nanostructures as the active material have specific capacitances below 220 F/g or areal capacitances below 15 mF/cm^2,[42,146,150,151] which are insufficient for practical applications. However, supercapacitors based on anodic-nanostructure templates exhibit much improved performance. An electrode made of PAO-templated RuO_2 has a reported specific capacitance of 1300 F/g.[147] RuO_2-coated TiO_2 nanotubes have also been investigated, but the mass of the TiO_2 leads to a lower specific capacitance of 620 F/g.[152] Non-Ru-based electrodes made of conductive polymers deposited into anodic nanostructure templates have also been investigated, with the best device having a specific capacitance that was nearly as high as the best RuO_2 electrode, 1142 F/g.[148] A CoO_4 nanotube electrode using a PAO template[153] has a reported specific capacitance of 574 F/g. NiO and Ni(OH)2 electrodes based on PAO templates[154] or deposited into TiO_2 nanotubes exhibited areal capacitances of up to 7,010 mF/cm^2.[154–156] MnO_2 electrodes templated by PAO or deposited into TiO_2

nanotubes have shown specific capacitances of up to 320 F/g and areal capacitances of up to 150 mF/cm^2.[133,150,157]

2.5 Role of Fundamental Investigations to Improve Performance in Energy Applications

Improved understanding of the fundamental mechanisms governing anodization provides a path for increased performance of anodic oxide films in energy generation and storage applications. To better predict and control the growth of anodic oxide films, a more complete understanding of the general mechanisms governing the anodization process is needed, particularly for the effects of plastic flow and the cooperative mechanism governing ionic transport through the oxide. Future experimental or computational investigations may also provide more specific insights into anodic oxide films that could be directly applied to improve device performance. Four promising areas for such insights are discussed below.

First, fundamental understanding of the role of impurities from the electrolyte in directing pore morphology and film properties must be developed. The effects of F^- ions from the electrolyte must be elucidated because they are responsible for the separation between nanotubes[58,62] and are believed to be recombination centers in solar cell applications.[120] Optimized control of the incorporation and transport of F^- ions during anodization may allow further control of the thickness of the nanotube walls and a decreased number of recombination centers. Second, more research is needed to understand the effect of embedded charge and the associated electric field on device performance, because it may alter the interfacial reaction

rates or the charge transport through the oxide. The embedded charge can be measured experimentally using electrostatic force microscopy or scanning Kelvin probe force microscopy, as in Refs. 158 and 159, or studied computationally using the approach described in Chapter III. Third, engineering the atomic-scale structure of anodic oxide films may lead to improved device performance, particularly for battery applications. Further investigations of the role of annealing and electrochemical phase transformations may provide insight into crystal structures that facilitate the intercalation and deintercalation processes. The approach taken in Ref. 134 to examine phase transitions in TiO_2 for Li-ion battery applications, combining synchrotron X-ray characterization techniques, molecular dynamics simulations, and density functional theory calculations, is particularly promising. Fourth, the continued development of high-surface-area anodic oxide morphologies, such as nanolace and dendritic nanopores, may lead to improvements in DSSCs and supercapacitors, where the electrode surface area is a primary determinant of device performance. In DSSCs, these high surface-area-morphologies may provide the high surface area found in nanoparticulate electrodes without the detrimental interparticle recombination centers.

2.6 Conclusion

Anodic oxide nanostructures provide a compelling mixture of high aspect ratios and highly ordered geometries with controllable features on the order of tens of nanometers. Fundamental research into the mechanisms governing anodic oxide growth may lead to new processing routes to gain further control of the properties and

morphology of these nanostructures. Despite much progress in understanding these governing mechanisms, many questions remain, particularly regarding the process of cooperative ionic conduction through the film and the role of stress in the self-ordering process.

Anodic oxide nanostructures have been investigated for a variety of applications, including solar cells, batteries, and supercapacitors, with promising results. However, further understanding of the formation and properties of anodic nanostructures is required to improve the performance of these devices. Such advances provide a path to commercial success of devices for energy storage and generation based on anodic nanostructures.

CHAPTER III

One-Dimensional Model for Anodic Film Growth on Aluminum with Coupled Bulk Transport and Interfacial Reactions

3.1 Introduction

In this chapter, we present a new one-dimensional model for anodic alumina growth, which couples bulk ionic transport to electrochemical reactions at the interfaces. The goal of this model is to provide an accurate description of the interfacial reaction kinetics while also capturing the effects of high-field transport within the film, embedded charge at the oxide/electrolyte interface, and the electric double-layer in the electrolyte. The model also provides a framework that easily extends to multidi-

mensional simulations of nanostructure ordering and could include other phenomena (e.g., impurities from the electrolyte, plastic flow). We parameterize and validate the model using experimental measurements of the aluminum-ejection current, the embedded charge density at the oxide/electrolyte interface, the steady-state pore barrier thickness, and the pore growth rate.

3.2 Model

The model presented here consists of three submodels: the submodel for the electric potential throughout the system, the submodel for ion transport within the film, and the submodel describing the chemical reactions at the oxide/electrolyte and metal/oxide interfaces. In this section, the three submodels are discussed in detail, followed by a discussion of the model parameters. In the interest of simplicity, we do not include effects due to mechanical stress or electrolyte species incorporated into the oxide. The impact of these effects is discussed in Section 3.5.

Before discussing the details of the model, we first define the terminology we use in describing the structure of the amorphous oxide. Oxygen and metal sites in Section 3.2.2 refer to locations where the short-range bond interactions favor either oxygen or metal ions, respectively, not positions in a periodic lattice of a crystalline material. In Section 3.2.3, pseudo-interstitials refer to ions that lead to concentration values exceeding those expected from the average film density. Likewise, pseudo-vacancies refer to ions that lead to concentration values below those expected from the average film density. While true interstitials and vacancies are point defects localized to specific sites, the pseudo-interstitials and pseudo-vacancies are not necessarily

localized and represent an excess or deficiency of the species which may be spread over multiple ion spacings.

3.2.1 Submodel for the Electric Potential

The electric potential distribution within the growing anodic film can be calculated using Poisson's equation and the Helmholtz double-layer model at the oxide/electrolyte interface.[160] During the anodization of aluminum, the substrate and bulk electrolyte can be approximated as ideal conductors, in which the potential is constant, and therefore nearly all of the potential drop occurs across the oxide film.[161] The distribution of the electric potential, ϕ, within the film is given by Poisson's equation

$$\frac{\partial^2 \phi}{\partial x^2} = -\frac{\rho}{\epsilon} \tag{3.1}$$

where the x-axis is oriented from the oxide/electrolyte interface to the metal/oxide interface, ρ is the charge density, and ϵ is the permittivity of the oxide film.

The potential within the bulk electrolyte is set to zero but it drops across the interfacial double-layer by an amount, η, which is the surface overpotential. The potential of the aluminum substrate is set to the applied potential, $\phi_{applied}$.

In concentrated electrolytes, including the electrolytes typically used during anodization, the interfacial double-layer behavior is dominated by the Helmholtz layer.[2] Therefore, the double-layer in the electrolyte can be modeled as a parallel-plate capacitor with capacitance $C_{Helmholtz}$ and with a uniform electric displacement field given by $D_{Helmholtz} = -C_{Helmholtz}\eta$.[162,163] Applying Gauss's law across the interface between the Helmholtz layer and the oxide, η can be expressed in terms of the electric

field at the interface on the oxide side:[160]

$$C_{Helmholtz}\eta - \epsilon \left.\frac{\partial \phi}{\partial x}\right|_{ox} = 0 \tag{3.2}$$

On the oxide side of the oxide/electrolyte interface, the space charge region is also closely confined to the interface. Due to the large concentration of charged species within the oxide, the Debye length, which typically characterizes the width of the space charge region,[84,160] is well below the atomic layer thickness. Therefore, similarly to the Helmholtz layer in the electrolyte, the space charge density in the oxide is confined to a single atomic layer at the interface, yielding a compact charge region. The ionic concentrations within this compact charge region are denoted by ${}_{ccr}c_{Al^{3+}}$ and ${}_{ccr}c_{O^{2-}}$, where subscripts on the left indicate the region of the variable (the compact charge region in this case). The electric field appearing in eq. (3.2) is the field at the edge of the compact charge region abutting the Helmholtz layer.

Due to the bulk charge neutrality and the approximately constant bulk oxide density, the ionic concentrations in the oxide outside of the compact charge region are also approximately constant with the values ${}^{eq}_{ox}c_{Al^{3+}}$ and ${}^{eq}_{ox}c_{O^{2-}}$. Outside the compact charge region, the right-hand side of 3.1 is zero and the electric field is given by

$$E_{bulk} = -\frac{\phi_{applied} - \phi_{ccr}}{L - l_{ccr}} \tag{3.3}$$

where, as can be seen in Fig. 3.1, ϕ_{ccr} is the value of ϕ at the boundary between the oxide bulk and the compact charge region, L is the thickness of the oxide, and l_{ccr} is the thickness of the compact charge region.

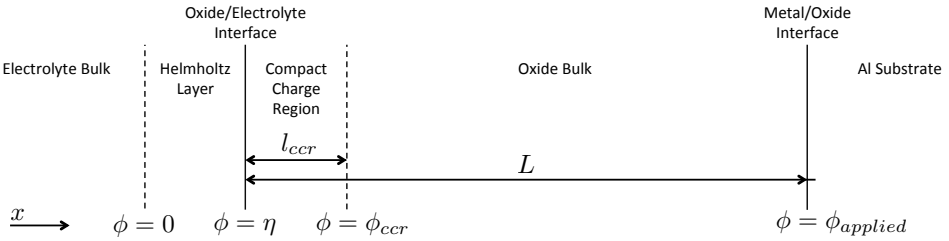

Figure 3.1: A schematic diagram of the model system, with the value of ϕ marked at key locations.

To find expressions for η and ϕ_{ccr}, eq. (3.1) is integrated across the compact charge region, with eqs. (3.2) and (3.3) providing boundary conditions

$$\eta = \frac{{}_{ccr}\rho l_{ccr}(L - \frac{l_{ccr}}{2}) + \epsilon\phi_{applied}}{\epsilon + C_{Helmholtz}L} \tag{3.4}$$

$$\phi_{ccr} = \frac{2\eta(\epsilon + C_{Helmholtz}l_{ccr}) - {}_{ccr}\rho l_{ccr}}{2\epsilon} \tag{3.5}$$

where ${}_{ccr}\rho = q_{Al^{3+}}{}_{ccr}c_{Al^{3+}} + q_{O^{2-}}{}_{ccr}c_{O^{2-}}$ is the charge density in the compact charge region and q_i is the charge of the ion i.

3.2.2 Submodel for Ionic Transport within the Film

The ionic current during anodization is known empirically to have the following exponential dependence on the applied electric field, E,

$$i = A\exp(BE) \tag{3.6}$$

where A and B are temperature dependent parameters.[164] Equation (3.6) is known as the high-field transport equation. Verwey[83] proposed that the exponential dependence

in eq. (3.6) is due to the field-dependent motion of ions over a potential barrier for an ionic hop in the bulk oxide[83,165] (although other explanations have also been proposed[84,166]). Based on this assumption, Fromhold developed the following continuum description of the ionic flux due to repeated ionic jumps driven by an applied electric field:[167]

$$J_i = -4a_i\nu_i \exp\left(\frac{-W_i}{kT}\right)\left[c_i \sinh\left(\frac{-q_i a_i}{kT}\frac{\partial\phi}{\partial x}\right) + a_i\frac{\partial c_i}{\partial x}\cosh\left(\frac{q_i a_i}{kT}\frac{\partial\phi}{\partial x}\right)\right] \qquad (3.7)$$

J_i is the ionic flux for the i^{th} species, a_i is half of the jump distance, ν_i is the jump attempt frequency related to atomic vibrations in the film, c_i is the concentration of species i, and W_i is the potential barrier height. For large applied fields and constant ionic concentrations, eq. (3.7) simplifies to eq. (3.6).

Although eq. (3.7) was originally conceived as a description of the transport of a single ion, experimental observations have provided evidence for a correlated ion transport mechanism. Tracer experiments have shown that the current is carried by both metal and oxygen ions during anodization of aluminum, niobium, tantalum, and tungsten.[168–172] Fromhold[173] noted that these results would be unlikely for a non-correlated transport mechanism. Due to the exponential dependence of the ionic fluxes on the potential barrier height in eq. (3.7), even a small difference in W_i would cause transport dominated by a single species.[173]

Experimental measurements of B, the field coefficient in eq. (3.6), provide further evidence of correlated ion transport. Harkness and Young[87] measured the average electric field during anodization as a function of the applied current and determined B to be 35 nm/V. According to eq. (3.7), for typical anodization conditions under

which the applied electric field is large and concentration gradient across the film is low, B is approximately equal to $q_i a_i/kT$. Assuming an average Al-Al spacing of 0.31 nm (a_i =0.16 nm) and an average O-O spacing of 0.28 nm (a_i =0.14 nm),[13] $q_i a_i/kT$ for one Al^{3+} ion moving one Al-Al spacing is 19 nm/V and for one O^{2-} ion moving one O-O spacing it is 11 nm/V. These field coefficients are much lower than the experimental value, implying that the primary transport mechanism is not individual ions moving single atomic spacings.

Several correlated ion motion mechanisms have been proposed,[81,89,91,173] including the hopon mechanism.[173] A hopon is a mobile defect where a metal ion is located on an oxygen site and an oxygen ion is located on a metal site. This defect travels by causing adjacent metal-oxygen pairs to exchange places as well, and one hop results in an effective charge of $q_{M^{n+}} - q_{O^{2-}}$ moving one metal-oxygen spacing. If two hopons are coupled, and share a central ion (Fromhold's "two-hopon process"[173]), the net effect is that a metal ion travels between adjacent oxygen sites, as shown in Fig. 3.2a. Conversely, an oxygen ion could travel between adjacent metal sites, but the oxygen ion's significantly larger ionic radius makes this case less likely. The coupled hopons are most visible in the second step of Fig. 3.2a, where two Al^{3+} ions on O^{2-} sites form hopons with an O^{2-} on an Al^{3+} site. Assuming an average Al-O spacing of 0.18 nm in the oxide,[13] $q_i a_i/kT$ for each of these steps is approximately 17 nm/V, which is well below the experimental value. Alternatively, if the hopons are coupled tightly enough, the combined motion of the hopons could face a single potential barrier, with the jump distance corresponding to the distance the defect travels after both steps. If such a tightly coupled hopon pair is traveling between oxygen sites in anodic alumina,

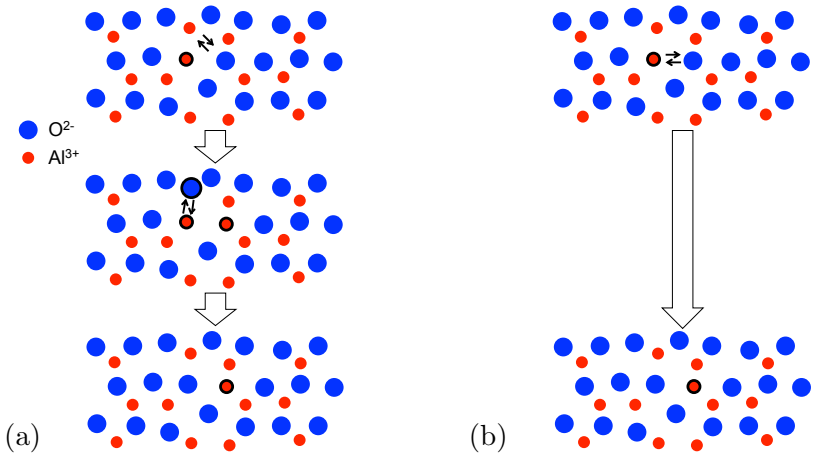

Figure 3.2: Schematic illustrations of a) the paired hopon and b) the counter-site defect transport mechanisms in two dimensions. In both mechanisms, an Al^{3+} ion on an O^{2-} site effectively exchanges locations with the O^{2-} ion to its right, propagating the excess charge to the right. The ions that are located on a site belonging to the other species are circled in black.

$q_i a_i/kT$ is 27 nm/V. This value is much closer to the experimental value than the single ion mechanisms.

We propose a related, but more direct transport mechanism than the two-hopon mechanism, the counter-site defect mechanism. Instead of two sequential aluminum-oxygen place-exchanges, the Al^{3+} ion on the O^{2-} site directly exchanges positions with an adjacent O^{2-} ion, as depicted schematically in Fig. 3.2b. Because the counter-site defect mechanism is a single-step mechanism, the single potential barrier framework can be applied directly. Unlike the coupled hopon mechanism, the counter-site defect mechanism does not require that O^{2-} ions be located on the smaller Al^{3+} ion sites. Since the motion of a multi-ion defect can also take the form of eq. (3.7),[173] the bulk

ionic flux due to the counter-site defect mechanism is given by

$$J_{Al^{3+}} = -J_{O^{2-}} = -J^0_{csd} \sinh\left(\frac{q_{csd} a_{csd} E_{bulk}}{kT}\right) \tag{3.8}$$

assuming a constant concentration of counter-site defects in the film, c_{csd}, and where $J^0_{csd} = 4 a_{csd} \nu_{csd} c_{csd} \exp\left(\frac{W_{csd}}{kT}\right)$. A positive flux corresponds to ion motion toward the metal/oxide interface. Equation (4.9) is fitted, with J^0_{csd} as a fitting parameter, and the calculated E values are within 4% of Harkness and Young's experimental results. The aluminum transport number, the fraction of the current carried by Al^{3+}, for this mechanism is a constant value of 0.6 across all current densities, which matches experimental results which showed that the transport number was 0.58±0.05 for current densities 0.1-10 mA/cm^2.[168] The transport number is also independent of the applied potential and electrolyte pH because it solely depends on the fraction of the defect charge due to an Al ion, $+3e$, out of a total defect charge, $+5e$ (including an O vacancy). Because eq. (4.9) is consistent with both the experimental current/field relation and the experimental transport numbers, it is used in our model.

The number of ions of each species within the system must be conserved. The evolution of the ion concentrations in the oxide is described by a continuity equation taking the form:

$$\frac{\partial c_i}{\partial t} = -\frac{\partial J_i}{\partial x} \tag{3.9}$$

In the oxide bulk, the ionic flux is spatially constant and the enforcement of eq. (4.10) is trivial. In the compact charge region, eq. (4.10) governs the evolution of ${}_{ccr}c_{Al^{3+}}$ and ${}_{ccr}c_{O^{2-}}$. For multidimensional simulations of anodic growth, the electric field

is no longer uniform in the oxide bulk, and eq. (4.10) must be solved within the entire domain to describe the formation and evolution of bulk space charge. As the oxide/electrolyte interface moves due to oxidation or dissolution, the compact charge region moves at the same velocity, $v_{o/e}$. To correct for this moving frame of reference, an advective term must be added to eq. (4.10). The evolution of the ion concentrations in the compact charge region are then given by

$$\frac{\partial_{ccr} c_i}{\partial t} = \frac{{}_{o/e}J_i - J_i}{l_{ccr}} - \frac{v_{o/e} c_{ox}^{eq} c_i}{l_{ccr}} \tag{3.10}$$

where ${}_{o/e}J_i$ is the flux into the compact charge region due to interfacial chemical reactions.

3.2.3 Submodel for Chemical Reactions at the Oxide/Electrolyte Interface

The goal of this subsection is to present the reaction mechanisms considered in our model and to derive equations for the oxidation/dissolution reaction rate, the reaction flux between the electrolyte and the compact charge region, the aluminum-species ejection flux, and the velocity of the oxide/electrolyte interface. In the process of these derivations, we obtain a set of equations that specifies the concentration of adsorbed species at the oxide/electrolyte interface. The approach taken here extends that of Våland and Heusler[174] for pH < 10. The experimentally observed change in the ejection mechanism in strongly alkaline electrolytes is not considered because neutral or acidic electrolytes are used for most applications of anodization.

The Våland-Heusler model describes the flux of aluminum species ($AlOH^{2+}$ and

$Al(OH)_2^+$) from the film into the electrolyte and the flux of oxygen ions from the electrolyte into the film. However, their model does not determine what portion of this ionic flux leads to interfacial motion. An influx of O^{2-} can either increase $c_{O^{2-}}$ near the interface or it can lead to the formation of new oxide. Similarly, an outflux of Al^{3+} can either decrease $c_{Al^{3+}}$ near the interface or lead to dissolution of the film. In order to determine what fraction of the flux contributes to interfacial motion, an oxidation/dissolution reaction must be explicitly considered:

$$2_{ad}Al^{3+} + 3_{ad}O^{2-} \rightleftharpoons {}_{ox}Al_2O_3 \tag{3.11}$$

where the subscripts on the left denote the location of the species, either in the adsorbed layer ("ad") or oxide ("ox"). In reaction (3.11), the reaction of adsorbed Al^{3+} with adsorbed O^{2-} leads to the creation of vacant anion and cation sites in the adsorbed layer. The concentration of these vacant adsorption sites are given by

$${}_{ad}c_{V_{anion}} = {}^{max}_{ad}c_{anion} - {}_{ad}c_{O^{2-}} - {}_{ad}c_{OH^-} \tag{3.12}$$

$${}_{ad}c_{V_{cation}} = {}^{max}_{ad}c_{cation} - {}_{ad}c_{Al^{3+}} - {}_{ad}c_{AlOH^{2+}} \tag{3.13}$$

where ${}^{max}_{ad}c_{anion}$ and ${}^{max}_{ad}c_{cation}$ are the number density of adsorption sites for anions and cations respectively. Section 4.4 describes how these sites are defined. The adsorbed OH^- and adsorbed O^{2-} are formed by the decomposition of water:

$${}_eH_2O \rightleftharpoons {}_{ad}OH^- + {}_eH^+ \tag{3.14}$$

$${}_{ad}OH^- \rightleftharpoons {}_{ad}O^{2-} + {}_eH^+ \tag{3.15}$$

In addition to the ion transfers described by reaction (3.11), we assume that Al^{3+} and O^{2-} ions can transfer between the oxide and the adsorbed layer without causing interfacial motion. These transfer reactions are separated into pseudo-interstitial and pseudo-vacancy processes. Local ion concentrations higher or lower than ${}^{eq}_{ox}c_i$ indicate the presence of pseudo-interstitial ions and pseudo-vacancies, respectively. The pseudo-interstitial concentration, ${}^{int}_{ccr}c_i$, and the pseudo-vacancy concentration, ${}_{ccr}c_{V_i}$, for species i are modeled as:

$$ {}^{int}_{ccr}c_i = max({}_{ccr}c_i - {}^{eq}_{ox}c_i, 0) \tag{3.16} $$

$$ {}_{ccr}c_{V_i} = max({}^{eq}_{ox}c_i - {}_{ccr}c_i, 0) \tag{3.17} $$

where $max(x, y)$ yields the larger value of x and y.

The following reactions describe the pseudo-interstitial and pseudo-vacancy reactions for each of the species present in the oxide:

$$ {}_{ad}O^{2-} \rightleftharpoons {}^{int}_{ox}O^{2-} \tag{3.18} $$

$$ {}_{ad}O^{2-} + {}_{ox}V_O^{2+} \rightleftharpoons {}_{ox}O^{2-} \tag{3.19} $$

$$ {}_{ad}Al^{3+} \rightleftharpoons {}^{int}_{ox}Al^{3+} \tag{3.20} $$

$$ {}_{ad}Al^{3+} + {}_{ox}V_{Al}^{3-} \rightleftharpoons {}_{ox}Al^{3+} \tag{3.21} $$

Experiments using ^{18}O tracers have shown that nearly all of the oxygen that enters the film is retained within the film,[175] which may appear to conflict with the dissolution reaction described by reaction (3.11). However, reactions (3.18) and (3.19)

provide a mechanism for O^{2-} that is sent to the adsorbed layer through reaction (3.11) to re-enter the film. Given the flux of O^{2-} from the adsorbed layer into the oxide, which is required by eq (4.9), most of the adsorbed O^{2-} would be expected to re-enter the film rather than entering the electrolyte through reactions (3.14) and (3.15).

The final reactions, describe the formation and ejection of adsorbed $AlOH^{2+}$:

$$ {}_{ad}Al^{3+} + {}_{ad}OH^{-} \rightleftharpoons {}_{ad}AlOH^{2+} \tag{3.22} $$

$$ {}_{ad}AlOH^{2+} \rightarrow {}_{e}AlOH^{2+} \tag{3.23} $$

Reaction (3.23) is assumed to be irreversible[174] because the concentration of $AlOH^{2+}$ in the electrolyte is sufficiently low such that diffusion removes the dissolved ions on a time scale much faster than the reaction rate. To reduce the number of species that are explicitly tracked in the adsorbed layer, we assume that the back reaction in reaction (3.22) is favored such that ${}_{ad}c_{AlOH^{2+}}$ is low and therefore negligible in the calculation of the vacant cation sites in the adsorbed layer in eq (3.13), i.e., that ${}_{ad}c_{V_{cation}} \approx {}^{max}_{ad}c_{cation} - {}_{ad}c_{Al^{3+}}$.

Rate equations and equilibrium concentrations can be found by applying Butler-Volmer kinetics to reactions (3.11), (3.14), (3.15) and (3.18) to (3.23). Reaction (3.11) yields the oxidation/dissolution rate per unit area,

$$ R_{oxidation} = k^{+}_{ox}({}_{ad}c_{Al^{3+}})^2({}_{ad}c_{O^{2-}})^3 - k^{-}_{ox}({}_{ccr}c_{Al^{3+}})^2({}_{ccr}c_{O^{2-}})^3({}_{ad}c_{V_{cation}})^2({}_{ad}c_{V_{anion}})^3 \tag{3.24} $$

where k^{+}_{ox} and k^{-}_{ox} are the forward and backward rate constants for reaction (3.11). The reaction order for eq (4.13) is determined from the stoichiometry of reaction (3.11),

reflecting the assumption that the reaction requires three O^{2-} and two Al^{3+} for substantial interfacial motion. The reaction order would be different if there are intermediate reactions that occur much faster than the other reactions. However, in the absence of experimental data suggesting a lower reaction order, we assume that the reaction order reflects the stoichiometry.

The velocity of the oxide/electrolyte interface is given by the oxidation reaction rate multiplied by the volume of oxide created,

$$ {}_{o/e}v = \frac{\Omega_{oxide} R_{oxidation}}{N_A}, \tag{3.25} $$

where Ω_{oxide} is the molar volume of the oxide and N_A is Avogadro's constant.

Reactions (3.14) and (3.15) are fast electrochemical reactions that are assumed to be at equilibrium.[174] By setting the forward reaction rate equal to the backward reaction rate, the equilibrium concentrations of adsorbed OH^- and adsorbed O^{2-} are determined to be

$$ {}_{ad}c_{OH^-} = \frac{{}_{ad}K_{OH\,ad}c_{V_{anion}}}{{}_{e}c_{H^+}} \exp\left(\frac{e\eta}{kT}\right) \tag{3.26} $$

$$ {}_{ad}c_{O^{2-}} = \frac{{}_{ad}K_{O\,ad}c_{OH^-}}{{}_{e}c_{H^+}} \exp\left(\frac{e\eta}{kT}\right) \tag{3.27} $$

where ${}_{ad}K_{OH}$ and ${}_{ad}K_{O}$ are equilibrium constants (given by the ratio of the forward and backward reaction constants), ${}_{e}c_{H^+}$ is the concentration of H^+ in the electrolyte, and e is the elementary charge. The dependence of ${}_{ad}c_{O^{2-}}$ and ${}_{ad}c_{OH^-}$ on η and electrolyte pH can be observed in Fig. 3.3. Vacancies in the adsorbed layer are favored at low η, adsorbed OH^- is favored for intermediate η, and adsorbed O^{2-} is

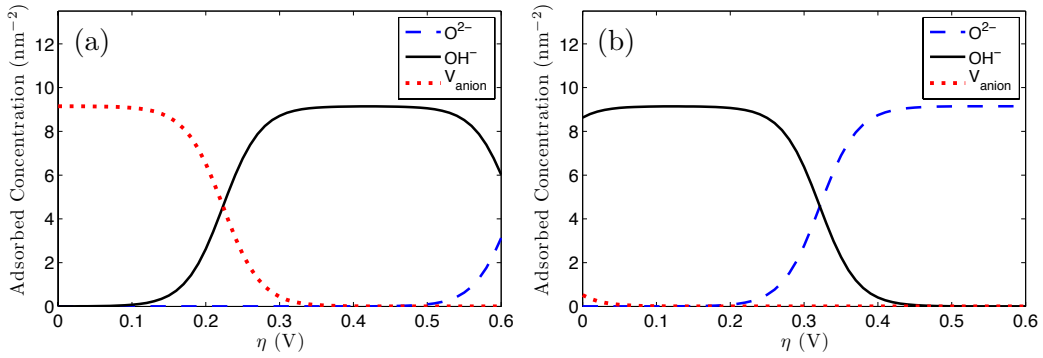

Figure 3.3: The concentrations of O^{2-}, OH^-, and vacant anion sites in the adsorbed layer as a function of the surface overpotential for electrolyte pH values of (a) 2 and (b) 7.

favored for high η. Fig. 3.3 also shows that increasing the electrolyte pH decreases the overpotential necessary to form adsorbed O^{2-} and OH^-.

Reactions (3.18) and (3.19) can be combined to find the flux of O^{2-} transferring from the adsorbed layer into the oxide without moving the interface

$$J_{O^{2-}transfer} = k^+_{O_{vac}} {}_{ad}c_{O^{2-}} {}_{ccr}c_{V_O^{2-}} + k^+_{O_{int}} {}_{ad}c_{O^{2-}} - k^-_{O_{vac}} {}_{ccr}c_{O^{2-}} {}_{ad}c_{V_{anion}} - k^- {}^{int}_{O_{int}} {}_{ccr}c_{O^{2-}} {}_{ad}c_{V_{anion}} \quad (3.28)$$

where $k^+_{O_{int}}$ and $k^-_{O_{int}}$ are the forward and backward reaction constants for the pseudo-interstitial ion transfer reactions and $k^+_{O_{vac}}$ and $k^-_{O_{vac}}$ are the forward and backward reaction constants for the pseudo-vacancy transfer reactions.

The aluminum transfer flux from the adsorbed layer to the oxide can be found in

a similar manner, yielding

$$J_{Al^{3+}transfer} = k^{+}_{Al_{vac}}{}^{ad}c_{Al^{3+}}{}^{ccr}c_{V_Al^{3+}} + k^{+}_{Al_{int}}{}^{ad}c_{Al^{3+}} - k^{-}_{Al_{vac}}{}^{ccr}c_{Al^{3+}}{}^{ad}c_{V_{cation}} - k^{-}_{Al_{int}}{}^{int}_{ccr}c_{Al^{3+}}{}^{ad}c_{V_{cation}} \quad (3.29)$$

where, similar to reaction (4.14), $k^{+}_{Al_{int}}$ and $k^{-}_{Al_{int}}$ are the reaction constants for the pseudo-interstitial transfer reactions and $k^{+}_{Al_{vac}}$ and $k^{-}_{Al_{vac}}$ are reaction constants for the pseudo-vacancy transfer reactions.

The $AlOH^{2+}$ ejection flux is determined by reactions (3.22) and (3.23), where reaction (3.22) is a fast chemical reaction, and reaction (3.23) taken as the rate-limiting electrochemical reaction.[174] The ejection flux is then given by

$$J_{AlOH^{2+}ejection} = k_{eject}\frac{{}^{ad}c_{Al^{3+}}{}^{ad}c_{OH^-}}{{}^{ad}c_{V_{anion}}}\exp\left(\frac{\gamma e\eta}{kT}\right) \quad (3.30)$$

where γ is the effective charge transfer coefficient for reaction (3.23).

The flux from the adsorbed layer to the compact charge region from eq (3.10), ${}_{o/e}J_i$, is given by the sum of the flux due to the oxidation/dissolution reaction and the ion transfer flux:

$${}_{o/e}J_{O^{2-}} = 3R_{oxidation} + J_{O^{2-}transfer} \quad (3.31)$$

$${}_{o/e}J_{Al^{3+}} = 2R_{oxidation} + J_{Al^{3+}transfer} \quad (3.32)$$

The change in ${}_{ad}c_{Al^{3+}}$ is calculated based on ${}_{o/e}J_{Al^{3+}}$ and the ejection flux:

$$\frac{\partial {}_{ad}c_{Al^{3+}}}{\partial t} = -{}_{o/e}J_{Al^{3+}} - J_{AlOH^{2+}ejection} \tag{3.33}$$

In summary, the oxide/electrolyte reactions submodel is specified by the fluxes at the oxide/electrolyte interface (eqs (3.31) and (3.32)), the concentration evolution equations (eqs (3.10) and (4.12)), the equilibrium concentrations (eqs (4.16) and (4.17)), the Al-species ejection rate (eq (3.30)), and the interfacial velocity (eq (4.18)).

3.2.4 Submodel for Chemical Reactions at the Metal/Oxide Interface

In contrast to the complex series of reactions at the oxide/electrolyte interface, the processes at the metal/oxide interface are much simpler. The only reaction is the irreversible oxidation of the metal substrate,

$$2_m Al + 3_{ox}O^{2-} \rightarrow {}_{ox}Al_2O_3 + 3_m e^- \tag{3.34}$$

where the subscript m represents species in the metal substrate. Due to the high exchange current density for reaction (3.34),[176] the overpotential at this interface is small and thus one can model the reaction rate to be limited by the incoming flux of oxygen ions,[177–180] in place of a Butler-Volmer expression. The velocity at the

metal/oxide interface is therefore given by:

$$ {}_{m/o}v = \frac{2\Omega_{oxide} J_{O^{2-}}}{3N_A} \tag{3.35} $$

Any O^{2-} transported to the metal/oxide interface forms new oxide. Thus, in the moving reference frame of the interface, the boundary condition at the metal/oxide interface for the O^{2-} concentration is zero flux. We assume that the Al^{3+} concentration at the interface is constant at ${}^{eq}_{ox}c_{Al^{3+}}$.

3.2.5 Model Parameters

The values of the simulation parameters used in this study are can be found in Table 3.1 and include direct experimental values,[87,174,181,182] molecular dynamics simulation results,[13] and estimations using relevant experimental data.[159,174,183–185] The values for $C_{Helmholtz}$ and ϵ are taken directly from experiments. The values of Ω_{oxide}, ${}^{eq}_{ox}c_{O^{2-}}$, and ${}^{eq}_{ox}c_{Al^{3+}}$ are calculated using an alumina density of 3.1 g/cm^3.[182] The maximum adsorbed anion concentration, ${}^{max}_{ad}c_{anion}$, is calculated assuming the oxygen ions form a (0001) hexagonal close-packed surface with an oxygen nearest neighbor distance of 0.28 nm.[13] The value of ${}^{max}_{ad}c_{cation}$ is then calculated assuming electroneutrality. The aluminum-ejection transfer coefficient, γ, is taken from Våland and Heusler's results[174] and, due to a change in notation, it is a value of unity smaller than their value.

The jump distance for the counter-site defect mechanism, $2a_{csd}$, is taken to be the oxygen nearest neighbor distance. The effective defect charge, q_{csd}, is $5e$. The flux coefficient J^0_{csd} is determined by fitting eq (4.9) to the data in Ref. 87. These

Table 3.1: Model Parameters

Oxide Constants:

$C_{Helmholtz}$	50e-20 F/nm	Ref. 181
ϵ	9.8 ϵ_0	Ref. 87
Ω_{oxide}	3.3e22 nm^3/mol	Ref. 182
${}^{eq}_{ox}c_{O^{2-}}$	55 nm^{-3}	
${}^{eq}_{ox}c_{Al^{3+}}$	37 nm^{-3}	
${}^{max}_{ad}c_{anion}$	9.15 nm^{-2}	
${}^{max}_{ad}c_{cation}$	6.10 nm^{-2}	
a_{csd}	0.14 nm	
q_{csd}	$5e$	
J^0_{csd}	2.54e-8 nm^{-2}	
l_{ccr}	0.28 nm	
T	298 K	

Reaction Constants:

γ	0.35	Ref. 174
${}_{ad}K_O$	2.2e-13 nm^{-2}	
${}_{ad}K_{OH}$	1.0e-6 nm^{-2}	
k^+_{ox}	5.0e6 nm^8 s^{-1}	
k^-_{ox}	2.0e9 nm^{18} s^{-1}	
k_{eject}	1.0e-5 s^{-1}	
$k^+_{O_{vac}}$	1.0e5 nm^3 s^{-1}	
$k^-_{O_{vac}}$	0	
$k^+_{O_{int}}$	0	
$k^-_{O_{int}}$	4.5e4 nm^3 s^{-1}	
$k^+_{Al_{vac}}$	6.45 nm^3 s^{-1}	
$k^-_{Al_{vac}}$	2.97e4 nm^3 s^{-1}	
$k^+_{Al_{int}}$	0	
$k^-_{Al_{int}}$	1.0e5 nm^3 s^{-1}	

Computational Parameters:

$\delta i_{galvanostatic}$	1.0e-5 mA/cm^2
Δ t	5.0e-6 - 5.0e-9 s

assumptions were discussed in detail in Section 3.2.2.

As discussed in Section 3.2.1, the compact charge is limited to a single atomic layer at the oxide/electrolyte interface, the last ionic hop site. The thickness of the compact charge region, l_{ccr}, is therefore taken to be the jump distance, $2a_{csd}$.

The values for the equilibrium constants ${}_{ad}K_{OH}$ and ${}_{ad}K_{O}$ are chosen to match the experimentally observed pH value of 9.1 for the point of zero charge[183] and nearly complete OH^- adsorption at pH 7.[184] No direct experimental data is available for the reaction constants in eqs (3.30) and (4.13) to (4.15), and thus the values are estimated by comparing the simulation results to three sets of experimental data. These sets of data are aluminum-ejection current data taken from Ref. 174, the embedded charge at the oxide/electrolyte interface from Ref. 159, and the steady-state barrier thickness for porous films at pH 1.1 and 30 V from Ref. 185. Further discussion of these parameterizations is provided in Section 6.4.

3.3 Computational Methods

To simulate the anodic growth of alumina, the model equations are discretized in time with time step, Δt. At each time step, the values of η and E_{bulk} are recalculated from eqs (3.3) and (4.8). Updated values of J_i, ${}_{o/e}J_i$, ${}_{ad}c_{OH^-}$, ${}_{ad}c_{O^{2-}}$, ${}_{ad}c_{V_{anion}}$, ${}_{ad}c_{V_{cation}}$, and $R_{oxidation}$ are then calculated. The explicit forward Euler method is used to discretize eqs (3.10) and (4.12) to update ${}_{ccr}c_{Al^{3+}}$, ${}_{ccr}c_{O^{2-}}$, and ${}_{ad}c_{Al^{3+}}$. The discretized

forms of these equations are

$$ {}_{ccr}c_i^{n+1} = {}_{ccr}c_i^n + \Delta t \frac{({}_{o/e}J_i^n - J_i^n)}{l_{ccr}} - {}_{o/e}v_{ox}^{eq} c_i \tag{3.36} $$

$$ {}_{ad}c_{Al^{3+}}^{n+1} = {}_{ad}c_{Al^{3+}}^n - \Delta t(J_{Al^{3+}transfer}^n + J_{Al^{3+}ejection}^n) \tag{3.37} $$

where the superscript n represents the current time step and $n+1$ represents the upcoming time step. At the end of each time step, the locations of the oxide/electrolyte and metal/oxide interfaces, ${}_{o/e}x$ and ${}_{m/o}x$, are advanced by ${}_{o/e}v\Delta t$ and ${}_{m/o}v\Delta t$ respectively. These positions are used to update L.

Both potentiostatic and galvanostatic simulations are implemented. For potentiostatic simulations $\phi_{applied}$ is simply set to the desired potential. For galvanostatic simulations, $\phi_{applied}$ is set such that the current at the metal/oxide interface equals the desired current, $i_{applied}$. In this case, $\phi_{applied}$ is determined at each time step using the bisection method such that the current is within a specified tolerance, $\delta i_{galvanostatic}$, of $i_{applied}$. This tolerance is chosen such that any variation in the current is negligible. The value of the time step, Δt, is chosen to ensure both accuracy and stability. The stability of the numerical method decreases with decreasing electrolyte pH because the decreased pH increases the $AlOH^{2+}$ ejection rate. Therefore, Δt is decreased for simulations at low pH. The values of $\delta i_{galvanostatic}$ and Δt that are used in our simulations are given in Table 3.1.

3.4 Results and Analysis

3.4.1 Overall Dynamics of Anodization

During galvanostatic anodization, the system undergoes a short transient period as the ionic concentrations at the oxide/electrolyte interface evolve toward their steady-state values. Differences in the bulk and reaction fluxes lead to the formation of a compact charge region near the oxide/electrolyte interface. The charge in the compact charge region drives the reaction flux toward balancing the bulk flux. After the initial transient, the surface overpotential, interfacial concentrations, reaction rates, and ionic fluxes reach constant values, with only the applied potential and interface locations changing in time. For potentiostatic anodization, after the initial transient, the surface overpotential, interfacial concentrations, reaction rates, and ionic fluxes continue to evolve as L, and thus E_{bulk}, changes. In both cases, the value of η varies based on the anodization conditions, but is on the order of 100 mV, within the range plotted in Fig. 3.3.

3.4.2 Aluminum-Ejection Current

Våland and Heusler's work provides the partial current due to the ejection of aluminum species and the partial current due to O^{2-} incorporation across a wide range of applied current and pH values.[174] In the course of these experiments, they found that porous films, rather than barrier films, develop for pH values below 4.63 and that there is a change in the dominant aluminum-species ejection mechanism near pH 10. In highly alkaline electrolytes, they determined that the ejected aluminum

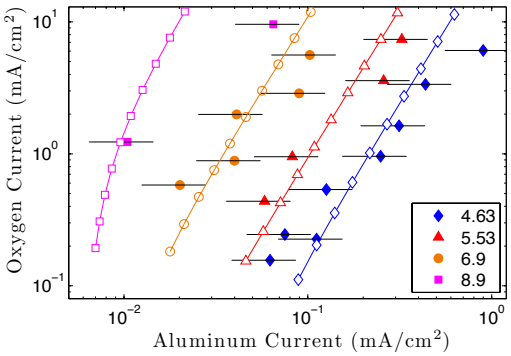

Figure 3.4: The O^{2-} partial current at the oxide/electrolyte interface vs. the Al^{3+} partial current at the oxide/electrolyte interface for pH values of 4.63, 5.53, 6.90, and 8.90 and $i_{applied}$ 0.2-12.0 mA/cm^2. The solid lines and hollow markers are simulated results and the solid markers are experimental results from Ref. 174.

species changes from $AlOH^{2+}$ to $Al(OH)_2^+$.

In light of these findings, the reaction constants are parameterized using the experimental results at pH 4.63, pH 5.53, and pH 6.9, where the film is non-porous and the non-highly-alkaline ejection mechanism is dominant. As illustrated in Fig. 3.4, the parameterized simulation results at pH 5.53 and 6.9 match the experimental results within the experimental uncertainty, as expected. At pH 4.63, the simulation results are mostly within the experimental uncertainty, but fall slightly outside the experimental data for high and low Al^{3+} partial current values. The experimental uncertainty in the data in Fig. 3.4 is $\pm 38\%$, estimated by twice the standard deviation of the relative difference between the data points and a linear trend line (covering 95% of a normal distribution).

Figure 3.4 also presents simulated data at pH 8.9, which matches the experimental result when the applied current is 1.2 mA/cm^2. However, at high applied current, the simulated Al^{3+} partial current is substantially lower than the corresponding

experimental value. This discrepancy in the ejection current is consistent with the experimentally observed change in the ejection mechanism, where the highly alkaline ejection mechanism accounts for the missing ejection current.

3.4.3 Embedded Charge at the Oxide/Electrolyte Interface

The embedded charge density at the oxide/electrolyte interface, given by ${}_{o/e}\sigma = 2_{ccr}\rho a_{csd}$, provides another key quantity with which the model can be parameterized. In measurements performed by Lambert et al.,[159] the surface charge density for anodic alumina grown galvanostatically at 5 mA/cm^2 in a 7 pH electrolyte was determined to be -1.3×10^{12} e/cm^2. They also found that the surface charge density increases in magnitude to -2.1×10^{12} e/cm^2 if the current is allowed to potentiostatically decay to from 5 mA/cm^2 to 0.05 mA/cm^2. The values of the charge densities must be modified from Ref. 159 to reflect an anodic alumina relative permittivity value of 9.8, as used elsewhere in the simulations, rather than the value of 8.0 used in their calculation. The modified values of ${}_{o/e}\sigma$ are -1.6×10^{12} e/cm^2 at 5 mA/cm^2 and -2.6×10^{12} e/cm^2 at 0.05 mA/cm^2.

In order to reproduce these experimental results, we perform a simulation where $i_{applied}$ is fixed at 5 mA/cm^2 until the potential reaches 40 V. At this point, $\phi_{applied}$ is held at 40 V until the current decreases below 0.05 mA/cm^2. The reaction constants for the model are chosen such that the simulated ${}_{o/e}\sigma$ matches the experimental galvanostatic value during the galvanostatic phase and also matches the experimental potentiostatic value when the current, i, has decreased to 0.05 mA/cm^2.

The simulated evolution of ${}_{o/e}\sigma$ for galvanostatic anodization followed by potentio-

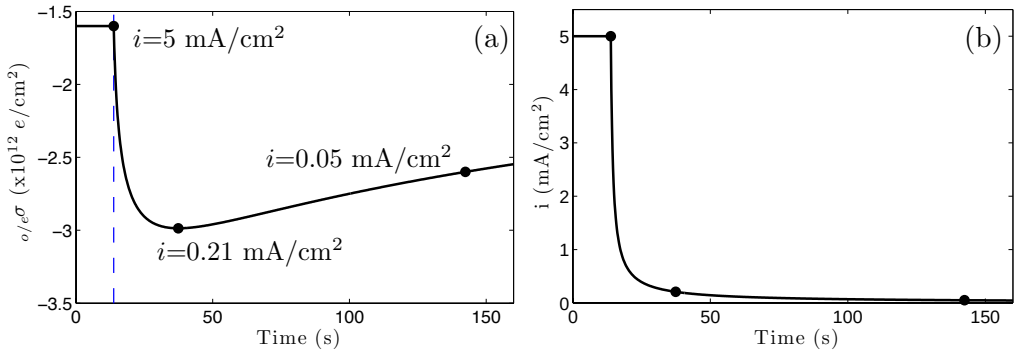

Figure 3.5: (a) The embedded charge at the oxide/electrolyte interface as a function of time during mixed galvanostatic/potentiostatic anodization. The growth conditions switch from galvanostatic anodization at 5 mA/cm^2 to potentiostatic anodization at 40 V after 14 s, marked by the vertical dashed line. The current decays to 0.05 mA/cm^2 after 142 s. (b) The current during the simulation.

static current decay is shown in Fig. 3.5a and the corresponding evolution of i is shown in Fig. 3.5b. The magnitude of ${}_{o/e}\sigma$ increases quickly after the switch to potentiostatic anodization and then slowly decays as the current drops. The maximum magnitude of ${}_{o/e}\sigma$, -3.0$\times 10^{12} e$/cm^2, is achieved after 37 s, when i equals 0.21 mA/cm^2.

Once parameterized, the model can predict the behavior of the embedded charge density where experimental data are not available. As can be observed in Fig. 3.6a, the model predicts that ${}_{o/e}\sigma$ monotonically decreases with increasing pH when $i_{applied}$ is held constant at 5mA/cm^2. As the pH increases, the concentrations of adsorbed OH^- and adsorbed O^{2-} increase and thus a lower η value is needed for the oxidation and the aluminum-ejection reactions, reactions (4.13) and (3.30), respectively, to balance the bulk fluxes. By eq (4.8), this lower value of η leads to a decrease in ${}_{o/e}\sigma$.

As shown in Fig. 3.6b, the model predicts that the embedded charge during galvanostatic anodization in an electrolyte with pH 7 attains its maximum magnitude

at 0.21 mA/cm^2. This behavior can be explained as follows. Both ${}_{ccr}c_{O^{2-}}$ and ${}_{ccr}c_{Al^{3+}}$ continuously decrease as the applied current density increases. Below 0.21 mA/cm^2, the loss of O^{2-} outpaces the loss of Al^{3+}. On the other hand, above 0.21 mA/cm^2, the loss of Al^{3+} outpaces the loss of O^{2-}.

Interestingly, Fig. 3.6b also reveals that ${}_{o/e}\sigma$ as a function of i is identical for both galvanostatic anodization and the potentiostatic phase of mixed galvanostatic/potentiostatic anodization. This result implies that E_{bulk} varies slowly enough during potentiostatic anodization that, at any given moment, ${}_{o/e}\sigma$ is at its steady-state value for a given i, and would not change if the current was held constant at that value indefinitely. The value of ${}_{o/e}\sigma$ in this regime is thus solely determined by the instantaneous value of i. It does not exhibit any dependence on $\phi_{applied}$ or the history of i. Therefore, the increase in $|{}_{o/e}\sigma|$ from pure galvanostatic to mixed galvanostatic/potentiostatic anodization in Ref. 159 is due to the change in i and is not due to transient behavior associated with potentiostatic anodization.

3.4.4 Pore Barrier Thickness and Pore Growth Rate

Our model can also be applied to the barrier portion of a porous film (the pore base), under the approximation that the film at the center of the pore base is flat and that the pore is deep enough that the potential drop in the pore walls is negligible. Under this approximation, we only simulate the phenomena occurring at the center of the pore and do not describe the accumulation of oxide in the pore walls. In order for this model to exhibit stable pore growth in two or three dimensions, the forward reaction (oxidation) in reaction (3.11) must dominate at the base of the pore when

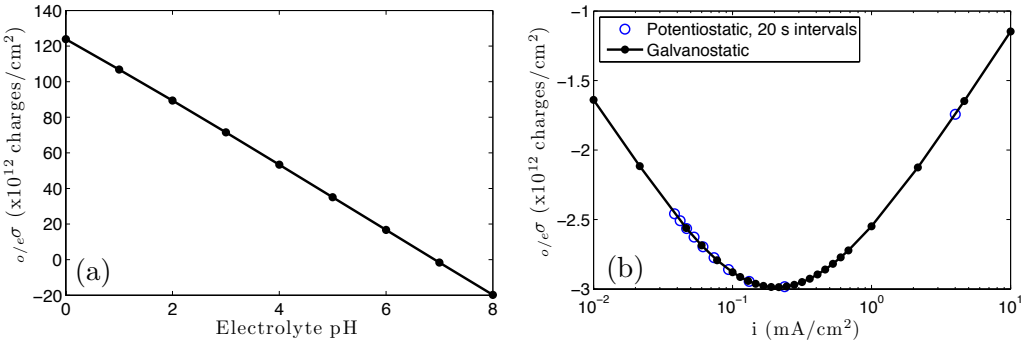

Figure 3.6: (a) The embedded surface charge at the oxide/electrolyte interface for pH between 0 and 8, when $i_{applied}$ is equal to 5 mA/cm^2. (b) The embedded surface charge at the oxide/electrolyte interface as a function of $i_{applied}$ for a pH 7 electrolyte. The solid markers represent $_{o/e}\sigma$ during galvanostatic anodization over a range of $i_{applied}$. The hollow markers represent $_{o/e}\sigma$ during the potentiostatic decay from Fig. 3.5a, sampled every 20 s.

the pore barrier is thin and the back reaction (dissolution) must dominate at the base of the pore when the pore barrier is thick. In a one dimensional simulation this feedback effect leads to a steady-state film thickness where the net dissolution rate at the oxide/electrolyte interface matches the oxidation rate at the metal/oxide interface.

The simulated steady-state film thickness for three pH levels is shown in Fig. 3.7a along with experimental pore barrier thickness data from Ebihara, Takahashi, and Nagayama.[185] The experimental results at 30 V and pH 1.1 are used to select the value of k_{eject} and the remaining experimental results are used for validation. As in the experimental data, the simulated barrier thickness increases with increasing applied potential with essentially no pH dependence. The simulated pore barrier thickness is linear with the applied potential, with a slope of approximately 1.2 nm/V. In contrast, the experimental pore barrier thickness exhibits nonlinearity with

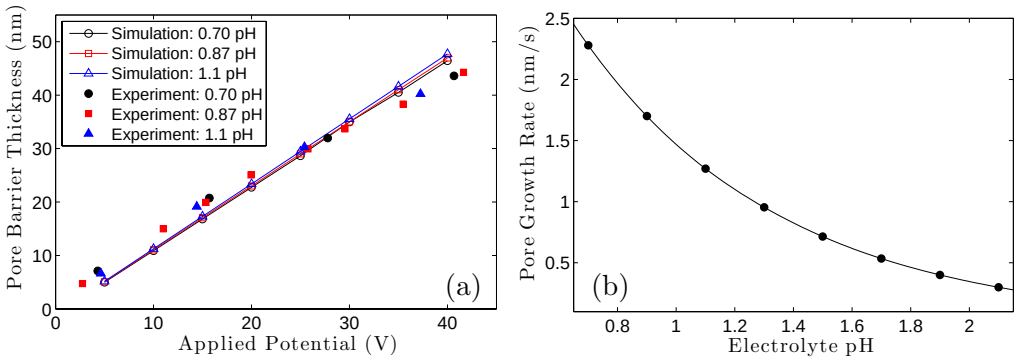

Figure 3.7: a) The steady-state pore barrier thickness vs. the applied potential. The experimental data was extracted from Ref. 185. b) The simulated steady-state pore growth rate as a function of electrolyte pH for $\phi_{applied} = 20$ V. The simulation results for other $\phi_{applied}$ are identical.

a slope of approximately 1.2 nm/V below 20 V and 0.88 nm/V above 20 V. This change in the experimental slope is likely related to lateral geometric changes in the pore: as the applied potential increases, the interpore spacing increases faster than the pore diameter.[185] Furthermore, smaller pores have larger curvature at the pore base, reducing the accuracy of the flat-film approximation for low applied potentials. Neither of these geometric effects can be captured by our one-dimensional simulation.

Although the electrolyte pH has little effect on the simulated steady-state pore barrier thickness, the pH substantially impacts the simulated pore growth rate, as observed in Fig. 3.7b. Both the magnitude of the growth rate and the trend that the growth rate decreases as the electrolyte pH increases are consistent with the experimental results reported by Friedman, Brittain, and Menon.[186] However, while these authors also find that the porous film growth rate increases as the applied potential increases,[186] our model yields growth rates that are independent of the applied potentials. The potential-dependent growth rate observed in the experiment

is likely caused by potential-dependent geometric changes, such as the ratio of the interpore spacing to the pore diameter discussed earlier, and therefore is not accounted for in a one-dimensional model.

3.5 Discussion

As observed in Section 6.4, our model captures a range of experimental behavior. However, the model does not currently account for a few experimental observations: the incorporation of electrolyte species into the film, embedded charge at the metal/oxide interface, and the impact of mechanical stress. In this section, we discuss the implications of these phenomena, as well as ways in which they could be incorporated into the model. After discussing the current limitations of the model, we propose new experiments and simulations to confirm and refine the mechanisms and parameters in our model.

The model does not account for the incorporation of electrolyte species into the film, but the framework is easily extensible to account for it. This can be accomplished by introducing the reactions necessary for the adsorption and incorporation of electrolyte species to the reactions in our model. The transport of electrolyte species can be handled using eqs (3.7) and (4.10). Migrating electrolyte species are particularly important when simulating the growth of TiO_2 nanotubes, where incorporated F^- is believed to play a significant role.[187]

Electrostatic force microscopy and Kelvin probe force microscopy experiments[158,159] indicate that positive charge is embedded at the metal/oxide interface. Due to the transport-limited formulation of reaction (3.34), no space charge region is assumed to

form at the metal/oxide interface in the present model. The model could be easily modified to include a separate metal/oxide reaction term to allow the build-up of Al^{3+} pseudo-interstitials or O^{2-} pseudo-vacancies. However, the effect on the growth behavior would be minimal because, unlike at the oxide/electrolyte interface, there are no competing reactions.

Mechanical stress has also been observed during the growth of anodic films[188] and may play a role in the self-organization of anodic nanostructures.[96,178] Under the counter-site defect transport mechanism, five moles of Al metal are consumed for every mole of Al_2O_3 generated at the metal/oxide interface. Assuming the molar volumes of Al and Al_2O_3 are 9.99 cm^3/mol and 32.9 cm^3/mol, the new Al_2O_3 only occupies 66% of the Al it replaces. Thus, a significant tensile stress could be expected at the metal/oxide interface and could be incorporated into our model in a manner similar to Ref. 179.

New experiments and atomistic simulations could resolve experimental uncertainties in the ionic transport parameters and provide further validation of the counter-site defect mechanism. Experiments utilizing ^{18}O tracers indicate that ionic transport is a result of many microscopic jumps, as is assumed in the counter-site defect mechanism, for barrier films on both aluminum[80] and tantalum substrates.[165] However, similar tracer experiments for porous film growth[189,190] provide possible evidence for "easy path" conduction via small channels or voids in the oxide. Further experiments are needed to determine if easy path conduction occurs in porous films, and if so, the conditions under which the transport mechanism changes.

The most comprehensive experimental data for B in eq (3.6)[86,87] report signifi-

cantly different values, 34 nm/V and 48-54 nm/V. A more accurate measurement of B could provide further evidence for or against the counter-site defect mechanism. Although the counter-site defect mechanism's Al transport number is consistent with the results in Ref. 168 for one of the electrolytes studied, transport numbers in the literature[168–172] have a wide range of values and behavior. Definitive measurements of the Al transport number for a range of applied current densities would provide more information about the nature of ion transport.

Alternatively, the validity of the counter-site defect mechanism could be tested using molecular dynamics simulations. In particular, although the counter-site defect mechanism and the tightly coupled hopon mechanism are experimentally indistinguishable, a molecular dynamics simulation would be able to distinguish between a one-step process (the counter-site defect mechanism) and a two-step process (the hopon mechanism).

The model parameters determined during the parameterization of our model are not unique. In particular, some freedom exists in selecting the value of k_{ox}^{-}, when k_{eject} and $k_{Al_{vac}}^{-}$ are also changed. Alternate values of these parameters influence the simulated pore growth rate (where larger k_{ox}^{-} values lead to higher growth rates) without substantially impacting the other simulated behavior. Two-dimensional simulations of pore growth, where a more accurate comparison of simulated and experimental pore growth rates is possible, can provide uniquely determined parameters.

The predicted behavior of the embedded charge with respect to the solution pH and the applied current in Fig. 3.6 provides an opportunity for further validation of our model. This experimental data can be obtained using electrostatic force

microscopy or Kelvin probe force microscopy, which to the best of our knowledge does not exist.

3.6 Conclusion

We have presented a new model of anodic film growth that encompasses high-field ionic transport in the oxide bulk and Butler-Volmer reaction kinetics at the oxide/electrolyte interface. These two processes are coupled by a thin space charge region, the compact charge region, at the oxide/electrolyte interface. The counter-site defect mechanism has been proposed as a new mechanism for cooperative ionic transport through the oxide bulk. Experimental results for the aluminum-ejection current, the embedded charge at the oxide/electrolyte interface, and the pore barrier thickness were used to parameterize the model for constants that were not available in the literature.

The model predicts yet unexamined behavior of the embedded charge for varied applied current densities and electrolyte pH. We find that potentiostatic anodization yields the same embedded charge density as galvanostatic anodization at the same current. Moreover, the model exhibits the self-stabilizing oxidation/dissolution feedback loop associated with the growth of anodic nanopores. The simulated steady-state pore barrier thickness matches experimental results for varied applied potential and pH. The simulated pore growth rate is consistent with experimental observations, both in terms of magnitude and trend with varied pH. This ability to capture the effect of the electrolyte pH on the aluminum-ejection current and the pore growth rate without changing the pore geometry (as measured by the pore barrier thickness)

resolves an inconsistency between previous predictions and experiments.[106,161,180,186,191] Based on the success of the model in these one-dimensional simulations, it can now be applied in multidimensional simulations to study the self-organization of anodic nanostructures.

A predictive simulation of anodic film growth would accelerate the progress of designing optimized growth conditions for desired film qualities. This work provides an improved understanding of the mechanisms underlying anodization and a significant step in the development of a predictive anodization simulation.

CHAPTER IV

Multidimensional Extension of the Anodization Model and Simulations of Anodic Nanopore Growth Using the Smoothed Boundary and Level Set Methods

4.1 Introduction

A multidimensional extension of the 1D model in Chapter III could be used to simulate the time evolution of pore formation to gain insight into the mechanisms responsible for pore ordering. However, while moving interface problems are relatively straightforward in 1D, efficiently solving partial differential equations on complex, evolving interfaces presents a computational challenge.[19] The smoothed boundary and level set methods provide a framework for efficient calculations on dynamic interfaces in two and three dimensions. The smoothed boundary method is a diffuse interface method for applying boundary conditions on an arbitrarily shaped

boundaries using a fixed grid[21] and has been applied to systems ranging from Li-ion battery intercalation/deintercalation[192] to selective area epitaxy.[193,194] The level set method is a technique to define and track interfacial motion and has been used in a variety of applications including electrodeposition, combustion, and semiconductor processing.[23,195] These two methods can be used in conjunction: the level set method to define and evolve the interfaces and the smoothed boundary method to solve partial differential equations with boundary conditions imposed at the interfaces.[196] These techniques permit the solution of the model equations on a fixed grid even though the interfacial locations move as the pores grow, eliminating the computationally expensive remeshing process needed for a body-fitted grid.[17]

In this chapter, we present multidimensional simulations of pore growth in anodic alumina based on the model developed in the previous chapter. In Section 6.2, we describe the necessary modifications to the 1D model to extend it to multiple dimensions. Section 4.3 describes the numerical implementation of the model using the smoothed boundary and level set methods. In Section 4.4, we present the parameters used in our simulations. Section 6.4 presents the simulated pore geometry and the growth rate as a function of the applied potential and the electrolyte pH. In Section 4.6, we discuss the insights the simulations yield regarding the mechanisms controlling pore growth and describe possible extensions of the model.

4.2 Model

The 1D model, upon which the multidimensional model of anodization in this work is built, can be separated into three coupled submodels describing: (1) the

electric potential, (2) the ionic transport within the film, and (3) the interfacial reactions. In the following section, we describe each of these submodels and the necessary changes for extension to multiple dimensions. Note that, while anodic oxides are amorphous, in the following section we apply the terminology associated with crystalline solids, including vacancies, interstitials, and maximum site densities, to reflect the short-range order that exists in these systems.

The electric potential submodel describes the electric potential within the film and the Helmholtz layer in the electrolyte. In this submodel, three changes are made to the 1D model: the derivatives are changed to vector derivatives, space charge is allowed to accumulate in the bulk oxide, and an effective boundary condition at the oxide/electrolyte (o/e) interface is formulated to include the effects of the Helmholtz layer in the electrolyte and the compact charge layer in the oxide, which replaces the analytic formulation available in the 1D case.

The electric potential within the film, ϕ, is given by Poisson's equation

$$\nabla^2 \phi = -\frac{\rho}{\epsilon} \tag{4.1}$$

where ϵ is the permittivity of the oxide and $\rho = q_{Al^{3+}} c_{Al^{3+}} + q_{O^{2-}} c_{O^{2-}}$ is the charge density in terms of the concentrations of O^{2-} and Al^{3+} in the bulk oxide, $c_{O^{2-}}$ and $c_{Al^{3+}}$, respectively. The value of ϕ at the metal/oxide (m/o) interface is set to ϕ_{app}. ϕ_{app} is assumed to be uniformly zero in the bulk electrolyte. As in Chapter III, the potential drop in the diffuse part of the double layer is assumed to be negligible and the Helmholtz layer is modeled as a parallel-plate capacitor. Thus, the boundary

condition for ϕ between the Helmholtz layer and the oxide is given by

$$C_{Helmholtz}\eta - \epsilon \left.\frac{\partial \phi}{\partial n}\right|_{o/e} = 0 \tag{4.2}$$

where $C_{Helmholtz}$ is the capacitance of the Helmholtz layer, and η is the value of ϕ at the interface between the oxide and the Helmholtz layer. The derivative of ϕ in the oxide infinitesimally close to the o/e interface, taken along the normal of the o/e interface pointing from the oxide toward the electrolyte, is given by $\left.\frac{\partial \phi}{\partial n}\right|_{o/e}$. Please note that while this is a slight change in notation from Chapter III, where $\left.\frac{\partial \phi}{\partial n}\right|_{o/e}$ was referred to as $\left.\frac{\partial \phi}{\partial n}\right|_{ox}$, no change has been made to this equation.

From Chapter III, a thin space charge region known as the compact charge region (CCR) exists at the o/e interface to couple the bulk ionic transport and the interfacial reactions. In Chapter III, the 1D geometry permitted an analytic solution for eqs (4.1) and (4.2). However, for multidimensional calculations, we now derive an effective Robin boundary condition for eq (4.1) at the CCR/bulk oxide boundary. Integration of eq (4.1) across the CCR, assuming uniform charge within the CCR and using eq (4.2), yields the following boundary condition at the CCR/bulk oxide boundary

$$\left.\frac{\partial \phi}{\partial n}\right|_{CCR} = \frac{C_{Helmholtz}}{l_{CCR}C_{Helmholtz} + \epsilon}\phi_{CCR} - \frac{{}_{CCR}\rho l_{CCR}}{2l_{CCR}C_{Helmholtz} + 2\epsilon} - \frac{{}_{CCR}\rho l_{CCR}}{2\epsilon} \tag{4.3}$$

where $\partial\phi/\partial n|_{CCR}$ is the derivative of ϕ in the oxide bulk, taken along the normal of the CCR/bulk oxide boundary and infinitesimally close to the CCR/bulk oxide boundary, ϕ_{CCR} is the value of ϕ at the CCR/bulk boundary, and l_{CCR} is the thickness of the CCR. The charge within the CCR is given by ${}_{CCR}\rho = q_{Al^{3+}}\ {}_{CCR}c_{Al^{3+}} + q_{O^{2-}}\ {}_{CCR}c_{O^{2-}}$,

where q_i is the charge of ion i (either O^{2-} or Al^{3+}) and ${}_{CCR}c_i$ is the concentration of ion i (noted by the subscript on the right) in the CCR (interfacial concentrations and velocities have their location denoted by the subscript on the left). Due to the thin nature of the CCR, we approximate it as an infinitesimally thin region, and thus ${}_{CCR}c_i$ is treated as an interfacial quantity. See the Supporting Information for the derivation of eq (4.3).

Equation (4.3) can be derived by solving eq (4.1) in the CCR. If the distance across the CCR is given by x, with $x(0)$ being the interface between the Helmholtz layer in the electrolyte and the CCR, and $x(l_{CCR})$ is the boundary between the CCR and the oxide bulk, integration of eq (4.1) across the CCR yields:

$$\phi(x) = -Ax - B - \frac{{}_{CCR}\rho}{2\epsilon}x^2 \tag{4.4}$$

For unknown constants A and B. Given that $\phi(0) = \eta$ and $\phi(l_{CCR}) = \phi_{CCR}$, eq (4.4) becomes

$$\phi(x) = -\frac{{}_{CCR}\rho}{2\epsilon}x^2 + \frac{\phi_{CCR} - \eta + \frac{{}_{CCR}\rho l_{CCR}}{\epsilon}}{l_{CCR}}x + \eta \tag{4.5}$$

From the expression in eq (4.5), one can determine the derivative of ϕ at the CCR/bulk oxide boundary

$$\left.\frac{\partial\phi}{\partial x}\right|_{CCR} = \frac{\phi_{CCR} - \eta}{l_{CCR}} - \frac{{}_{CCR}\rho l_{CCR}}{2} \tag{4.6}$$

and the derivative of ϕ at the electrolyte/CCR interface

$$\left.\frac{\partial \phi}{\partial x}\right|_{o/e} = \frac{\phi_{CCR} - \eta + \frac{_{CCR}\rho l_{CCR}^2}{2\epsilon}}{l_{CCR}} \tag{4.7}$$

This expression can be rewritten using eq (4.2) to yield η in terms of ϕ_{CCR}

$$\eta = \frac{\epsilon\phi_{CCR} + \frac{_{CCR}\rho l_{CCR}^2}{2}}{l_{CCR}C_H + \epsilon} \tag{4.8}$$

Finally, substituting eq (4.8) into eq (4.7) yields the effective boundary condition given in eq (4.3).

The ionic transport submodel describes the motion of Al^{3+} and O^{2-} ions through the oxide. In this submodel, two changes are made from the 1D model. First, the derivatives are changed to vector derivatives. The second change is the explicit solution of the continuity equation for the ions in the oxide bulk. In the 1D model, the ionic flux was constant throughout the oxide bulk, and thus the enforcement of continuity was trivial.

The gradient of ϕ, as given by eq (4.1), drives the transport of Al^{3+} and O^{2-} through the oxide film. Assuming the ionic transport is governed by the counter-site defect mechanism described in Chapter III, the ionic fluxes of Al^{3+} and O^{2-}, $\mathbf{J}_{Al^{3+}}$ and $\mathbf{J}_{O^{2-}}$ respectively, are given by the following high-field transport expression

$$\mathbf{J}_{Al^{3+}} = -\mathbf{J}_{O^{2-}} = J_{CSD}^0 \frac{\nabla\phi}{|\nabla\phi|} \sinh\left(\frac{q_{CSD}a_{CSD}|\nabla\phi|}{kT}\right) \tag{4.9}$$

where J_{CSD}^0 is the flux coefficient, $q_{CSD} = q_{Al^{3+}} - q_{O^{2-}}$ is the effective charge of the

counter-site defect, and a_{CSD} is half of the defect jump distance. In eq (4.9), we assume that the concentration of counter-site defects is constant in the oxide, thus making J^0_{CSD} constant.

The evolution of the concentration within the oxide is given by continuity relations in the bulk and in the CCR. The initial values of c_i and ${}_{CCR}c_i$ are set to the average experimental ionic concentration, ${}^{eq}_{ox}c_i$. These average ionic concentrations are determined by the experimental molecular volume of the oxide, Ω_{ox}, such that ${}^{eq}_{ox}c_{O^{2-}} = \frac{3\Omega_{ox}}{N_A}$ and ${}^{eq}_{ox}c_{Al^{3+}} = \frac{2\Omega_{ox}}{N_A}$, where N_A is the Avogadro constant. Within the oxide bulk, the evolution of the concentration is given by:

$$\frac{\partial c_i}{\partial t} = -\nabla \cdot \mathbf{J}_i \tag{4.10}$$

The equation describing the evolution of the concentration within the CCR is:

$$\frac{\partial_{CCR} c_i}{\partial t} = \frac{J_{i\ transfer} - J_i|_{CCR}}{l_{CCR}} \tag{4.11}$$

In these equations, $J_i|_{CCR} = \mathbf{J}_i \cdot \mathbf{n}_{o/e}$ is the normal bulk flux in the oxide infinitesimally close to the boundary of the CCR, with the normal vector of the o/e interface, pointing from the oxide to the electrolyte, given by $\mathbf{n}_{o/e}$. Here, we apply the approximation that $\mathbf{n}_{o/e}$ is equivalent to the normal vector to the CCR/bulk oxide boundary, pointing from the bulk oxide to the CCR, due to the infinitesimally thin nature of the CCR. $J_{i\ transfer}$ is the flux of i transferred from the adsorbed layer to the CCR due to reactions that do not cause the o/e interface to move. The reactions contributing to $J_{i\ transfer}$ are described later in this section.

As c_i and ${}_{CCR}c_i$ evolve according to eqs (4.10) and (4.11), they shift away from their initial value, ${}^{eq}_{ox}c_i$. Excess concentrations, c_i or ${}_{CCR}c_i$ greater than the equilibrium value, ${}^{eq}_{ox}c_i$, indicates the presence of pseudo-interstitials, while c_i or ${}_{CCR}c_i$ greater than ${}^{eq}_{ox}c_i$ indicates the presence of pseudo-vacancies. The concentrations of pseudo-interstitials and pseudo-vacancies in the CCR are relevant to the interfacial reaction submodel discussed later in this section. The concentrations of pseudo-interstitials in the CCR and pseudo-vacancies in the CCR are given by ${}^{int}_{CCR}c_i = max({}_{CCR}c_i - {}^{eq}_{ox}c_i, 0)$ and ${}_{CCR}c_{V_i} = max({}^{eq}_{ox}c_i - {}_{CCR}c_i, 0)$, respectively, where $max(a, b)$ yields the larger value of a and b.

The third and final submodel, which describes the reactions at the o/e and m/o interfaces, is unchanged from the 1D model and is summarized below. In this model, nine reactions occur at the o/e interface and a tenth occurs at the m/o interface. At the o/e interface, these reactions are: (i) the formation of oxide from adsorbed Al^{3+} and adsorbed O^{2-}, (ii) the dissociation of water into H^+, adsorbed O^{2-}, and adsorbed OH^-, (iii) the dissociation of adsorbed OH^- into H^+ and adsorbed O^{2-}, (iv, v) the transfer of O^{2-} from the adsorbed layer into the oxide through either a pseudo-interstitial or pseudo-vacancy mechanism, (vi, vii) the transfer of Al^{3+} from the adsorbed layer into the oxide through either a pseudo-interstitial or pseudo-vacancy mechanism, (viii) the formation of adsorbed $AlOH^{2+}$ from adsorbed Al^{3+} and adsorbed OH^-, and (ix) the ejection of adsorbed $AlOH^{2+}$ into the electrolyte. The only reaction at the m/o interface is (x) the combination of O^{2-} from the oxide reacting with the Al substrate to form new oxide. Reactions (i) and (x) are responsible for the motion of the o/e and m/o interfaces, respectively. Reactions (iv)-(vii) are

the transfer reactions responsible for $J_{i\ transfer}$ in eq (4.11).

In Chapter III, five assumptions were made in formulating the model equations from these reactions. First, the model assumed that the electrolyte pH was below 10 to avoid consideration of additional reaction mechanisms in strongly alkaline electrolytes.[74] Second, it assumed that the concentrations of adsorbed O^{2-} and adsorbed OH^- were at equilibrium. Third, it is assumed that the concentration of adsorbed $AlOH^{2+}$ was at equilibrium, and that the equilibrium concentration was low enough to neglect it when calculating the number of vacant cation sites in the adsorbed layer. Fourth, it assumed that the ejection of adsorbed $AlOH^{2+}$ into the electrolyte was irreversible because $AlOH^{2+}$ ions in the electrolyte diffuse away from the interface. Finally, it assumed that the oxidation reaction at the m/o interface is irreversible and transport-limited.

The governing equations for the interfacial reactions submodel at the o/e interface are:

$$\frac{\partial_{ad}c_{Al^{3+}}}{\partial t} = -\left(2R_{oxidation} + J_{Al^{3+}transfer} + k_{eject}\frac{{}_{ad}c_{Al^{3+}}\,{}_{ad}c_{OH^-}}{{}_{ad}c_{V_{anion}}}\exp\left(\frac{\gamma e\eta}{kT}\right)\right) \quad (4.12)$$

$$R_{oxidation} = k_{ox}^{+}({}_{ad}c_{Al^{3+}})^2({}_{ad}c_{O^{2-}})^3 - k_{ox}^{-}({}_{CCR}c_{Al^{3+}})^2({}_{CCR}c_{O^{2-}})^3({}_{ad}c_{V_{cation}})^2({}_{ad}c_{V_{anion}})^3 \quad (4.13)$$

$$J_{O^{2-}transfer} = k_{O_{vac}}^{+}\,{}_{ad}c_{O^{2-}}\,{}_{CCR}c_{V_O^{2-}} + k_{O_{int}}^{+}\,{}_{ad}c_{O^{2-}} - k_{O_{vac}}^{-}\,{}_{CCR}c_{O^{2-}}\,{}_{ad}c_{V_{anion}} - k_{O_{int}}^{-}\,{}_{CCR}^{int}c_{O^{2-}}\,{}_{ad}c_{V_{anion}} \quad (4.14)$$

$$J_{Al^{3+}transfer} = k^{+}_{Al_{vac}}{}_{ad}c_{Al^{3+}}{}_{CCR}c_{V_Al^{3+}} + k^{+}_{Al_{int}}{}_{ad}c_{Al^{3+}} - k^{-}_{Al_{vac}}{}_{CCR}c_{Al^{3+}}{}_{ad}c_{V_{cation}} - k^{-}_{Al_{int}}{}^{int}_{CCR}c_{Al^{3+}}{}_{ad}c_{V_{cation}} \quad (4.15)$$

$$_{ad}c_{OH^-} = \frac{K_{OH}{}_{ad}c_{V_{anion}}}{{}_{e}c_{H^+}} \exp\left(\frac{e\eta}{kT}\right) \quad (4.16)$$

$$_{ad}c_{O^{2-}} = \frac{K_{O}{}_{ad}c_{OH^-}}{{}_{e}c_{H^+}} \exp\left(\frac{e\eta}{kT}\right) \quad (4.17)$$

In these equations, the concentrations of vacancies in the adsorbed layer are given by $_{ad}c_{V_{anion}} = {}^{max}_{ad}c_{anion} - {}_{ad}c_{O^{2-}} - {}_{ad}c_{OH^-}$ and $_{ad}c_{V_{cation}} = {}^{max}_{ad}c_{cation} - {}_{ad}c_{Al^{3+}}$, where ${}^{max}_{ad}c_{anion}$ and ${}^{max}_{ad}c_{cation}$ are the (areal) number densities of anion and cation sites, respectively, in the adsorbed layer. In eq (4.14), $k^{+}_{O_{int}}$, $k^{-}_{O_{int}}$, $k^{+}_{O_{vac}}$, and $k^{-}_{O_{vac}}$ are the forward and backward reaction constants for the pseudo-interstitial and pseudo-vacancy O^{2-} transfer reactions. Likewise, in eq (4.15), $k^{+}_{Al_{int}}$, $k^{-}_{Al_{int}}$, $k^{+}_{Al_{vac}}$, and $k^{-}_{Al_{vac}}$ are the forward and backward reaction constants for the pseudo-interstitial and pseudo-vacancy Al^{3+} transfer reactions. In eq (4.12), k_{eject} is the reaction constant and γ is the effective charge transfer coefficient for the ejection of adsorbed $AlOH^{2+}$ into the electrolyte. In eqs (4.16) and (4.17), K_{OH} and K_O are the equilibrium constants for the dissociation of water and the dissociation of adsorbed OH^-, respectively.

The velocities of the o/e interface and m/o interface, respectively, are

$$_{o/e}v = -\frac{\Omega_{oxide}R_{oxidation}}{N_A} \quad (4.18)$$

$$_{m/o}v = \frac{2\Omega_{oxide}J_{O^{2-}}|_{m/o}}{3N_A} \quad (4.19)$$

where $J_{O^{2-}}|_{CCR} = \mathbf{J}_{O^{2-}} \cdot \mathbf{n}_{m/o}$ is the normal bulk flux in the oxide bulk infinitesimally close to the m/o interface, and with the outward normal vector of the o/e interface given by $\mathbf{n}_{o/e}$. For both ${}_{o/e}v$ and ${}_{m/o}v$, positive values correspond to motion toward the metal substrate.

4.3 Computational Methods

4.3.1 Smoothed Boundary Method Formulation for the Electric Potential Submodel

The smoothed boundary method (SBM) is utilized to solve eq (4.1) to obtain ϕ. The SBM is a diffuse interface method for applying boundary conditions along interfaces on the interior of the computational domain.[21] In this method, the location of the interface is given by a domain parameter, ψ. This domain parameter is unity in the domain of interest and zero outside, with a smooth transition from zero to unity across the interface.

The model system has three phases, the electrolyte, the oxide, and the metal substrate, and thus requires three respective domain parameters, ψ_e, ψ_{ox}, and ψ_m. A Dirichlet boundary condition, $B_{D,o/e} = \phi_{app}$, is applied at the m/o interface. The SBM permits allows one to apply either Dirichlet or Neumann boundary conditions.[21] Therefore, the Robin boundary condition for ϕ along the o/e interface, given by eq (4.3), can either be treated as a Neumann boundary condition as a function of ϕ or as a Dirichlet boundary condition as a function of the normal derivative of ϕ. Tests indicated that the Neumann boundary condition treatment was more accurate

unless the Neumann contribution to the Robin boundary condition is negligible, and therefore we use the Neumann formulation. The smoothed boundary method formulation of eq (4.1) is given by:[21]

$$\frac{1}{\psi_{ox}}\nabla\cdot(\psi_{ox}\nabla\phi)-\frac{1}{\psi_m^2}\left[\nabla\psi_m\cdot\nabla(\psi_m\phi)-B_{D,o/e}|\nabla\psi_m|^2\right]+\frac{|\nabla\psi_e|}{\psi_e}B_{N,m/o}(\phi)=0 \quad (4.20)$$

where the Neumann boundary condition, $B_{N,m/o}(\phi)=\partial\phi/\partial n|_{CCR}$, is given by eq (4.3). The solution of the model equations using the SBM was compared with the solution using the 1D sharp interface method presented in Chapter III, and it was confirmed that the solutions are identical within a small numerical difference, given a well-resolved SBM boundary that was sufficiently thin.

4.3.2 Application of the Level Set Method

The level set method is used to define and evolve the domain parameters in eq (4.20). In the level set method, the interface is defined as the contour where a function, ξ, is zero (known as the zero level set).[23] We take ξ to be a signed distance function. A different length scale is used in the level set calculations from elsewhere, in which the grid spacing, h_{LS}, is unity, and where the distances given by ξ are measured in grid spacings. The domain parameters in eq (4.20) are determined from the distance functions defining the o/e and m/o interfaces, $\xi_{o/e}$ and $\xi_{m/o}$ respectively.

ψ_e, ψ_m, and ψ_{ox} are given by

$$\psi_e = \frac{1 - \tanh\left(\frac{\xi_{o/e}}{W}\right)}{2} \tag{4.21}$$

$$\psi_m = \frac{1 - \tanh\left(\frac{\xi_{m/o}}{W}\right)}{2} \tag{4.22}$$

$$\psi_{ox} = 1 - \psi_e - \psi_m \tag{4.23}$$

where W controls the interfacial width.

Each distance function ξ_j (for j = o/e, m/o) is defined by the steady-state solution of[23]

$$\frac{\partial \xi_j}{\partial t'} = -S_j(1 - |\nabla \xi_j|) \tag{4.24}$$

where t' is a dummy time variable for the generation of ξ_j. The smoothed sign function, S_j, is defined as $S_j = \xi_j/(\xi_j^2 + \delta^2)$, where δ is a parameter determining the width of the transition from -1 to 1.[197] Equation (4.24) is initialized by a function, ξ_j^0, whose zero level set defines the initial interface, as described in the next subsection.

The level set method is also used to evolve the interfaces. The interfacial motion is accomplished by the following equation

$$\frac{\partial \xi_j}{\partial t} = {}_j v |\nabla \xi_j| \tag{4.25}$$

Here, the velocity has the property $\nabla_j v \cdot \nabla \xi_j = 0$ (i.e., ${}_j v$ is constant along lines normal to the interface), which limits distortions in ξ_j as the interface moves, and decreases the required frequency of redistancing.[23] The extension scheme to extend

${}_jv$ from the interfacial region to the entire domain is detailed in Section 4.3.5.

4.3.3 Computational Domain and Initial Geometry

In this chapter, we focus on simulations of individual pores in a pseudo-3D axisymmetric computational domain, which approximates the hexagonal symmetry of an array of nanopores. In the radial direction, the computational domain extends from $r = 0$ along the center of the cylinder to $r = R_{cell}$ at the radial boundary. In the axial direction, the computational domain extends from $z = 0$ in the electrolyte to $z = L_z$ in the metal substrate, taking z to increase along the growth direction. The computational domain is discretized into a grid with uniform spacing, h, in the radial and axial directions. The initial geometry of the system, defined by ξ_j^0, is of a partially developed pore with a geometry estimated to be close to the steady-state geometry from an initial set of simulations.

The initial pore geometry is constructed from a combination of straight lines (the top and side of the pore wall) and arcs (the o/e interface at the base of the pore and the m/o interface). The initial geometry for each simulation depends on ϕ_{app} and the cell size chosen for that particular simulation. As described below in Section 4.3.7, the pore cell size, $L_{cell} = 2R_{cell}$, varies between simulations. The initial radius of the pore is chosen to be 0.435 L_{cell}. The arc defining the m/o interface and the arc defining the o/e interface at the base of the pore have equal radii of curvature, R_{curve}. R_{curve} is selected such that the change in the height of the o/e interface from the pore center to where the arc meets the pore wall is given by 0.1 ϕ_{app} nm/V. Therefore, R_{curve} is equal to $\frac{(0.1\ \phi_{app}\ \text{nm/V})^2+(0.435\ L_{cell})^2}{0.2\ \phi_{app}\ \text{nm/V}}$. The length of the vertical portion of

the pore wall and the pore barrier thickness are given by 0.3 ϕ_{app} nm/V and 1.2 ϕ_{app} nm/V, respectively.

From the geometry described in the previous paragraph, ξ_j^0 was constructed to have a hyperbolic tangent profile given by $\xi_j^0 = \tanh(\frac{g_j}{4.5})$, where g_j is a piecewise function that approximates a distance function in the neighborhood of the interface. The hyperbolic tangent function is used to remove artifacts due to the piecewise nature of g_j. A smoothing operation, where the value of ξ_j^0 at each grid point is averaged with the value of ξ_j at its four neighboring grid points, is applied twice to ξ_j^0 to remove any discontinuities in ξ_j^0 as a result of piecewise construction. The initial pore geometry for $\phi_{app} = 40$ V and $L_{cell} = 64$ nm, after the initial solution of eq (4.24) to calculate ξ_j, is shown in Fig. 4.2a.

4.3.4 Finite Difference Implementation of the Model Equations

The model equations are solved using the finite difference method in cylindrical coordinates. Equation (4.20) is discretized using central finite differences and is solved using alternating-direction line-relaxation (ADLR) method.[198] The solution is considered to have converged when the maximum difference in ϕ between iterations is less than the convergence criterion, $\delta\phi_{ADLR}$. The spatial derivatives in eq (4.10) are discretized using a central finite differencing scheme and first-order upwind derivatives are used to calculate $\nabla\xi_j$.[23] Time evolution is performed using the forward Euler method for all time-dependent equations, eqs (4.10) to (4.12), (4.24) and (4.25).

The discretization stencils for eqs (4.10) to (4.12), (4.20), (4.24) and (4.25) are given below. In the following stencils, the subscripts α and β are indices in associated

with the r and z coordinates, respectively, the superscript n denotes that the value of the variable is taken at the current time step, and the superscript m denotes that the value of the variable is taken at the current dummy time step used to generate ξ_j.

The discretization stencil for eq (4.10) using central finite differencing in cylindrical coordinates for spatial derivatives and the forward Euler method for time evolution is:

$$\frac{c_{i,\alpha,\beta}^{n+1} - c_{i,\alpha,\beta}^{n}}{\Delta t} = -\frac{1}{r_{\alpha,\beta}} \left[\frac{\frac{r_{\alpha+1,\beta}+r_{\alpha,\beta}}{2} J_{i,\alpha+1/2,\beta} - \frac{r_{\alpha,\beta}+r_{\alpha-1,\beta}}{2} J_{i,\alpha-1/2,\beta}}{h} + \frac{J_{i,\alpha,\beta+1/2} - J_{i,\alpha,\beta-1/2}}{h} \right] \tag{4.26}$$

where the discretized fluxes at half grid points are given by:

$$J_{i,\alpha+1/2,\beta} = J_{CSD}^{0} \frac{\phi_{\alpha+1,\beta}^{n} - \phi_{\alpha,\beta}^{n}}{\sqrt{\left(\phi_{\alpha+1,\beta}^{n} - \phi_{\alpha,\beta}^{n}\right)^2 + \frac{1}{16}\left(\phi_{\alpha,\beta+1}^{n} - \phi_{\alpha,\beta-1}^{n} + \phi_{\alpha+1,\beta+1}^{n} - \phi_{\alpha+1,\beta+1}^{n}\right)^2}}$$
$$\sinh\left(\frac{q_{CSD} a_{CSD}}{kT} \sqrt{\left(\phi_{\alpha+1,\beta}^{n} - \phi_{\alpha,\beta}^{n}\right)^2 + \frac{1}{16}\left(\phi_{\alpha,\beta+1}^{n} - \phi_{\alpha,\beta-1}^{n} + \phi_{\alpha+1,\beta+1}^{n} - \phi_{\alpha+1,\beta+1}^{n}\right)^2} \right) \tag{4.27}$$

$$J_{i,\alpha-1/2,\beta} = J_{CSD}^{0} \frac{\phi_{\alpha,\beta}^{n} - \phi_{\alpha-1,\beta}^{n}}{\sqrt{\left(\phi_{\alpha,\beta}^{n} - \phi_{\alpha-1,\beta}^{n}\right)^2 + \frac{1}{16}\left(\phi_{\alpha,\beta+1}^{n} - \phi_{\alpha,\beta-1}^{n} + \phi_{\alpha-1,\beta+1}^{n} - \phi_{\alpha-1,\beta+1}^{n}\right)^2}}$$
$$\sinh\left(\frac{q_{CSD} a_{CSD}}{kT} \sqrt{\left(\phi_{\alpha,\beta}^{n} - \phi_{\alpha-1,\beta}^{n}\right)^2 + \frac{1}{16}\left(\phi_{\alpha,\beta+1}^{n} - \phi_{\alpha,\beta-1}^{n} + \phi_{\alpha-1,\beta+1}^{n} - \phi_{\alpha-1,\beta+1}^{n}\right)^2} \right) \tag{4.28}$$

$$J_{i,\alpha,\beta+1/2} = J^0_{CSD} \frac{\phi^n_{\alpha,\beta+1} - \phi^n_{\alpha,\beta}}{\sqrt{\left(\phi^n_{\alpha,\beta+1} - \phi^n_{\alpha,\beta}\right)^2 + \frac{1}{16}\left(\phi^n_{\alpha+1,\beta} - \phi^n_{\alpha-1,\beta} + \phi^n_{\alpha+1,\beta+1} - \phi^n_{\alpha-1,\beta+1}\right)^2}}$$
$$\sinh\left(\frac{q_{CSD}a_{CSD}}{kT}\sqrt{\left(\phi^n_{\alpha,\beta+1} - \phi^n_{\alpha,\beta}\right)^2 + \frac{1}{16}\left(\phi^n_{\alpha+1,\beta} - \phi^n_{\alpha-1,\beta} + \phi^n_{\alpha+1,\beta+1} - \phi^n_{\alpha-1,\beta+1}\right)^2}\right) \tag{4.29}$$

$$J_{i,\alpha,\beta-1/2} = J^0_{CSD} \frac{\phi^n_{\alpha,\beta} - \phi^n_{\alpha,\beta-1}}{\sqrt{\left(\phi^n_{\alpha,\beta} - \phi^n_{\alpha,\beta-1}\right)^2 + \frac{1}{16}\left(\phi^n_{\alpha+1,\beta} - \phi^n_{\alpha-1,\beta} + \phi^n_{\alpha+1,\beta-1} - \phi^n_{\alpha-1,\beta-1}\right)^2}}$$
$$\sinh\left(\frac{q_{CSD}a_{CSD}}{kT}\sqrt{\left(\phi^n_{\alpha,\beta} - \phi^n_{\alpha,\beta-1}\right)^2 + \frac{1}{16}\left(\phi^n_{\alpha+1,\beta} - \phi^n_{\alpha-1,\beta} + \phi^n_{\alpha+1,\beta-1} - \phi^n_{\alpha-1,\beta-1}\right)^2}\right) \tag{4.30}$$

The stencils for 4.11 and 4.12 are determined using the forward Euler method and are respectively given by:

$$\frac{{}_{CCR}C^{n+1}_{i,\alpha,\beta} - {}_{CCR}C^n_{i,\alpha,\beta}}{\Delta t} = \frac{J^n_{i\ transfer,\alpha,\beta} - J^n_i|_{CCR,\alpha,\beta}}{l_{CCR}} \tag{4.31}$$

$$\frac{{}_{ad}C^{n+1}_{Al^{3+},\alpha,\beta} - {}_{CCR}C^n_{i,\alpha,\beta}}{\Delta t} =$$
$$-\left(2R^n_{oxidation,\alpha,\beta} + J^n_{Al^{3+}transfer,\alpha,\beta} + k_{eject}\frac{{}_{ad}C^n_{Al^{3+},\alpha,\beta}\,{}_{ad}C^n_{OH^-,\alpha,\beta}}{{}_{ad}C^n_{V_{anion},\alpha,\beta}}\exp\left(\frac{\gamma e\eta^n_{\alpha,\beta}}{kT}\right)\right) \tag{4.32}$$

The discretization stencil for eq (4.20) using central finite differencing and cylindrical

coordinates is:

$$\frac{1}{r_{\alpha,\beta}\psi_{ox,\alpha,\beta}h^2}\Bigg[\frac{(r_{\alpha+1,\beta}+r_{\alpha,\beta})(\psi_{ox,\alpha+1,\beta}+\psi_{ox,\alpha,\beta})}{4}(\phi_{\alpha+1,\beta}-\phi_{\alpha,\beta}) - \frac{(r_{\alpha,\beta}+r_{\alpha-1,\beta})(\psi_{ox,\alpha,\beta}+\psi_{ox,\alpha-1,\beta})}{4}(\phi_{\alpha,\beta}-\phi_{\alpha-1,\beta}) + \frac{\psi_{ox,\alpha,\beta+1}+\psi_{ox,\alpha,\beta}}{4}(\phi_{\alpha,\beta+1}-\phi_{\alpha,\beta}) - \frac{\psi_{ox,\alpha,\beta}+\psi_{ox,\alpha,\beta-1}}{4}(\phi_{\alpha,\beta}-\phi_{\alpha,\beta-1})\Bigg] - \frac{1}{4\psi_{m,\alpha,\beta}h^2}\Bigg[(\psi_{m,\alpha+1,\beta}-\psi_{m,\alpha-1,\beta})(\psi_{m,\alpha+1,\beta}\phi_{\alpha+1,\beta}-\psi_{m,\alpha-1,\beta}\phi_{\alpha-1,\beta}) + (\psi_{m,\alpha,\beta+1}-\psi_{m,\alpha,\beta-1})(\psi_{m,\alpha,\beta+1}\phi_{\alpha,\beta+1}-\psi_{m,\alpha,\beta-1}\phi_{\alpha,\beta-1}) - \phi_{app}((\psi_{m,\alpha+1,\beta}-\psi_{m,\alpha-1,\beta})^2+(\psi_{m,\alpha,\beta+1}-\psi_{m,\alpha,\beta-1})^2)\Bigg] + \frac{\sqrt{(\psi_{e,\alpha+1,\beta}-\psi_{e,\alpha-1,\beta})^2+(\psi_{e,\alpha,\beta+1}-\psi_{e,\alpha,\beta-1})^2}}{\psi_{e,\alpha,\beta}}B_{N,m/o,\alpha,\beta}=0 \quad (4.33)$$

where the Neumann boundary condition, $B_{N,m/o,\alpha,\beta}$ is given by

$$B_{N,m/o,\alpha,\beta}=\frac{C_{Helmholtz}}{l_{CCR}C_{Helmholtz}+\epsilon}\phi_{\alpha,\beta}-\frac{{}_{CCR}\rho_{\alpha,\beta}l_{CCR}}{2l_{CCR}C_{Helmholtz}+2\epsilon}-\frac{{}_{CCR}\rho_{\alpha,\beta}l_{CCR}}{2\epsilon} \quad (4.34)$$

The stencils for eqs (4.24) and (4.25) are determined using first order upwind spatial derivatives and the forward Euler method for time evolution. These stencils are respectively given by:

$$\frac{\xi^{m+1}_{j,\alpha,\beta}-\xi^{m}_{j,\alpha,\beta}}{\Delta t'}=-S^{m}_{j,\alpha,\beta}(1-G^{m}_{j,\alpha,\beta}) \quad (4.35)$$

$$\frac{\xi^{n+1}_{j,\alpha,\beta}-\xi^{n}_{j,\alpha,\beta}}{\Delta t}={}_{j}v^{ext,n}_{\alpha,\beta}G^{n}_{j,\alpha,\beta} \quad (4.36)$$

where $G^m_{j,\alpha,\beta}$ is the magnitude of the upwind gradient of ξ_j. The magnitude of the upwind gradient is given by the following expression:[199]

$$G^m_{j,\alpha,\beta} = \begin{cases} max\left(max\left(\frac{\xi^m_{j,\alpha,\beta}-\xi^m_{j,\alpha-1,\beta}}{h_{LS}},0\right)^2,\ min\left(\frac{\xi^m_{j,\alpha+1,\beta}-\xi^m_{j,\alpha,\beta}}{h_{LS}},0\right)^2 \right. & \\ \quad \left. +max\left(\frac{\xi^m_{j,\alpha,\beta}-\xi^m_{j,\alpha,\beta-1}}{h_{LS}},0\right)^2,\ min\left(\frac{\xi^m_{j,\alpha,\beta+1}-\xi^m_{j,\alpha,\beta}}{h_{LS}},0\right)^2 \right) & S^m_{j,\alpha,\beta} > 0 \\ max\left(min\left(\frac{\xi^m_{j,\alpha,\beta}-\xi^m_{j,\alpha-1,\beta}}{h_{LS}},0\right)^2,\ max\left(\frac{\xi^m_{j,\alpha+1,\beta}-\xi^m_{j,\alpha,\beta}}{h_{LS}},0\right)^2 \right. & \\ \quad \left. +min\left(\frac{\xi^m_{j,\alpha,\beta}-\xi^m_{j,\alpha,\beta-1}}{h_{LS}},0\right)^2,\ max\left(\frac{\xi^m_{j,\alpha,\beta+1}-\xi^m_{j,\alpha,\beta}}{h_{LS}},0\right)^2 \right) & S^m_{j,\alpha,\beta} < 0 \\ \frac{\xi^m_{j,\alpha+1,\beta}-\xi^m_{j,\alpha-1,\beta}}{2h_{LS}} & S^m_{j,\alpha,\beta} = 0 \end{cases} \tag{4.37}$$

Equation (4.24) is considered to have converged if the maximum value of $|S_j(1 - |\nabla\xi_j|)|$ is less than the convergence criterion, δ_{dist}. Equation (4.24) must be occasionally re-applied to ensure that ξ_j is a distance function, a process called redistancing. A redistancing operation is conducted every n_{redist} time steps. During the evolution of eq (4.24) the interface can drift slightly.[23] To prevent excessive drift, the solution of eq (4.24) is stopped if the number of iterations is greater than N_{dist}, which has different values for the initial generation of ξ_j and for redistancing, N^{init}_{dist} and N^{redist}_{dist}, respectively. Although truncating the iteration of eq (4.24) before it has fully converged introduces a small amount of error into ξ_i (where the error in $|\nabla\xi_j|$ is less than 1%), the effect on the solutions via the SBM boundary conditions is less than that caused by interfacial drift if iteration was allowed to continue.

Zero-gradient boundary conditions for ϕ and ξ_j are applied along $r = 0$ to represent

the axisymmetric geometry. A zero-gradient boundary condition is also applied for ϕ along $r = R_{cell}$ to approximate the behavior of an infinite hexagonal array of pores, where the flux of ions is zero at the boundary between the cells of adjacent pores. A zero-gradient boundary condition is also applied for ξ_j along $r = R_{cell}$ to simulate the effect of an adjacent pore. The axial boundaries of the computational domain ($z = 0$ and $z = L_z$) are outside the SBM-defined domain where ϕ is solved, and thus have little effect on the ϕ inside the SBM-defined domain.[20] A zero-derivative boundary condition is applied along $z = 0$, and ϕ is set to ϕ_{app} along $z = L_z$. Boundary conditions for ξ_j along $z = 0$ and $z = L_z$ are unnecessary as a result of the upwind scheme employed for the level set equations.

4.3.5 Extension Scheme for Interfacial Variables

There are several variables that are defined to describe interfacial quantities, such as interfacial velocities and concentrations. Due to the diffuse interface nature of the methods we apply, these quantities must be accurately represented throughout the interfacial region. This requires the storage of the interfacial values across the diffuse interfacial region.[200] The value of ϕ_{CCR} throughout the interfacial region is determined by the value of ϕ at the zero level set of $\xi_{o/e}$. The values of ${}_{o/e}v$, ${}_{CCR}c_{O^{2-}}$, ${}_{CCR}c_{Al^{3+}}$, and ${}_{ad}c_{Al^{3+}}$ throughout the interfacial region are all determined by their respective values at the zero level set of $\xi_{o/e}$, while ${}_{m/o}v$ is determined by its value at the zero level set of $\xi_{m/o}$.

While in theory all of the extensions should be from the zero level set of ξ_j, in practice, an artifact due to the diffuse nature of the SBM makes another level set a

better choice for some variables. In the calculation of eq (4.20), the SBM-imposed conditions on ϕ cause the electric field to be artificially low near the interfaces, which also affects the fluxes near the interfaces. To avoid this artifact, the interfacial quantities $J_{O^{2-}}|_{CCR}$, $J_{Al^{3+}}|_{CCR}$, and $J_{O^{2-}}|_{m/o}$ are determined from the values of the bulk fluxes, $\mathbf{J}_i$, eight grid points into the oxide bulk from the interface. In addition, the same artifacts cause eq (4.10) to yield incorrect bulk ion concentrations near the interfaces. Therefore, we determine the values of ρ in the interfacial regions from their accurate bulk values taken from eight points into the oxide.

The extension algorithm propagates the interpolated value of a variable at a particular level set, Γ, of ξ_j in the direction given by the normal of the interface. This scheme is conceptually similar to the scheme by Malladi et al. that constructs extension velocities.[201] For a discrete function, f, defined at the grid points inside the computational domain, the extension of f from the level set given by $\xi_j = \Gamma$ is defined as f^{ext}. If the continuous function, $\tilde{f}(r, z)$, is defined from the bilinear interpolation of f, then the value of f^{ext} at a point on the discrete grid, (r_α, z_β), is given by:

$$f^{ext}(r_\alpha, z_\beta) = \tilde{f}\left(r_\alpha + h(\Gamma - \xi_j)\frac{\partial\xi_j/\partial r}{|\nabla\xi_j|}, z_\beta + h(\Gamma - \xi_j)\frac{\partial\xi_j/\partial z}{|\nabla\xi_j|}\right) \tag{4.38}$$

where α and β are indices associated with the r and z coordinates, respectively. The extension in performed in a band near the interface where $|\xi_j| < w_{band}$, except for the extension for ${}_jv$, which is extended throughout the entire computational domain.

Other variables are derived from variables defined using an extension scheme and thus are only defined within the interfacial band: ${}_{CCR}\rho$, η, $R_{oxidation}$, $J_{O^{2-}transfer}$, $J_{Al^{3+}transfer}$, ${}_{ad}c_{O^{2-}}$, ${}_{ad}c_{OH^-}$, ${}_{CCR}c_{V_O^{2-}}$, ${}_{ad}c_{V_{anion}}$, ${}^{int}_{CCR}c_{O^{2-}}$, ${}_{CCR}c_{V_Al^{3+}}$, ${}_{ad}c_{V_{cation}}$, and

${}^{int}_{CCR}c_{Al^{3+}}$.

4.3.6 Strategies to Improve the Computational Speed and Stability of the Simulations

Four strategies are employed to improve the speed and stability of the numerical calculations. First, the calculations are parallelized using OpenMP to leverage the availability high-performance computing resources. The second strategy is a separate time step for eq (4.12), the equation describing the evolution of ${}_{ad}c_{Al^{3+}}$. In this equation, ${}_{ad}c_{Al^{3+}}$ is very close to ${}^{max}_{ad}c_{cation}$, making ${}_{ad}c_{V_{cation}}$ almost zero. Thus, small changes in ${}^{max}_{ad}c_{cation}$ can cause order of magnitude changes in ${}_{ad}c_{V_{cation}}$, which influences eq (4.12) through the expressions in eqs (4.13) and (4.15). To prevent large changes in ${}_{ad}c_{V_{cation}}$ between time steps, we use a smaller time step for eq (4.12), taking 140 time steps for eq (4.12) for each time step taken for the other equations. The other variables change minimally between time steps. The third strategy is a tiered time step, in which the time step size is optimized for accuracy and efficiency. Small time step sizes are employed at the beginning of the simulation to resolve initial transients (Δt_1) and to allow the ionic concentrations to approach their steady-state values (Δt_2) and then a larger value (Δt_3) is employed for the remainder of the simulation. The following scheme is used for the time step Δt at iteration i_{iter}:

$$\Delta t(i_{iter}) = \Delta t_1 + \frac{(\Delta t_2 - \Delta t_1)\tanh\left(\frac{i_{iter}-i_{transition,1-2}}{w_{transition}}+1\right)}{2} + \frac{(\Delta t_3 - \Delta t_2)\tanh\left(\frac{i_{iter}-i_{transition,2-3}}{w_{transition}}+1\right)}{2} \quad (4.39)$$

In this form, Δt has smooth transitions centered at iteration numbers $i_{transition,1-2}$ and $i_{transition,2-3}$, with a transition duration controlled by $w_{transition}$. The fourth strategy is to begin the simulations with a smaller computational domain and then add grid points at the bottom of the domain as the pore grows, such that the bottom-most part of the m/o interface is between 15 and 30 grid points from the bottom of the computational domain. This expanding computational domain reduces unnecessary calculations in the substrate phase far from the m/o interface.

4.3.7 Determination of the Preferred Steady-State Pore Cell Size

Using the methods described above, simulations of pore growth were performed with various values of ϕ_{app} and the electrolyte pH. The preferred cell size for each combination of ϕ_{app} and pH was determined by finding the cell size with the fastest-growing stable pore (using the assumption known as the maximum velocity principle[103,202]). The pore was considered to have reached steady state when the difference between the pore diameters measured at one quarter and twice the pore barrier thickness above the o/e interface at the pore center was ¡1%. The cell sizes were varied in increments of $\phi_{app} = 10$ nm/V, and the preferred cell size was identified as that with the maximum growth rate among those that do not exhibit pore splitting.

4.4 Simulation Parameters

Most of the physical parameters in this work are identical to those in Ref. Chapter III, and can be found in Table 4.1. As in Ref. Chapter III, the values of these parameters were determined by fitting the 1D sharp interface model to experimental

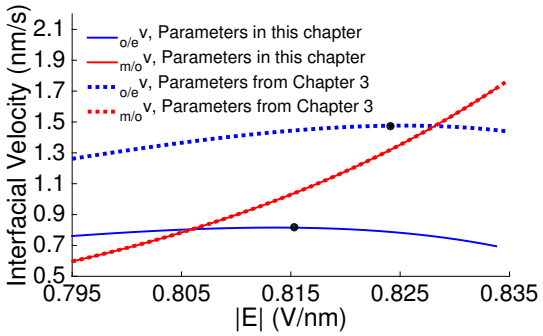

Figure 4.1: The interfacial velocities as a function of $|E|$, based on 1D sharp interface calculations, for the parameters from Chapter III and the parameters used in this chapter. The maximum o/e velocity for each parameter set is marked with a black dot.

data for $AlOH^{2+}$ ejection,[74] the charge embedded in the o/e interface,[100] and the pore barrier thickness for anodization at 30 V in a 1.1 pH oxalic acid electrolyte.[55] It was noted in Ref. Chapter III that a parameterization based on these experimental observations is not unique, and that different values of k_{ox}^{-}, k_{eject}, and $k_{Al_{vac}^{-}}$ can be consistent with the aforementioned experimental observations.

The values of k_{ox}^{-}, k_{eject}, and $k_{Al_{vac}^{-}}$ determine the preferred pore geometry by controlling the difference between the magnitude of the electric field, $|E|$, at the o/e interface and $|E|$ at the m/o interface when the pore is growing into the substrate at its maximum steady-state rate, which we refer to as $\Delta|E|$. For the pore geometry typically seen in anodic alumina films, the curvature of the interfaces focuses the electric field at the o/e interface and defocuses it at the m/o interface such that $\Delta|E|$ is positive (i.e., $|E|$ is higher at the o/e interface than at the m/o interface).[97,103,113] However, 1D sharp interface simulations shown in Fig. 4.1 indicate that the values of k_{ox}^{-}, k_{eject}, and $k_{Al_{vac}^{-}}$ from Chapter III result in a negative value of $\Delta|E|$. This

Table 4.1: Physical Parameters

Oxide Constants:		
$C_{Helmholtz}$	Helmholtz layer capacitance	50×10^{-20} F/nm
ϵ	Oxide permittivity	$9.8\ \epsilon_0$
Ω_{oxide}	Oxide molar volume	3.3×10^{22} nm^3/mol
${}^{max}_{ad}c_{anion}$	Number density of adsorbed anion sites	9.15 nm^{-2}
${}^{max}_{ad}c_{cation}$	Number density of adsorbed cation sites	6.10 nm^{-2}
a_{CSD}	Half the counter-site defect jump distance	0.14 nm
q_{CSD}	Charge of the counter-site defect	$5e$
J^0_{CSD}	Counter-site defect flux coefficient	2.54×10^{-8} nm^{-2}
l_{CCR}	Thickness of the CCR	0.28 nm
T	Temperature	298 K
Reaction Constants:		
γ	$AlOH^{2+}$ ejection charge transfer coefficient	0.35
${}_{ad}K_O$	Equilibrium constant for adsorbed O^{2-} formation	2.2×10^{-13} nm^{-2}
${}_{ad}K_{OH}$	Equilibrium constant for adsorbed OH^- formation	1.0×10^{-6} nm^{-2}
k^+_{ox}	Oxidation rate constant	5.0×10^{6} nm^8 s^{-1}
k^-_{ox}	Dissolution rate constant	1.45×10^{7} nm^{18} s^{-1}
k_{eject}	$AlOH^{2+}$ ejection rate constant	1.1×10^{-5} s^{-1}
$k^+_{O_{vac}}$	Forward oxygen vacancy transfer rate constant	1.0×10^{5} nm^3 s^{-1}
$k^-_{O_{vac}}$	Backward oxygen vacancy transfer rate constant	0
$k^+_{O_{int}}$	Forward oxygen interstitial transfer rate constant	0
$k^-_{O_{int}}$	Backward oxygen interstitial transfer rate constant	4.5×10^{4} nm^3 s^{-1}
$k^+_{Al_{vac}}$	Forward aluminum vacancy transfer rate constant	6.45 nm^3 s^{-1}
$k^-_{Al_{vac}}$	Backward aluminum vacancy transfer rate constant	2.53×10^{3} nm^3 s^{-1}
$k^+_{Al_{int}}$	Forward aluminum interstitial transfer rate constant	0
$k^-_{Al_{int}}$	Backward aluminum interstitial transfer rate constant	1.0×10^{5} nm^3 s^{-1}

inconsistency was not apparent in the 1D simulations, and while these parameters are provided key features of barrier film growth, these parameters cannot yield a preferred pore geometry and should not be used for simulations of pore growth.

A series of simulations were conducted to determine a new set of values for k^-_{ox}, k_{eject}, and $k_{Al^-_{vac}}$ that would lead to a preferred pore geometry consistent with experimental observations. The values of these variables were chosen such that the simulated preferred pore cell size for a simulation at $\phi_{app} = 30$ V and 1.0 pH matched the preferred pore cell size from the experiments of Friedman et al., 64 nm.[52] These values of k^-_{ox}, k_{eject}, and $k_{Al^-_{vac}}$ can be found in Table 4.1 and were used for the remaining simulations presented in this chapter.

The numerical parameters were chosen to ensure a combination of accuracy and

Table 4.2: Numerical Parameters

h	Grid spacing	$2\phi_{app}$/300 nm/V
α_1	Tier 1 Courant number	4.0×10^{-8}
α_2	Tier 2 Courant number	2.0×10^{-6}
α_3	Tier 3 Courant number	2.2×10^{-5}
$i_{transition,1-2}$	Number of iterations until transition from Δt_1 to Δt_2	5,000
$i_{transition,2-3}$	Number of iterations until transition from Δt_2 to Δt_3	50,000
$w_{transition}$	Width of the transition between time step tiers	1,000
$\delta\phi_{ADLR}$	ADLR convergence criterion	1.0 $\times 10^{-5}$ V
h_{LS}	Grid spacing for the level set calculations	1 grid point
W	Width of the interface for the domain parameters	1.4 grid points
$\Delta t'$	Dummy time step for level set calculations	1.6 $\times 10^{-3}$
δ	Smoothness of the smoothed sign function	$\sqrt{10}$ grid points
n_{redist}	Number of time steps between redistancing operations	100
δ_{dist}	Convergence tolerance for generating ξ	5.0×10^{-5}
N_{dist}^{init}	Maximum number of initial level set iterations	1 $\times 10^6$
N_{dist}^{redist}	Maximum number of redistancing iterations	75
w_{band}	Thickness of the extension band for interfacial variables	8

computational efficiency and are given in Table 4.2. The grid spacing, h, is chosen such that decreased grid spacing has minimal effect on the steady-state pore geometry. The grid spacing is dependent on ϕ_{app}, such that the pore barrier is resolved by approximately 180 grid points. The parameters controlling the time step size in eq (4.39) were selected such that smaller $\Delta t(i_{iter})$ had negligible effect on the solution. To adjust for the dependence of the growth velocity on the electrolyte pH and the dependency of h on ϕ_{app}, the values of Δt_1, Δt_2, and Δt_3 are written as $\Delta t_n = \alpha_n \frac{h}{v_{1D}}$ for $n = 1, 2, 3$, where v_{1D} is the steady-state interfacial velocity predicted from 1D sharp interface calculations (0.8, 0.4, and 0.2 nm/s for pH=1.0, 1.5, and 2.0, respectively). Small values of the Courant number, α_n, are required for stability. The ADLR convergence criterion, $\delta\phi_{ADLR}$, was chosen such that tighter tolerances lead to negligible differences in the pore geometry. The value of W was chosen such that there would be three to four points across the interface of ψ_e, ψ_m, and ψ_{ox}, for well-defined derivatives of the domain parameters across the interface. The level set

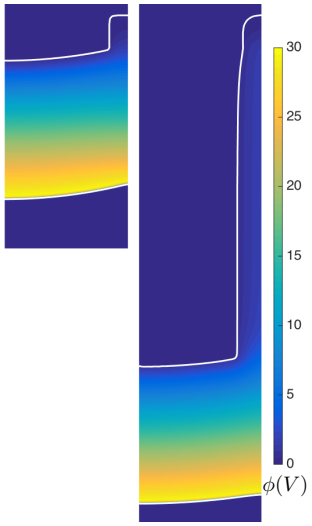

Figure 4.2: Plots of the pore morphology and ϕ at (a) the beginning and (b) the end of a simulation with $\phi_{app} = 40$ V in a 1 pH electrolyte. The white contours mark the boundaries of the oxide ($\psi_{ox} = 0.5$) and the color represents the value of ϕ within the oxide.

parameters, $\Delta t'$, δ, δ_{dist}, n_{redist} N_{dist}^{init}, and N_{dist}^{redist} were chosen to ensure stability and accuracy while minimizing interfacial drift.

4.5 Results

4.5.1 Pore Geometry as a Function of Electrolyte pH

Fig. 4.2 shows the initial and final film morphologies for a simulation with the preferred cell size at $\phi_{app} = 40$ V and an electrolyte pH of 1.0. The simulated pore has the characteristic shape of an anodic alumina nanopore with straight pore walls and curved interfaces near the pore base. The preferred cell size for this simulation and for two others with the same ϕ_{app} but with electrolyte pH values of 1.5 and 2.0

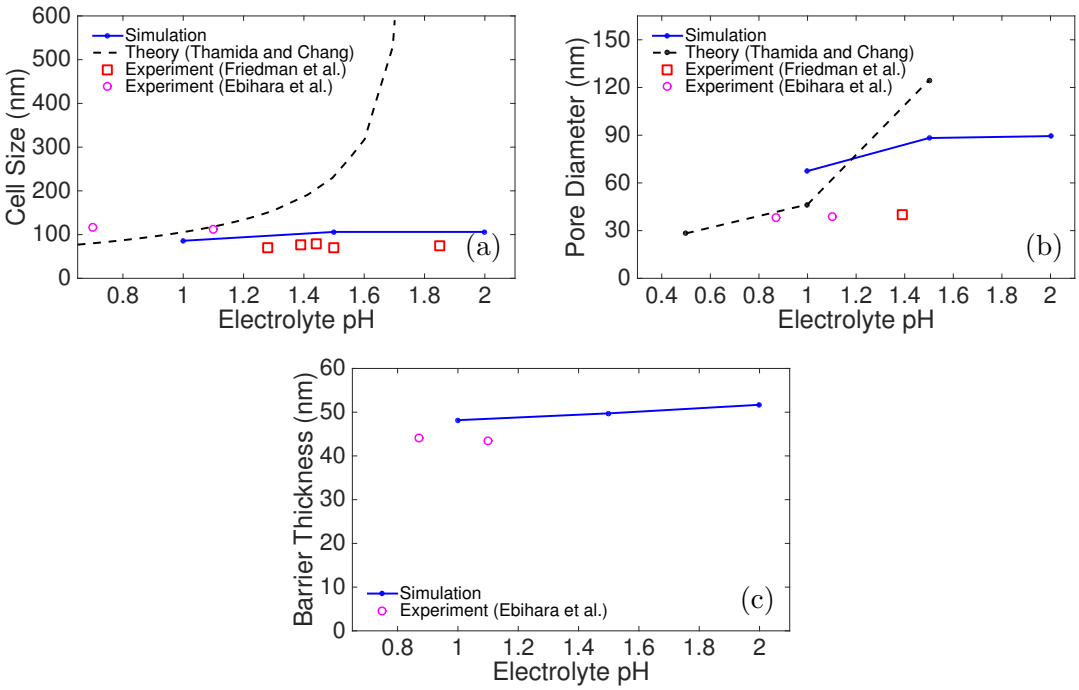

Figure 4.3: (a) Plots of the dependence of (a) the pore cell size, (b) the pore diameter, and (c) the barrier thickness with respect to pH for simulations conducted at $\phi_{app} = 40$ V. Where available, comparisons are included to the analytic result of Thamida and Chang and experimental results from Friedman et al. and Ebihara et al., all at $\phi_{app} = 40$ V.

are given in Fig. 4.3a. The theoretical relationship between the pore cell size and pH derived by Thamida and Chang[103] and experimental data measured by Friedman et al.[52] are also plotted in Fig. 4.3a. The simulated and experimental cell sizes are essentially constant as the pH varies. In contrast, Thamida and Chang predict that the cell size increases strongly for increasing pH, diverging at a pH value of 1.77.[103]

The simulated diameters as a function of electrolyte pH are given in Fig. 4.3b, along with 2D simulation results from Thamida and Chang[103] and experimental data from Friedman et al.[52] and Ebihara et al.[55] The simulated pore diameter is measured

at one quarter of the barrier thickness above the o/e interface at the center of the pore. Although there are only three experimental data points, they do not exhibit any noteworthy pH dependence. The simulated pore diameter increases from 1.0 to 1.5 pH, but then remains relatively constant from 1.5 to 2.0 pH, in contrast to Thamida and Chang's prediction that the pore diameter increases significantly from 1.0 to 1.5 pH. Although the trend with pH is improved over Thamida and Chang's prediction, the simulated pore diameter is systematically larger than the experimental measurements. This discrepancy is further discussed in Section 4.6.

Fig. 4.3c gives the simulated pore barrier thickness for varied electrolyte pH, along with experimental measurements by Ebihara et al.[55] The simulated pore barrier thickness is in good agreement with the available experimental data. The simulated barrier thickness becomes slightly thicker as the pH increases (increasing from 48 nm to 52 nm as the pH increases from 1.0 to 2.0), and the experimental barrier thickness is approximately constant at 44 nm.

4.5.2 Pore Geometry as a Function of Applied Potential

Fig. 4.4a gives the simulated preferred cell size for a 1.0 pH electrolyte for ϕ_{app} values of 10, 30, 40, and 60 V. Fig. 4.4a also plots Thamida and Chang's analytical prediction and experimental data from Friedman et al.[52] and Ebihara et al.[55] No data from Cheng and Ngan is provided in Fig. 4.4a because they did not calculate the cell size, but rather used experimental values as a model input. Both the simulations in this work and the theoretical results from Thamida and Chang are in good agreement with the experimental data, and exhibit a nearly linear increase in the cell size as

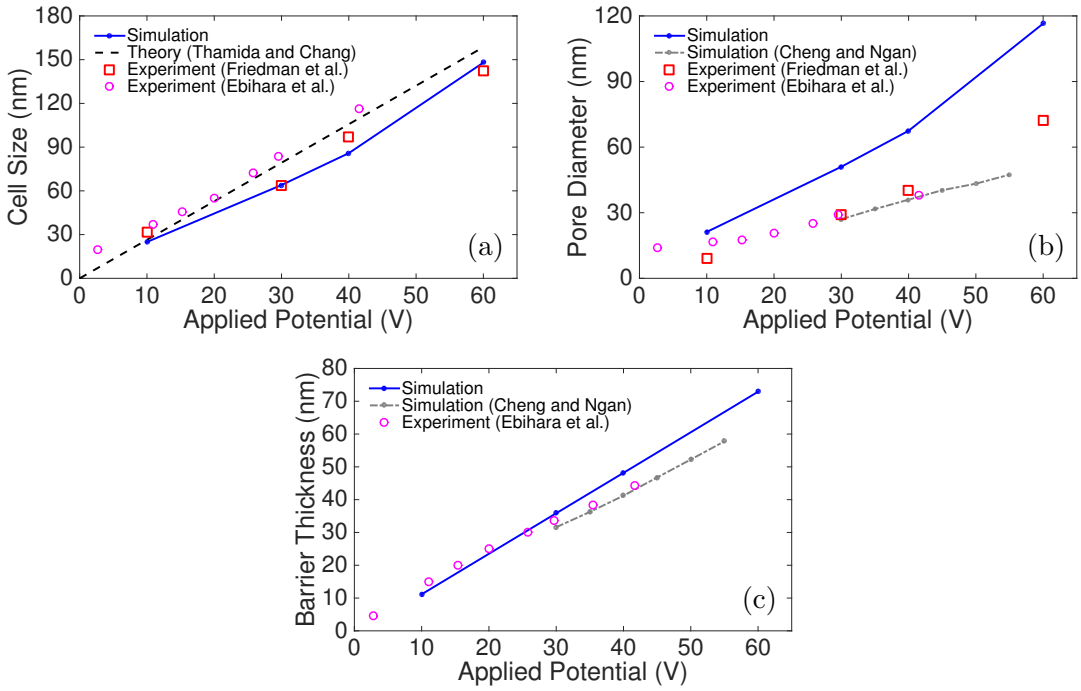

Figure 4.4: Plots of the dependence of (a) the pore cell size, (b) the pore diameter, and (c) the barrier thickness with respect to ϕ_{app} for simulations conducted at an electrolyte pH of 1.0. Where available, comparisons are included to simulation results from Cheng and Ngan (no pH given), the analytic result of Thamida and Chang (pH=1.0), and experimental results from Friedman et al. (oxalic acid, pH=1.39) and Ebihara et al. (oxalic acid, pH=0.87).

ϕ_{app} increases.

The simulated steady-state pore diameter as a function of ϕ_{app} is given in Fig. 4.4b, along with simulation results from Cheng and Ngan[104] and experimental data from Friedman et al.[52] and Ebihara et al.[55] As in the previous subsection, the simulated pore diameter is measured at one quarter of the barrier thickness above the o/e interface at the center of the pore. The simulated pore diameter increases with increasing ϕ_{app}, almost linearly, which is similar to the experimental data. However,

as in Section 4.5.1, the simulated pore diameter is systematically larger than the experimental measurements.

The simulated steady-state pore barrier thickness, measured at the pore center, as a function of ϕ_{app} is given in Fig. 4.4c, along with simulation results from Cheng and Ngan[104] and experimental data from Ebhihara et al.[55] As expected from the 1D simulations conducted in Chapter III, the barrier thickness increases linearly with the applied potential. The simulation results are in good agreement with the experimental data, although the simulations slightly overpredict the barrier thickness at high ϕ_{app}.

4.5.3 Comparison of the Pore Geometry for Pseudo-3D and 2D Calculations

The previous simulations were conducted using an axisymmetric pseudo-3D geometry. As noted by Parkhutik and Shershulsky,[102] the steady-state geometry is different between such pseudo-3D calculations and non-axisymmetric 2D calculations. For $\phi_{app} = 30$ V and an electrolyte pH of 1.0, a pseudo-3D calculations yields a cell size, pore diameter, and barrier thickness of 64 nm, 51 nm, and 36 nm, respectively. Under otherwise identical conditions, a 2D calculation yields a cell size, pore diameter, and barrier thickness of 46 nm, 31 nm, and 36 nm, respectively. Thus, the 2D simulation yields a preferred cell size 28% smaller and a pore diameter 38% smaller than the pseudo-3D simulation. The barrier thicknesses are comparable between the two simulations. The final pore morphology for both the pseudo-3D and 2D calculations can be found in Fig. 4.5.

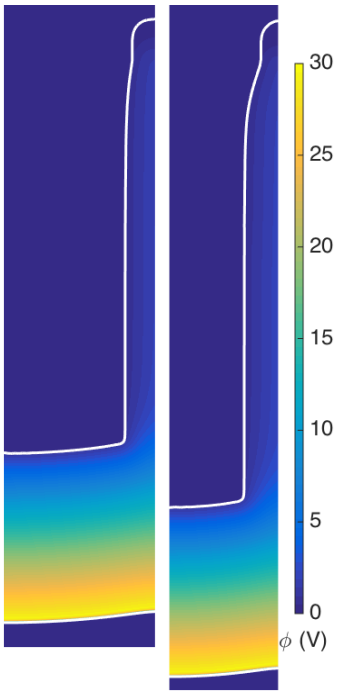

Figure 4.5: Plots of the pore morphology for a simulation with $\phi_{app} = 30$ V in a 1 pH electrolyte. (a) Pseudo-3D simulation. (b) 2D simulation.

In both the 2D and 3D calculations, the pore geometry focuses the electric field at the o/e interface and defocuses it at the m/o interface as a result of the solution of eqs (4.1) and (4.10). However, for a given pore cross-section, the curvature of the interfaces of the trench geometry for the 2D calculations is lower than for the pseudo-3D calculations, resulting in less geometric focusing/defocusing for the 2D calculations. Thus, in the 2D calculations, the geometry must adjust to obtain the same difference in $|E|$ between the o/e and m/o interfaces. Consequently, quantitative predictions of pore growth and self-ordering require 3D calculations. Simulations of multiple (nonidentical) pores, where the assumption of azimuthal symmetry cannot

be applied, would require a full 3D simulation, rather than the pseudo-3D simulations presented in this chapter. Therefore, unlike the 2D multipore simulations performed by Cheng and Ngan, full 3D simulations are necessary for quantitative simulations of interactions between nonidentical pores.

4.5.4 Pore Growth Rate

The simulated pore growth rate as a function of the electrolyte pH for $\phi_{app} = 10$ V is plotted in Fig. 4.6a, along with experimental data from Friedman et al.[52] The simulation results match the experimental trend of decreasing pore growth rate with increasing pH, although the decrease in the experimental data is more pronounced than in the simulations. This result demonstrates that the model does account for the change in the electrolyte pH in a manner consistent with experimental observation.

On the other hand, the simulations results do not reflect the observed dependence of the pore growth rate on ϕ_{app}. The simulated pore growth rate as a function of ϕ_{app} for a 1.0 pH electrolyte is plotted in Fig. 4.6b, along with experimental data from Friedman et al.[52] The simulated growth rate is independent of ϕ_{app}, while the experimental growth rate increases exponentially with ϕ_{app}. The simulation growth rate from Cheng and Ngan shows a very small dependence on ϕ_{app}, but is not sufficient to explain the experimentally observed increase, indicating that the discrepancy arises from a physical mechanism (or mechanisms) not considered in either model. In Section 4.6, we discuss the possible role of plastic flow in causing the experimentally observed increase in the growth rate as ϕ_{app} increases.

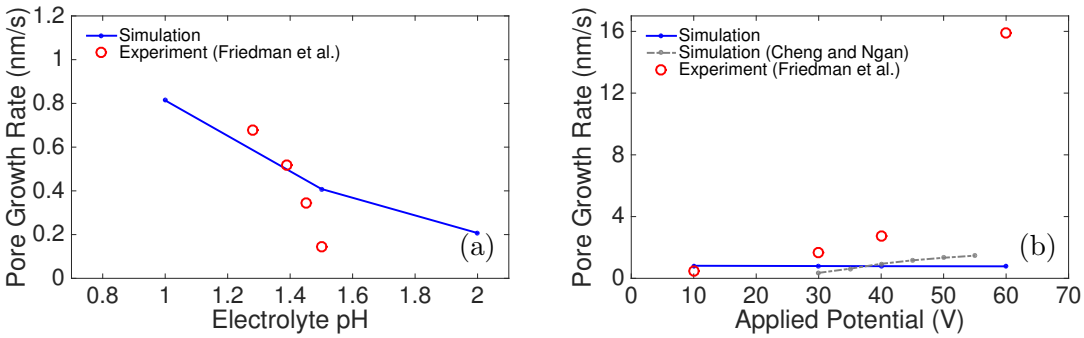

Figure 4.6: Plots of the dependence of (a) the electrolyte pH (for $\phi_{app} = 10$ V) on the simulated pore growth rate and (b) ϕ_{app} (for pH=1.0). Simulation results from Cheng and Ngan (no pH given) and experimental data from Friedman et al. ($\phi_{app} = 10$ V in (a) and pH=1.39 in (b)).

4.6 Discussion

4.6.1 Effect of Electrolyte pH

The success of our model in describing the effect of the electrolyte pH gives insight into role of adsorbed species in controlling the effect of the electrolyte pH. As first discussed by Våland and Heusler,[74] the electrolyte pH influences the oxidation and dissolution reactions at the o/e interface through the concentration of O^{2-} and OH^- adsorbed at the o/e interface. Previous models of anodization, including the models by Parkhutik and Shershulsky, Thamida and Chang, and Cheng and Ngan, assumed a simpler mechanism for the effect of electrolyte pH, that the oxide dissolution rate at the o/e interface was proportional to H^+ concentration in the electrolyte, 10^{-pH}. The divergence of the cell size with respect to pH reported by Thamida and Chang, suggests that this assumption is invalid. While the simpler mechanism yields an order of magnitude decrease in the dissolution rate as the pH increases from 1 to 2, our

simulation results presented in Fig. 4.6a, which do account for the adsorbed O^{2-} and OH^- concentrations, only show a decrease in the steady-state growth rate of a factor of 4. Thus, the equilibrium controlling the concentrations of adsorbed O^{2-} and OH^-, as described in eqs (4.16) and (4.17), moderates the effects of the changes to the electrolyte pH.

The relationship between the pH and the pore cell size can be understood in terms of the shifts in the equilibrium concentrations of adsorbed O^{2-} and OH^- as a function of pH. As discussed in Section 4.4, $\Delta|E|$ controls the preferred pore geometry, because it determines the level of geometric focusing/defocusing of the electric field required for ${}_{m/o}v$ to match the maximum value that can be attained by ${}_{o/e}v$. The effect of changing the pH on the peak value of ${}_{o/e}v$ can be observed through through plots of ${}_{o/e}v$ and ${}_{m/o}v$ as a function of $|E|$, shown in Fig. 4.7, which were generated using the 1D sharp interface calculations described in Chapter III. From Fig. 4.7, $\Delta|E|$ is 0.007 V/nm, 0.006 V/nm, and 0.005 V/nm at 1.0, 1.5, and 2.0 pH, respectively. In these simulations, nearly all of the anion sites in the adsorbed layer at the o/e interface are occupied by OH^- ions. As the pH increases, the equilibrium given by eqs (4.16) and (4.17) shifts in favor of higher ${}_{ad}c_{O^{2-}}$ and lower ${}_{ad}c_{V_{anion}}$, while ${}_{ad}c_{OH^-}$ remains relatively constant. By eq (4.13), these changes shift $R_{oxidation}$ toward film growth and away from dissolution, decreasing the downward velocity of the o/e interface, resulting in a slightly thicker barrier layer (as observed in Fig. 4.3c), which decreases $|E|$. As the peak ${}_{o/e}v$ decreases and shifts to lower $|E|$, the value of $|E|$ corresponding to ${}_{m/o}v$ where ${}_{m/o}v$ equals ${}_{m/o}v$ also decreases. Thus, although the electric field for the peak ${}_{o/e}v$ shifts by 0.055 V/nm (from 0.816 to 0.761 V/nm) from 1.0 to 2.0 pH,

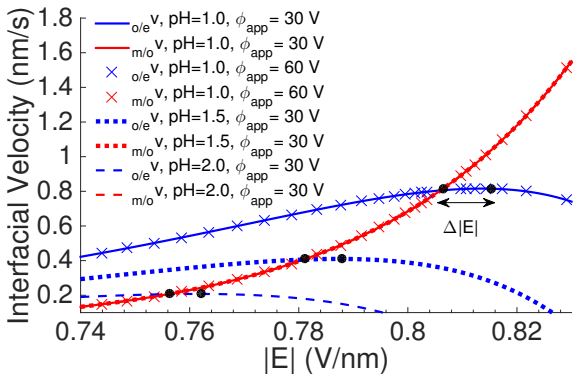

Figure 4.7: The $v(|E|)$ curves for electrolyte pH values of 1.0, 1.5 and 2.0. All ${}_{m/o}v$ collapse onto a single curve. The curves are identical for $\phi_{app} = 30$ V and $\phi_{app} = 60$ V. The maximum ${}_{o/e}v$ value and the corresponding ${}_{m/o}v$ value for each pH value is marked with a black dot. The difference in $|E|$ between the marked points gives $\Delta|E|$ for that pH.

the change in $\Delta|E|$ is only 0.002 V/nm across the range of pH examined, leading to the observed insensitivity of the cell size to pH.

4.6.2 Role of Plastic Flow

The steady-state pore growth rate is determined by the maximum possible value of ${}_{o/e}v$, as long as ${}_{m/o}v$ is not limiting the growth rate.[102,103] As seen in Fig. 4.7, our ${}_{m/o}v$ does not have a maximum as a function of $|E|$ because it depends on $|E|$ through a hyperbolic sine (eqs (4.9) and (4.19)). It can also be seen in Fig. 4.7 that ${}_{o/e}v$ is independent of ϕ_{app}. This is similar to previously published models by Parkhutik and Shershulsky[102] and Thamida and Chang,[103] where ${}_{o/e}v$ depends only on the electric field at the interface. For our model, this independence can be understood through the governing equations for ${}_{o/e}v$, which depend solely on a number of interfacial variables, ϕ at the o/e interface, and the electric field at the o/e interface. Therefore,

for any value of ϕ_{app}, the geometry of the pore will adjust until the variables at the o/e interface reach the values that maximize ${}_{o/e}v$. The clear discrepancy between this conclusion and the experimental observations indicate that our model, as well as the previous models by Parkhutik and Shershulsky and Thamida and Chang, are lacking a key physical mechanism involved in anodic growth.

Experimental tracer evidence[110] and simulations from Houser and Hebert[113] indicate that plastic flow, in addition to interfacial reactions, causes the o/e interface to evolve. Houser and Hebert's simulations predict that the oxide flows downward from the o/e interface and into the pore walls, which would correspond to an increase in ${}_{o/e}v$. The simulations from Ref. 113 also show that the flow rate increases as the current density increases (presumably coupled with an increase in ϕ_{app}). These results suggest plastic flow is responsible for the observed dependence of the pore growth rate on ϕ_{app}. The flow of oxide from the barrier region to the pore walls would also act to decrease the pore diameter relative to a system without plastic flow, providing a possible explanation for the overprediction of the pore diameters in this work.

4.6.3 Extraction of Kinetic Parameters with the Simulations

As discussed earlier in Section 4.4, the pseudo-3D simulations in this work permitted the unique determination of the system's kinetic parameters. Unlike the prior 1D simulations, the pseudo-3D simulations describe the pore geometry, allowing us to impose an additional constraint to the parameterization, the pore cell size. This example shows the utility of simulations for determining physical parameters that are difficult to access experimentally or from atomistic calculations, such as reaction

constants.

4.6.4 Extensions of the Model

The approach to simulating the growth of anodic alumina nanopores developed here can be extended to include other physical considerations. As the model stands, it could be applied to the simulation of multiple interacting pores, either in 2D (assuming a trench morphology) or 3D (e.g., a hexagonal nanopore array). The addition of plastic flow to the model, following the approach in Ref. 113, would allow an examination of the hypothesis proposed in Section 4.6.2 that the dependence of the growth rate on ϕ_{app} is a result of plastic flow. The model could also be extended to consider the incorporation and transport of anion impurities from the electrolyte. This extension would allow the simulation of anodized TiO_2 nanotube formation, where the presence of F^- impurities are believed to be critical in the separation of the nanotubes.[59] Finally, the general modeling approach from this work could be applied to other electrochemical systems involving time-dependent morphologies, including corrosion and electrodeposition.

4.7 Conclusion

We have presented a new multidimensional modeling framework to simulate the evolution of anodic alumina nanopores, building upon the 1D model we developed previously. This framework utilizes the smoothed boundary method to enforce boundary conditions at the oxide/electrolyte and metal/oxide interfaces and utilizes the level set method to track interfacial motion. The modeling framework was applied

to simulate the growth of individual nanopores in a pseudo-3D axisymmetric domain until the pores reached their steady-state geometry. We demonstrated that the preferred cell size for a given applied potential and electrolyte pH can be determined by identifying the cell size that leads to the fastest-growing stable pore.

We investigated the dependence of the steady-state pore geometry and the pore growth rate on the applied potential and the electrolyte pH. The simulations indicate that our model largely captures the experimentally observed dependencies of the pore geometry, although the simulations systematically overpredict the pore diameter. Furthermore, unlike previous models, the pore geometries in our simulations exhibits little dependence on the electrolyte pH, in agreement with experimental results, while still capturing the experimental trend of slower pore growth as the electrolyte pH increases. The improved pH-dependence is due to our model's treatment of the equilibrium processes governing the concentrations of adsorbed O^{2-} and OH^{-}. Like other models of anodization where the interfacial motion is solely due to interfacial reactions, our model does not capture the exponential relationship between the growth rate and the applied current, which is suggested to be due to a lack of plastic flow in the model. Simulations of the preferred pore geometry for pseudo-3D calculations and 2D calculations indicate that 2D calculations yield a substantially smaller preferred cell size and pore diameter, and thus 3D calculations are needed for quantitative predictions of anodic nanostructure growth.

The model presented here can now be applied for further investigations of the growth of anodic nanopores, including interactions between pores. The model is formulated to be easily extensible, and thus new mechanisms such as plastic flow or

the incorporation of impurities from the electrolyte can be added to further elucidate the mechanisms governing anodic nanostructure growth and self-ordering.

CHAPTER V

Rechargeable Magnesium Batteries: Background

5.1 Mg Batteries as a Successor to Li-Ion Batteries

Magnesium batteries have garnered substantial attention as a successor to Li-ion batteries due to their potential for high energy density and safe operation.[34,203,204] Metallic Mg anodes provide a substantially higher specific volumetric capacity (3833 mA h/cm^3) than either Li-graphite anodes (760 mA h/cm^3) or metallic Li anodes (2046 mA h/cm^3).[34] Furthermore, unlike metallic Li anodes,[205] metallic Mg anodes can be cycled without the formation of dendrites.[35] Dendrite growth poses a hazard because dendrites can grow across the separator to the cathode and short the battery, leading to thermal runaway.[205,206] Instead of forming dendrites, metallic Mg anodes form compact, faceted films, practically eliminating this risk.[35] Understanding the evolution of this Mg film during cycling is a critical factor in the development of high-performance magnesium batteries.[207]

5.2 Morphology of Isolated Mg Deposits

Although the development of electrolytes for the efficient and reversible deposition and dissolution of Mg has been pursued extensively (see Refs. 204 and 34 for comprehensive reviews on this topic), much less attention has been given to the morphological evolution of the Mg deposits during cycling. SEM and AFM images of the Mg film typically show a highly faceted film with grains on the order of 1 μm in width.[208–211] However, other morphologies with either larger[210] or smaller[212,213] features have also been observed.

A comprehensive examination of the morphology of electrodeposited Mg was conducted by Matsui,[35] who examined the morphology of 1 C/cm^2 of Mg deposited at 0.5, 1, and 2 mA/cm^2. At 0.5 and 1 mA/cm^2, he observed very similar morphologies: round faceted grains 2-3 μm in diameter. In contrast, at 2 mA/cm^2, he observed a different morphology: triangular grains with sizes 0.5-1 μm. This transition in the morphology coincides with a change in preferred orientation from (0001) at 0.5 and 1 mA/cm^2 to (1010) at 2 mA/cm^2, determined from X-ray diffraction. Matsui also examined the film morphology for a smaller amount of deposited Mg (0.25 C/cm^2) and observed a large number of equally sized faceted spheres with a diameter of approximately 1.5 μm. Matsui hypothesized that Mg does not form dendrites because the electrolyte surrounding a newly formed nucleus is depleted to the point that nucleation at another point on the substrate is favored over deposit growth. Consequently, a high density of deposits forms on the surface prior to substantial growth. This even coverage of deposits prevents the current localization that leads to dendrite growth. Other mechanisms for the suppression of dendrites during Mg

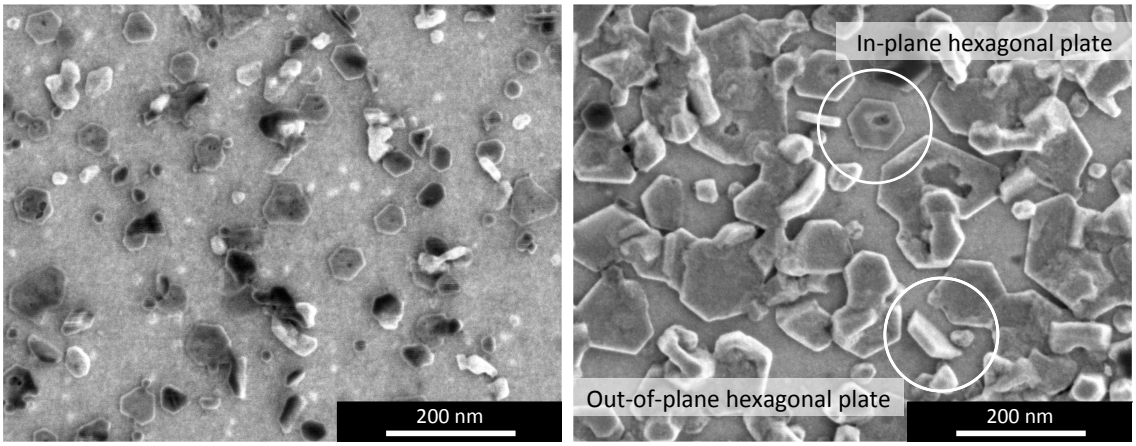

(a) (b)

Figure 5.1: SEM images of Mg deposited on a (111) Au surface after (a) 5 seconds of deposition (b) 20 seconds of deposition at 1.5 mA/cm^2. Examples of in-plane and out-of-plane hexagonal plates are circled. These figures are reproduced from Ref.[216]

deposition have been suggested, including faster surface diffusion[34,214] and higher bond strength,[215] as compared to Li.

Recent experiments by Hahn and Zavadil[216] investigated the morphology of isolated Mg deposits, observing strongly faceted These Mg deposits were grown on a highly textured Au (111) substrate in a 0.4 M "all-phenyl-complex" (APC) electrolyte.[217] The morphology of Mg deposits grown at approximately 1.5 mA/cm^2 can be seen in Fig. 5.1. After 5 seconds of growth, many of the deposits have not yet merged and have a faceted plate morphology with a broad facet on top and short faceted sides. The angles between most of the side facets are approximately 120°. The characteristic size for the deposits can be defined as the length of the shortest line through the center of the deposit crossing from one side of the deposit to another. Using this metric and sampling over a 500 nm × 500 nm area, the characteristic size after 5 seconds of growth ranges from approximately 10 to 60 nm. The maximum

spacing between deposit centers is approximately 100 nm. After 20 seconds of growth, most of the deposits have merged, creating a less well-defined deposit morphology. However, the faceted surface and the 120° angles between side facets are still present. The characteristic size of the deposits is now ranges from approximately 10 to 160 nm. Two primary morphologies dominate at this stage: in-plane and out-of-plane hexagonal plates (with respect to the substrate surface). An example of each of these morphologies is circled in Fig. 5.1b. The out-of-plane hexagonal plates vary in their orientation from deposits with broad facets that are perpendicular to the substrate to deposits that are tilted by approximately 30° from the normal of the substrate.

5.3 Previous Models of Electrodeposition and Crystal Growth and Their Relevance to Mg Battery Anodes

Simulations of Mg electrodeposition and electrodissolution may yield insight into mechanisms underlying these experimental observations of Mg film morphology and can provide a tool to predict anode morphology during cycling. Several models of electrodeposition can be found in the literature. Wheeler, Josell, and Moffat developed a two-dimensional (2D) model of copper electrodeposition using the level set method to track the moving interface.[32] This model accounts for the evolution of the concentration in the electrolyte, the reaction kinetics through the Butler-Volmer equation, and the effect of adsorbed accelerator species. Guyer et al. developed a one-dimensional (1D) phase field model for electrodeposition.[26,27] This model accounts for the concentration evolution in the electrolyte, the charge separation in the interfacial double layer, and the variation of the electric potential in the

electrolyte. The thermodynamic underpinnings of this model provide a overpotential-current relationship consistent with Butler-Volmer kinetics. Ely, Jana, and Garcia[25] developed a 2D phase field model similar to the Guyer et al. model, but assumed a constant electrolyte concentration and explicitly used Butler-Volmer kinetics to model the reaction rate.

Many aspects of these models are applicable to Mg electrodeposition and electrodissolution, including Butler-Volmer reaction kinetics, electrolyte concentration evolution, and spatial variation of the potential in the electrolyte. However, unlike these previous models, evolution should be simulated in three dimensions (3D) to capture the 3D morphology of the deposits, which do not exhibit the rotational or translational symmetry that allows simplification to 1D or 2D. Furthermore, none of these models provide a framework for the formation and evolution of the facets observed experimentally.

A formulation for modeling facet formation and evolution was developed for quantum dot growth via selective area epitaxy, taking a phase-field approach.[218,219] An orientation-dependent growth rate in the phase field equation leads to a faceted deposit morphology. The deposit morphology conforms to the shape predicted by the kinetic Wulff construction,[220] where the outwardly growing facets correspond to slow growth rate orientations and inwardly growing facets correspond to fast growth rate orientations. The model was implemented using the smoothed boundary method. The smoothed boundary method is a diffuse interface numerical method to restrict the solution of an equation to a particular subdomain within the computational domain and enforces boundary conditions along the boundary of the subdomain.[21]

In Refs. 218 and 219, the smoothed boundary method is used to separate the vapor and deposit subdomains from the substrate subdomain.

CHAPTER VI

Phase-Field Model for the Electrodeposition and Electrodissolution of Magnesium

6.1 Introduction

In this chapter, we present a new model of electrochemical morphology evolution using a combination of the approaches presented in Refs. 218 and 9. This diffuse interface model includes many aspects of previous electrodeposition models including Butler-Volmer reaction kinetics, electrolyte concentration evolution, and a non-uniform distribution of the potential in the electrolyte. This new model is presented in Section 6.2. The smoothed boundary method formulation and finite difference numerical implementation of the model are presented in Section 6.3. Simulation results and their implications are discussed in Section 6.4. Finally, the conclusions are presented in Section 6.5.

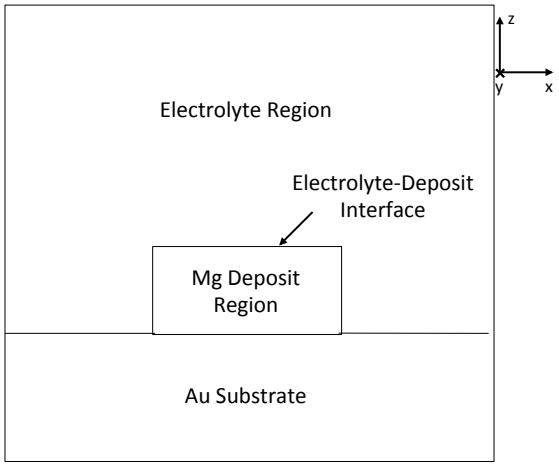

Figure 6.1: Schematic 2D diagram of the model system.

6.2 Model

6.2.1 Continuum Model for the Electrochemical Evolution of Faceted Deposits

In order to simulate the evolution of faceted Mg deposits, we have developed a new model of electrodeposition and electrodissolution. This model can be separated into three coupled models, each describing a different region of the system: the electrolyte-deposit interface, the electrolyte, and the Mg deposit. A schematic diagram of the system is given in Fig. 6.1.

The deposition/dissolution reaction occurs at the electrolyte-deposit interface. For simplicity, we assume that the dominant overall reaction is

$$Mg^{2+}(l) + 2e^{-}(s) \rightleftharpoons Mg(s) \tag{6.1}$$

If we assume that the first electron transfer during deposition is much faster than the

second electron transfer during deposition,[34] the current associated with this reaction, i_{rxn}, can be given by a Butler-Volmer expression[2]

$$i_{rxn} = k_{dep} c_{ion}^{int} \exp\left(\frac{-\beta F(\phi_{we} - \phi_{int})}{RT}\right) - k_{dis} \exp\left(\frac{(2-\beta)F(\phi_{we} - \phi_{int})}{RT}\right) \quad (6.2)$$

where F is Faraday's constant, k_{dep} is the rate constant for deposition, k_{dis} is the rate constant for dissolution, c_{ion}^{int} is the concentration of Mg^{2+} in the electrolyte at the electrolyte-deposit interface, β is the symmetry factor, R is the gas constant, and T is the temperature. The potential of the working electrode (the combination of the substrate and the deposit) is assumed to be spatially constant and is given by ϕ_{we}. The potential on the electrolyte side of the electrolyte-electrode interface is denoted by ϕ_{int}.

In general, k_{dep} and k_{dis} can depend on the local orientation of the Mg deposit. This orientation-dependence can take the form of

$$k_{dep} = k_{dep}^{*} \tilde{k}_{dep}(\theta_1, \theta_2) \quad (6.3)$$

$$k_{dis} = k_{dis}^{*} \tilde{k}_{dis}(\theta_1, \theta_2) \quad (6.4)$$

where k_{dep}^{*} and k_{dis}^{*} are rate coefficients set by the exchange current density and $\tilde{k}_{dep}$ and $\tilde{k}_{dis}$ are anisotropy functions that describe the orientation-dependence of the reaction rate. The local deposit orientation is described by two angles, θ_1 and θ_2: θ_1 is the angle between the deposit surface normal and the plane of the substrate, and θ_2 is the azimuthal angle, which is taken to be the angle between the x-axis and the projection of the deposit surface normal onto the plane of the

substrate. The anisotropy functions can be further separated into the product of functions solely dependent on either θ_1 or θ_2: $\tilde{k}_{dep}(\theta_1, \theta_2) = \tilde{k}_{dep1}(\theta_1)\tilde{k}_{dep2}(\theta_2)$ and $\tilde{k}_{dis}(\theta_1, \theta_2) = \tilde{k}_{dis1}(\theta_1)\tilde{k}_{dis2}(\theta_2)$. The orientation-dependence of k_{dep} and k_{dis} can lead to the formation of facets on the deposit. Therefore, k_{dep} and k_{dis} are similar to the orientation-dependent growth velocity in Ref. 218, except that the growth velocity in this model also depends on the other variables in eq (6.2). Two possible models relating $\tilde{k}_{dep}$ and $\tilde{k}_{dis}$ will be discussed in Subsection 6.2.2.

In the electrolyte, we calculate the distribution of the electric potential and the evolution of the concentration of the active species. Although the speciation of the electrolytes used for Mg deposition and dissolution is often quite complex,[204] in the interest of simplicity, we assume that the active species in the electrolyte are Mg^{2+} and A^{2-}, where A is a generic divalent anion. Applying the usual assumption of bulk electroneutrality,[2] the concentrations of these two species are equal throughout the electrolyte and given by c_{ion}. Following the typical derivation for a dilute binary electrolyte,[2] the evolution of the concentration is given by

$$\frac{\partial c_{ion}}{\partial t} = \nabla \cdot (D \nabla c_{ion}) \tag{6.5}$$

where $D = (z_{Mg} u_{Mg} D_A - z_A u_A D_{Mg})/(z_{Mg} u_{Mg} - z_A u_A)$, $z_{Mg} = 2$ is the valence of the Mg cation, $z_A = -2$ is the valence of A, u_{Mg} is the mobility of the Mg ions, u_A is the mobility of the A ions, D_{Mg} is the diffusivity of the Mg ions, and D_A is the diffusivity of the A ions. The mobilities of the Mg and A ions, u_{Mg} and u_A, can be expressed in terms of their diffusivity through the Nernst-Einstein relation:[2] $u_{Mg} = D_{Mg}/RT$ and $u_A = D_A/RT$. Also from the typical treatment of a dilute binary electrolyte,[2] the

distribution of the potential is given by a current continuity relation:

$$\nabla \cdot \mathbf{i} = -z_{Mg} F \nabla \cdot [(z_{Mg} u_{Mg} - z_A u_A) F c_{ion} \nabla \phi + (D_{Mg} - D_A) \nabla c_{ion}] = 0 \qquad (6.6)$$

Equations (6.5) and (6.6) are solved only within the electrolyte.

According to the reaction in eq (6.1), the flux of A^{2-} at the electrolyte-deposit interface is zero and the flux of Mg^{2-} at the electrolyte-deposit interface is equal to the reaction flux. The combination of these two flux expressions yield the following flux relation at the electrolyte-deposit interface:[9]

$$\mathbf{J} \cdot \mathbf{n} = -\frac{(1 - t_{Mg}) i_{rxn}}{z_{Mg} F} \qquad (6.7)$$

where $\mathbf{J} \cdot \mathbf{n}$ is the ionic flux at the electrolyte-deposit interface and $t_{Mg} = (z_{Mg} u_{Mg})/(z_{Mg} u_{Mg} - z_A u_A)$ is the Mg transference number.

The evolution of the Mg deposit is modeled using a phase field approach similar to that used to model InGaN quantum dot growth by selective area epitaxy.[218,219] As in many previous publications,[218,219,221–224] the phase field model is applied as a computational model to track the interfacial position, rather than as a physical model of phase transformation. The region occupied by the Mg deposit is described by a phase field parameter, $c_{deposit}$, where $c_{deposit} = 1$ within the deposit and $c_{deposit} = 0$ outside the deposit. Therefore, $c_{deposit}$ can be thought of as the normalized concentration of metallic Mg.

The evolution of $c_{deposit}$ is given by the Cahn-Hilliard equation[225] with a source

term, $vBc_{deposit}^2(1-c_{deposit})^2$, to account for deposition or dissolution:[218,219,221,222]

$$\frac{\partial c_{deposit}}{\partial t} = \nabla \cdot \left[M(c_{deposit}) \nabla \left(\frac{\partial f}{\partial c_{deposit}} - \kappa^2 \nabla^2 c_{deposit} \right) \right] + vBc_{deposit}^2(1-c_{deposit})^2 \tag{6.8}$$

where $M(c_{deposit})$ is the mobility of Mg in the deposit, f is the bulk free energy density, κ is the gradient energy coefficient, which adds an energetic penalty for interfaces between the deposit and the electrolyte, v is the normal velocity of the interface, and B is a normalization factor. The Mg mobility along the surface of the deposit is expected to be much higher than the mobility through the bulk. Therefore, as in Ref. 218, we define $M(c_{deposit}) = M_s c_{deposit}^2(1-c_{deposit})^2$, where M_s is the surface mobility of Mg. Sharp interface analysis demonstrates that this formulation of the mobility is equivalent to surface diffusion along the electrolyte/deposit interface in the sharp interface limit.[221]

Following the derivation in Ref. 218, the bulk free energy density is modeled by $f(c_{deposit}) = Wc_{deposit}^2(1-c_{deposit})^2$. This free energy function has minima at $c_{deposit} = 0$ and $c_{deposit} = 1$ and an energetic barrier of height $W/16$ at $c_{deposit} = 0.5$. Thus, the free energy function promotes phase separation, with regions where $c_{deposit}$ is either 0 or 1. The gradient energy penalty term, $\kappa^2 \nabla^2 c_{deposit}$, penalizes a sharp transition between these two regions, thus generating a thin interfacial region of finite thickness with intermediate values of $c_{deposit}$.

The normal velocity is determined by a combination of eq (6.2) and Faraday's law:

$$v = \frac{i_{rxn}\Omega_{Mg}}{z_{Mg}F} \tag{6.9}$$

where Ω_{Mg} is the molar volume of Mg. The normalization factor, $B = \sqrt{72W}/\kappa$, is determined from a sharp interface analysis.[221] The expression $c^2_{deposit}(1 - c_{deposit})^2$ is nonzero only near the interface and thus the source term is limited to the interface.

Equation (6.8) is solved only in the deposit and the electrolyte, and the substrate is assumed to be stationary throughout the process.

6.2.2 Two Models of Reaction Rate Orientation Dependence

The orientation-dependence of the reaction rate, as represented by $\tilde{k_{dep}}$ and $\tilde{k_{dis}}$ in our model, could be a result of orientation dependence in one of several properties for the electrolyte-deposit interface including: the kink-site density of the Mg surface, the existence and thickness of a passivation layer on the deposit, or the Mg ion's adsorption/desorption energy. These sources of orientation dependence may be symmetric (with respect to the reaction direction), i.e. $\tilde{k}_{dis} = \tilde{k}_{dep}$, or asymmetric, e.g. reciprocal where $\tilde{k}_{dis} = 1/\tilde{k}_{dep}$.

The kink-site density and the passivation layer thickness, $\tilde{k}_{dep}$ and $\tilde{k}_{dis}$ are expected to be symmetric sources because the reactivity of the Mg planes is due to properties of the planes that affect the reaction rate equally in both the deposition and dissolution reactions. If the orientation dependence is due to the adsorption/desorption energy, $\tilde{k}_{dep}$ and $\tilde{k}_{dis}$ can be represented as the exponential functions $\tilde{k}_{dep} = \exp(\Delta E_a/RT)$ and $\tilde{k}_{dis} = \exp(-\Delta E_a/RT)$, where ΔE_a is the adsorption energy. Thus, the anisotropy functions are expected to have a reciprocal relationship: $\tilde{k}_{dis} = 1/\tilde{k}_{dep}$. Both models have been examined in our simulations, and the effect of using a symmetric versus a reciprocal orientation dependence is discussed in Subsection 6.4.5.

6.2.3 Physical Input Parameters

The physical parameters used in our model are given in Table 6.1. The source of each of these parameters is briefly described below.

In eq (6.8), the barrier height coefficient and gradient penalty coefficient, W and κ respectively, were selected such that the equilibrium profile of $c_{deposit}$ has approximately four points in the interface. Both variables are normalized by a characteristic energy density, leaving W dimensionless and κ with units of nm. The value of $M_s = 6 \times 10^{-12} cm^2/s \times \frac{i_{app}}{1\ mA/cm^2}$ is selected such that there is sufficient diffusion for $c_{deposit}$ to maintain a smooth profile but not so much diffusion that the facets become rounded. The contact angle between the Mg deposit and the substrate, θ, is set to be 90°, based on top-down SEM images of Mg deposits (see Subsection 5.2).

In eq (6.5), the diffusion constants for the electrolyte species, D_{Mg} and D_A, are set in accordance with the measurements in Ref. 226 that were conducted for a 0.4 M C_2H_5MgCl-$((C_2H_5)_2Al\ Cl)_2$/THF electrolyte. For consistency with this experimental system, c_{ion}^{bulk} is set to 0.4 M.

In eq (6.2), we make the common assumption that the change in energy barriers for the deposition and dissolution reactions are equally affected by the applied potential, and therefore we take $\beta = 0.5$.[2] The values for k_{dep}^* and k_{dis}^* are estimated using the isotropic exchange current density, i_0, and the relationship between k_{dep}^* and k_{dis}^* at 0V vs. a magnesium reference electrode. To relate the experimental value of the exchange current density, 1 mA/cm^2,[227] to k_{dep}^* and k_{dis}^*, we define the isotropic exchange current density, $i_0 = (k_{dep}^*)^{\beta}(k_{dis}^*)^{(1-\beta)}(c_{ion}^{bulk})^{\beta}$, where we assume the electrolyte is in the well-stirred limit ($c_{ion}^{int} = c_{ion}^{bulk}$). To complete the parameterization of k_{dep}^* and k_{dis}^*,

Model Parameter:	Value:	
W	1	
κ	1 nm	
M_s	6 $\times 10^{-12}$ cm^2/s $\times \frac{i_{app}}{1\ mA/cm^2}$	
θ	90°	
D_{Mg}	3×10^{-9} cm^2/s	Ref. 226
D_A	3×10^{-9} cm^2/s	Ref. 226
c_{ion}^{bulk}	0.4 M	
β	0.5	
k_f^*	2.5 mA/cm$^2 \cdot M$	
k_b^*	1 mA/cm^2	
T	300 K	
Ω_{Mg}	14 cm^3/mol	Ref. 228

Table 6.1: Model Parameters

we note that current is approximately zero at 0 V,[210,226] and thus $k_{dis}^* \approx k_{dep}^* c_{ion}^{bulk}$ from eq (6.2). We assume $T = 300$K and that the molar volume of Mg, Ω_{Mg} in eq (6.9), is 14 cm^3/mol.[228]

6.3 Computational Methods and Numerical Parameters

The governing equations, eqs (6.2), (6.5), (6.6) and (6.8), are solved in a computational domain containing regions that evolve in time. In Ref. 218, the boundary condition between the growing quantum dot and the immobile substrate was applied using the smoothed boundary method (SBM). The SBM is designed to restrict the solution of an equation to a subdomain within the larger computational domain and to efficiently apply boundary conditions along the boundary of that subdomain.[21] Like phase-field methods, the SBM is a diffuse interface method where a domain parameter defines the location of the subdomain and smoothly transitions between a

value of 1 inside the subdomain and a value of 0 outside the subdomain.

Written in SBM form, eq (6.8) becomes[21,218]

$$\frac{\partial c_{deposit}}{\partial t} = \frac{1}{\psi}\nabla\cdot\left[\psi M(c_{deposit})\nabla\left(\frac{\partial f}{\partial c_{deposit}} - \frac{\kappa^2}{\psi}\left(\nabla\cdot\psi\nabla c_{deposit} + \frac{|\nabla\psi|\sqrt{2f}}{\kappa}\cos\theta\right)\right)\right] + vBc_{deposit}^2(1-c_{deposit})^2 \quad (6.10)$$

where ψ is a domain parameter with $\psi = 1$ in the electrolyte and Mg deposit and $\psi = 0$ in the substrate. The SBM is used to ensure that eq (6.8) is solved only in the electrolyte and Mg deposit.

Periodic boundary conditions are applied on the surfaces of the computational domain perpendicular to the surface of the substrate for eq (6.10). A no-flux boundary condition is applied at the top surface of the computational domain (the boundary between the computational domain and the bulk electrolyte). As in Ref. 218, the SBM is used to enforce a no-flux boundary condition along the substrate interface and to enforce a contact angle boundary condition, θ, at the triple phase boundary between the electrolyte, the deposit, and the substrate. The contact angle is determined by the balance of interfacial tensions between the three phases.[229]

As in Ref. 218, a curvature cutoff, H_c, is applied to prevent excess deposition/dissolution at the intersections between facets. These intersections are rounded, an artifact of the diffuse interface approach, leading to rate constants much higher than on the facets. The curvature, H, is given by the divergence of the interfacial

normal vector of the Mg deposit:

$$H = \nabla \cdot \mathbf{n} = \nabla \cdot \left(\frac{\nabla c_{deposit}}{|\nabla c_{deposit}|} \right) \tag{6.11}$$

Based on this definition of the curvature, concave portions of the Mg deposit surface have positive curvature. During deposition, the rate constants k_{dep} and k_{dis} are set to zero in areas of high convex curvature, where the curvature is negative and greater in magnitude than H_c. Conversely, during dissolution deposition, k_{dep} and k_{dis} are set to zero in areas of high concave curvature, where the curvature is greater than H_c.

The SBM is also used to solve eqs (6.5) and (6.6) only in the electrolyte. The SBM form these equations were obtained from Ref. 9:

$$\frac{\partial c}{\partial t} = \frac{1}{\psi_l} \nabla \cdot (\psi_l D \nabla c) - \frac{|\nabla \psi_l|}{\psi_l} \frac{i_{rxn}(1 - t_{Mg})}{z_{Mg} F} \tag{6.12}$$

$$\nabla \cdot [\psi_l (z_{Mg} u_{Mg} - z_A u_A) F c \nabla \phi] + |\nabla \psi_l| \frac{i_{rxn}}{z_{Mg} F} = \nabla \cdot [\psi_l (D_A - D_{Mg}) \nabla c] \tag{6.13}$$

The domain parameter for the electrolyte, ψ_l, can be found by the simple relation $\psi_l = \psi(1 - c_{deposit})$.

To prevent current from erroneously flowing through the substrate-electrolyte interface near the substrate-electrolyte-deposit triple phase boundary, the boundary given by ψ_l must be decomposed into two regions: the substrate-electrolyte interface and the deposit-electrolyte interface. The expression localizing the boundary condition in eqs (6.14) and (6.15), $|\nabla \psi_l|$, can thus be separated into $|\psi \nabla (1 - c_{deposit})| + |(1 - c_{deposit}) \nabla \psi|$. Along the substrate-electrolyte interface, i_{rxn} is assumed to be zero and therefore the second term can be dropped, leaving the boundary terms proportional

to $|\psi\nabla(1-c_{deposit})|i_{rxn}$:

$$\frac{\partial c}{\partial t} = \frac{1}{\psi_l}\nabla\cdot(\psi_l D\nabla c) - \frac{|\psi\nabla(1-c_{deposit})|}{\psi_l}\frac{i_{rxn}(1-t_{Mg})}{z_{Mg}F} \tag{6.14}$$

$$\nabla\cdot[\psi_l(z_{Mg}u_{Mg}-z_A u_A)Fc\nabla\phi] + |\psi\nabla(1-c_{deposit})|\frac{i_{rxn}}{z_{Mg}F} = \nabla\cdot[\psi_l(D_A-D_{Mg})\nabla c] \tag{6.15}$$

Periodic boundary conditions are applied on the surfaces of the computational domain perpendicular to the surface of the substrate for both eqs (6.14) and (6.15). The top surface of the domain is taken to be the reference for the potential and is set to 0 V. To simulate galvanostatic processes with an applied current, i_{app}, we systematically select ϕ_{we} using a bisection scheme until the total reaction current is within $\delta_i \cdot i_{app}$ of i_{app}, where δ_i is the convergence tolerance. The boundary condition for ϕ in eq (6.6) along the electrolyte-electrode interface is $\phi = \phi_{int}$, where ϕ_{int} is calculated such that $i_{rxn} = \mathbf{i}\cdot\mathbf{n}$ at the electrolyte-electrode interface. The value of c_{ion} at the top surface of the computational domain is fixed at the bulk electrolyte value, c_{ion}^{bulk}.

The SBM formulations of the governing equations are solved using a finite difference scheme. Equation (6.10) is discretized using the semi-implicit Crank-Nicolson scheme and is solved using the Gauss-Seidel method with red-black ordering. Equation (6.14) is spatially discretized using second-order central finite differencing and is temporally discretized using the backward (implicit) Euler method. The resulting matrix equation is solved using successive overrelaxation (SOR) with Chebyshev acceleration.[230] Equation (6.15) is discretized using second-order central finite differencing, and, like

eq (6.14), is solved using SOR with Chebyshev acceleration.

The computational expense of solving the model equations can be substantially reduced by replacing the full 3D equations governing the electrolyte with their corresponding 1D approximations away from the surface of the working electrode. The computational domain must extend far enough in the z direction such that the concentration at the far edge of the cell does not deviate from the bulk value. To accomplish this, the domain must be larger than the diffusion length (approximately 1,000 nm for a 1 s simulation). For most of this domain, the variation of c_{ion} and ϕ in the x-y plane is expected to be negligible and the electrolyte can be modeled as a 1D system. The full 3D treatment is necessary only within a few tens of nanometers of the substrate. Therefore, we split the computational domain into two parts. Within a distance L_{3D} of the working electrode, we solve the full 3D equations as given by eqs (6.10), (6.14) and (6.15). For the remaining part of the computational domain with length L_{1D}, we solve the 1D analogs of eqs (6.5) and (6.6). Both of these 1D equations are solved implicitly using the tridiagonal matrix algorithm. The values of c_{ion} and ϕ on the substrate side of the 1D domain are used as boundary conditions for the top of the 3D domain. Solving the 1D analog of eq (6.10) is unnecessary because $c_{deposit}$ is uniformly zero in the 1D domain.

Each of $\tilde{k}_{dep1}(\theta_1)$, $\tilde{k}_{dep2}(\theta_2)$, $\tilde{k}_{dis1}(\theta_1)$, and $\tilde{k}_{dis2}(\theta_2)$ is tabulated in a lookup table with an interval of 1°. The values of $\tilde{k}_{dep}(\theta_1, \theta_2)$ and $\tilde{k}_{dis}(\theta_1, \theta_2)$ are determined by a linear interpolation between the tabulated values. To prevent small errors in the calculation of the orientation of a facet from causing a drastic change in the anisotropy functions, the value within ±2° of each facet orientation is set to the value at the tip

of the cusp.

The finite difference calculations were parallelized using Message Passing Interface (MPI). A typical simulation took two hours using 128 2.67 GHz computing cores.

The numerical parameters for our simulations are given in Tables 6.2 and 6.3. Unless otherwise stated, the 3D domain is 100 nm $\times$ 100 nm $\times$ 75 nm and is discretized into an even grid of 128 points $\times$ 128 points $\times$ 96 points. The length of the 1D domain, L_{1D}, is 9,000 nm and is discretized into $N_{1D} = 500$ points with linearly increasing grid spacing. The i^{th} point of the 1D grid is given by

$$z_{1D}(i) = \frac{(L_{1D} - N_{1D}\Delta z_{3D})}{N_{1D}^2} i^2 + \Delta z_{3D} i + L_{3D} \tag{6.16}$$

where Δz_{3D} is the grid spacing in the 3D domain.

At the beginning of each simulation, the electrolyte concentration is uniformly equal to the bulk value. During deposition H_c was set to -0.13 nm^{-1}, and during dissolution it was set to 0.03 nm^{-1}. These cutoffs were chosen such that the misorientation of the facets is generally less than 3° and the artificial rounding of the facet corners is limited. Each simulation has a uniform time step, which depends on the applied current. The time steps are scaled such that the amount of charge passed per time step is the same for different applied currents, and are given in Table 6.3.

The tolerances for the convergence of the model equations were selected such that tighter tolerances have a minimal effect on the solution. The iterative solution for eq (6.10) is considered to have converged when the difference between successive values of $c_{deposit}$ is less than $\delta c_{deposit}$. The iterative solution for eq (6.14) is considered to have converged when the residual of eq (6.14) is less than R_c. Solving for ϕ occurs

Numerical Parameter:	Value:
Grid points (3D)	$128 \times 128 \times 96$
Domain Size (3D)	100 nm $\times$ 100 nm $\times$ 75 nm
Grid points (1D)	500
Domain Size (1D)	9000 nm
r_{init}	10 nm
H_c	-0.13 nm^{-1}, 0.03 nm^{-1}
$\delta c_{deposit}$	1e-6
R_c	4e-7 M/s
R_ϕ	9e-2 M/s
$\delta\phi_{rxn}$	1e-7 V
δ_i	0.01

Table 6.2: Numerical parameters for the simulations

i_{app} (mA/cm^2):	Δt (s):
1.5	8.33 $\times 10^{-4}$
5	2.50 $\times 10^{-4}$
10	1.25 $\times 10^{-4}$

Table 6.3: Time step for various applied current values

in two stages. First, eq (6.15) is solved using the SOR method with i_{rxn} linearized around ϕ_{int}. The iterative solution for eq (6.15) is considered to have converged when the residual of eq (6.14) is less than R_ϕ. Based on the resulting ϕ, an updated approximation of i_{rxn} is then calculated. This process continues until the difference in ϕ between successive iterations is less than $\delta\phi_{rxn}$, thus enforcing the full nonlinear expression of i_{rxn}. As described earlier, ϕ_{we} is found using a bisection method such that the current is within $\delta_i \cdot i_{app}$ of i_{app}.

In the simulations, two geometries were used for the initial Mg deposit. Most of the simulations were initialized using a hemispherical initial deposit with radius $r_{init} = 10$ nm. This initial deposit morphology is used for simulations where the basal plane of the Mg crystal structure is assumed to be parallel to the substrate, leading to

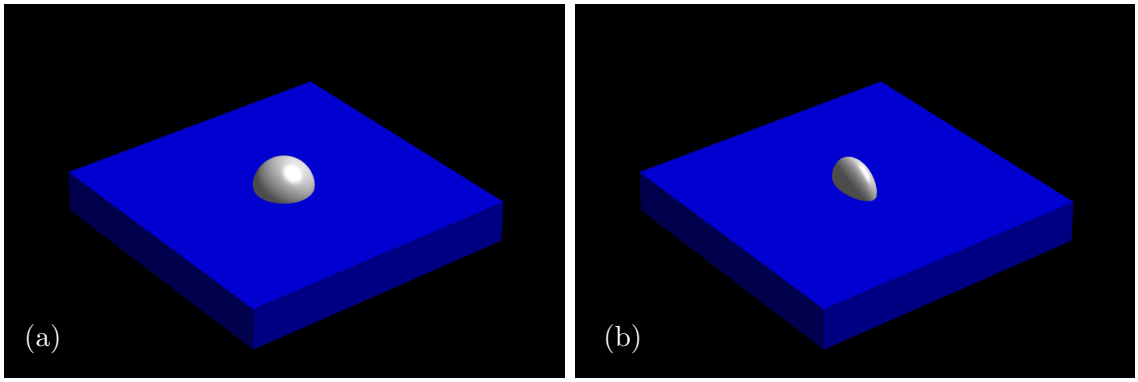

Figure 6.2: The two initial deposit morphologies for the simulations. (a) The hemispherical geometry. (b) The oblate hemispheroidal geometry.

short, broad deposits (termed in-plane deposits in Subsection 5.2). However, in two of the simulations, the basal plane is assumed to be perpendicular to the substrate, leading to tall, narrow deposits (termed out-of-plane deposits in Subsection 5.2). For one of these simulations, a 10-nm radius hemisphere was used as the initial condition. For the other simulation, an alternative initial geometry was used: an oblate hemispheroid extending 20 nm in the x direction, 10 nm in the y direction, and 10 nm in the z direction. This alternative geometry was chosen such that the maximum ratio of the thickness of the deposit parallel to the basal plane to the thickness of the deposit perpendicular to the basal plane is 2:1, just as it is for the hemispherical deposits when the basal plane is parallel to the substrate. As discussed later in Subsection 6.4.2, the oblate hemispheroid is closer than a hemisphere to the kinetic Wulff shape for the out-of-plane deposits, therefore reducing the effect of the finite size of the initial deposit on the simulated deposit morphology. The two initial deposit geometries can be seen in Fig. 6.2.

6.4 Results and Discussion

6.4.1 Determination of the Reaction Anisotropy Functions

Using the experimental images of isolated Mg deposits from Hahn and Zavadil[216] shown in 5.2, we developed expressions for the anisotropy functions, $\tilde{k}_{dep}(\theta_1, \theta_2)$ and $\tilde{k}_{dis}(\theta_1, \theta_2)$. To estimate of the aspect ratio of these deposits we measure the ratio of the thicknesses of the long and short axes of a out-of-plane plate. The out-of-plane plate directly to the left of the circled in-plate plate in Fig. 5.1b has a long-to-short axis ratio of 5:1 (70 nm to 14 nm). Assuming both types of plates are the result of rotations from the same kinetic Wulff construction, the width-to-height ratio for the in-plane plates should be twice the long-to-short axis ratio for the out-of-plane plates because the deposits do not grow into the substrate. Therefore, the expected width-to-height ratio for the in-plane plates is 10:1.

Using the aspect ratios for the hexagonal plates, we constructed anisotropy functions, $\tilde{k}_{dep}(\theta_1, \theta_2) = \tilde{k}_{dis}(\theta_1, \theta_2)$, assuming the symmetric orientation-dependence model. The components of $\tilde{k}_{dep}(\theta_1, \theta_2)$ are shown in Fig. 6.3.

The anisotropy function shown in Fig. 6.3a is given by the following piecewise function

$$\tilde{k}_{dep1}(\theta_1) = \begin{cases} 1 + \tanh\left(\frac{2}{|\tan((2\theta_1\pi)/180+\pi/2)+1\times10^{-15}|}\right) & 0 \geq \theta_1 \geq 45, 135 \geq \theta_1 \geq 225, \\ & 315 \geq \theta_1 \geq 360 \\ 0.2 + \tanh\left(\frac{0.5}{|\tan((2\theta_1\pi)/180+\pi/2)+1\times10^{-15}|}\right) & 45 > \theta_1 > 135, 225 > \theta_1 > 315 \end{cases} \tag{6.17}$$

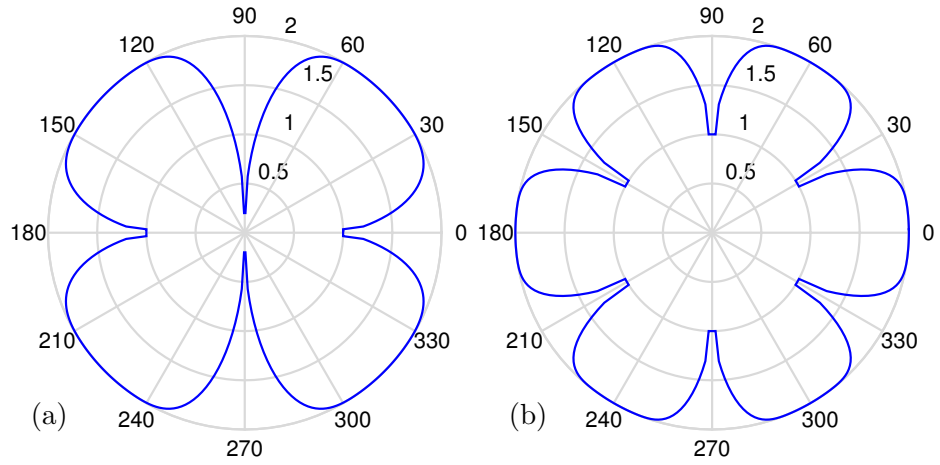

Figure 6.3: Polar plots of the components of $\tilde{k}_{dep}$ in the (a) θ_1 and (b) θ_2 directions during deposition. The cusps in these plots denote the location of the facets during growth. The product of these two functions yields the full anisotropy function.

and the anisotropy function shown in Fig. 6.3b is given by the following function:

$$\tilde{k}_{dep2}(\theta_2) = 1 + \tanh\left(\frac{2}{|\tan((3\theta_2\pi)/180) + 1 \times 10^{-15}|}\right) \tag{6.18}$$

As discussed in Section 6.3, these functions are tabulated in a lookup table. The values in the table that are within 2° of the cusps are set to the value of the cusp. The values for $\tilde{k}_{dis1}(\theta_1)$ and $\tilde{k}_{dis2}(\theta_2)$ for the reciprocal model, are calculated by taking the reciprocal of the tabulated values for $\tilde{k}_{dep1}(\theta_1)$ and $\tilde{k}_{dep2}(\theta_2)$.

6.4.2 Growth Morphologies of Individual Deposits

Figure 6.4 shows the simulated deposit morphology using these anisotropy functions with 0° and 90° rotations of the anisotropy about the x axis. The simulations were conducted at 1.5 mA/cm^2 for 5 s, as in the experimental results shown in Fig.

5.1a. We focus on the experimental morphologies at 5 s, because at 20 s most of the deposits have merged, obscuring the morphologies of the individual deposits. The simulated area of the electrode, 100 nm $\times$ 100 nm, was chosen to match the spacing between the simulated deposits to the maximum experimental spacing between deposits after 5 s so as to simulate the growth of well-separated deposits.

The in-plane hexagonal plate in Fig. 6.4a has width of 66 nm, growing 46 nm from the 20 nm diameter of the initial nucleus. This 46 nm of growth after 5 s of deposition is in agreement with the 10 to 60 nm deposit sizes observed in Fig. 5.1a.

The dependence of the morphology after 5 s of growth on the initial deposit morphology can be seen by comparing Fig. 6.4b with Fig. 6.4c. The simulations shown in Figs. 6.4b and 6.4c were initialized with the hemispherical initial geometry (1:1 ratio of the widths in the x and y directions) and the oblate hemispheroidal initial geometry (2:1 ratio of the widths in the x and y direction) described in Section 6.3, respectively. The higher initial aspect ratio of the initial condition in Fig. 6.4c results in a deposit with a higher aspect ratio after 5 s of deposition, closer to the 5:1 ratio expected from the kinetic Wulff shape. In principle, the initial shape of initial deposit should not change the predicted steady-state shape of the deposit. However, the dependence on the initial deposit shape persists due to the relatively large size of the initial deposit, as compared to the size of the deposit after 5 s of growth. As seen in Figs. 6.4b and 6.4c, the appropriate choice of the initial geometry can reduce artifacts due to the finite size of the initial deposit without having to significantly increase the spatial resolution of the simulation.

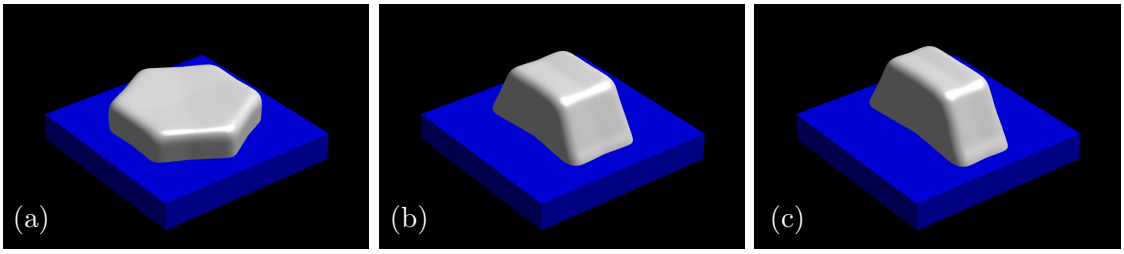

Figure 6.4: Simulated Mg deposits after 5 s of growth at 1.5 mA/cm^2. (a) An in-plane hexagonal plate deposit. (b) An out-of-plane hexagonal plate deposit where $\tilde{k}_{dep}(\theta_1, \theta_2)$ is rotated 90° about the x axis. (c) An out-of-plane hexagonal plate deposit using the oblate hemispheroidal initial geometry.

6.4.3 Effect of the Applied Current on the Deposit Morphology

For simulations like those presented in Subsection 6.4.2 that are performed at an applied current of 1.5 mA/cm^2, the electrolyte concentration at the electrode surface is effectively uniform, as can be seen in Fig. 6.5a. The electrolyte concentration is also effectively uniform at 5 mA/cm^2, as seen in Fig. 6.5b. However, as the current density increases to 10 mA/cm^2, the spatial variation in the electrolyte concentration along the electrode surface becomes noticeable, as seen in Fig. 6.5c. The concentration is particularly depleted at the sides of the deposit, where the reaction current on the faster-growing side facets has consumed more Mg^{2+} from the electrolyte than on the slower-growing top facet.

The cross-sections of the deposits grown at these three applied current densities can be seen in Fig. 6.6. As the applied current density increases and the concentration near the side facets decreases, more of the current passes through the top facet and the deposits become narrower and taller. At 10 mA/cm^2, the electrolyte concentration at the junction between the deposit and the substrate has almost reached zero, inhibiting

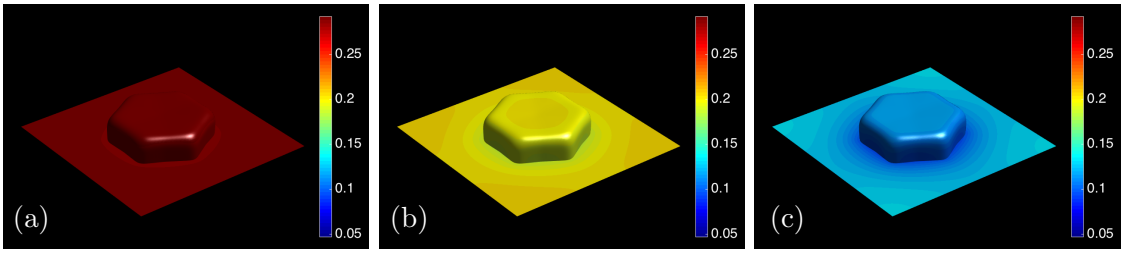

Figure 6.5: The electrolyte concentration at the electrode surface after 3 mC/cm^2 has passed at (a) 1.5, (b) 5, and (c) 10 mA/cm^2 with 100 nm spacing between deposits. The color represents the electrolyte concentration in mol/L.

further growth in this region. As a result, the sides become slanted inward.

To eliminate the possibility that the morphological change is due to the focusing of the electric field at the top of the deposit, rather than solely the concentration depletion observed above, we perform two additional simulations at 10 mA/cm^2. In the first simulation, we assume a well-stirred electrolyte where the concentration in the electrolyte is uniform at c_{ion}^{bulk}. In the second simulation, we assume a well-supported but unstirred electrolyte, where the potential drop across the bulk electrolyte is zero. The cross sections of the resulting deposits for these two simulations are shown in Fig. 6.7, along with the 10 mA/cm^2 cross section from Fig. 6.6. Under the unstirred/well-supported assumption, the deposit cross section is nearly identical to the unstirred/unsupported case. However, under the well-stirred/unsupported assumption, the deposit cross-section is more similar to the non-tapered deposits grown at a lower applied current. From these simulations, we can conclude that the morphology change is predominately due to the depletion of the electrolyte at the sides of the deposits.

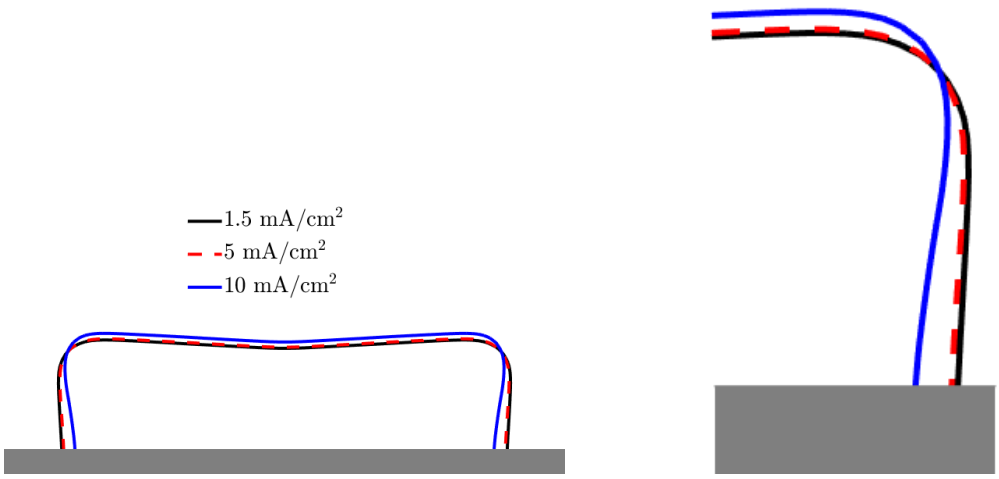

(a) (b)

Figure 6.6: (a) The cross section of the Mg deposit (going through the side facets) after 6 mC/cm^2 has passed at 1.5, 5, and 10 mA/cm^2. (b) Magnified view of the cross section of the deposit edge.

6.4.4 Effect of the Nucleus Spacing on the Electrolyte Concentration

Although the experimental image after 5 s of deposition (Fig. 5.1a) shows less than 100 nm spacing between deposits, earlier in the deposition process the spacing between neighboring deposits is larger because not all of the deposits have nucleated. To gain insight into this lower nuclei density regime, we performed three simulations similar to those in Fig. 6.5 but with 175 nm between the deposits (decreasing the density of the deposits by approximately one third). The electrolyte concentration at the electrode surface for these simulations can be seen in Fig. 6.8. With larger spacing between the nuclei, variation in the electrolyte concentration near the deposit has increased at 10 mA/cm^2 and is now visible at 1.5 and 5 mA/cm^2. At 10 mA/cm^2,

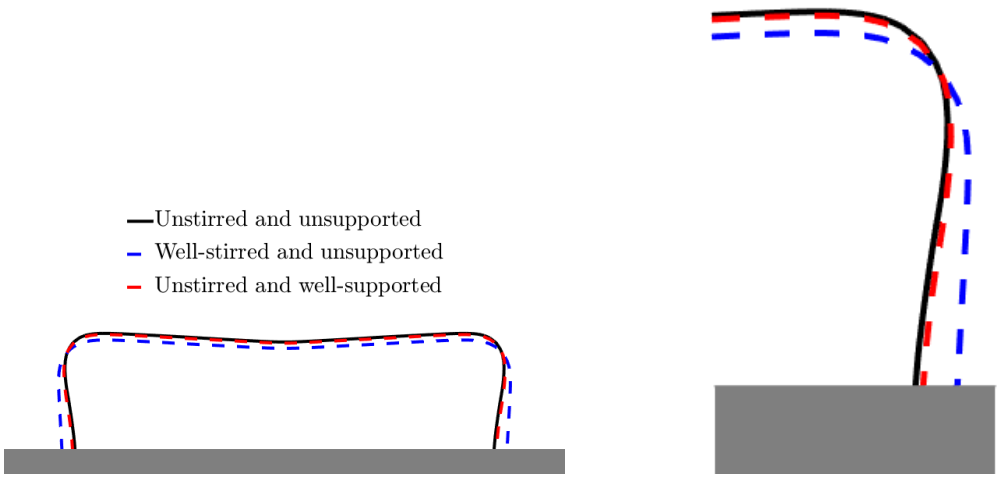

Figure 6.7: (a) The cross section of the Mg deposit for an unstirred/unsupported electrolyte, a well-stirred/unsupported electrolyte, and an unstirred/well-supported electrolyte after 6 mC/cm^2 has passed at 10 mA/cm^2. (b) Magnified view of the cross section of the deposit edge.

the electrolyte has depleted to approximately 10% of the bulk value. The minimum and maximum of the electrolyte concentration at the electrode surface for both the simulations with 100-nm and 175-nm spacing are given in Fig. 6.9. The range between the minimum and maximum concentrations increases more than two-fold as the spacing increases from 100 nm to 175 nm, with the majority of the change due to the reduced minimum concentrations for 175 nm spacing.

This finding supports Matsui's hypothesis that, during the initial stages of deposition, nucleation of Mg on the substrate is favored over growth of existing deposits due to local depletion of the electrolyte.[35] Furthermore, our simulations suggest that once the nuclei spacing is under 100 nm, the electrolyte concentration becomes

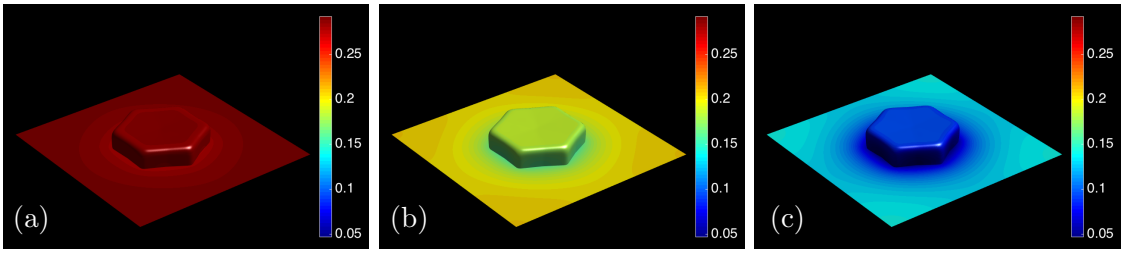

Figure 6.8: The electrolyte concentration at the electrode surface after 3 mC/cm^2 has passed at (a) 1.5, (b) 5, and (c) 10 mA/cm^2 with 175 nm spacing between deposits. The color represents the electrolyte concentration in mol/L.

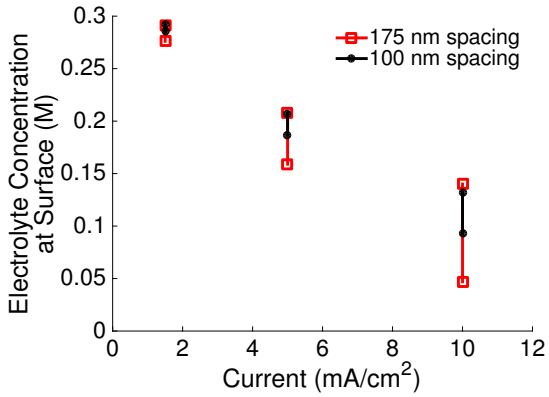

Figure 6.9: The maximum and minimum of the electrolyte concentration along the electrode surface after 3 mC/cm^2 has passed at 1.5, 5, and 10 mA/cm^2.

essentially uniform, even at high applied current densities, thus ending the preference for nucleation over growth.

6.4.5 Deposit Cycling Simulations

In addition to simulating the growth of Mg deposits, our modeling approach enables simulations of deposition-dissolution cycles. The deposit morphology during dissolution depends on the model chosen for the orientation dependence of the reaction rate. Under the symmetric model described in Section 6.2.2, the components

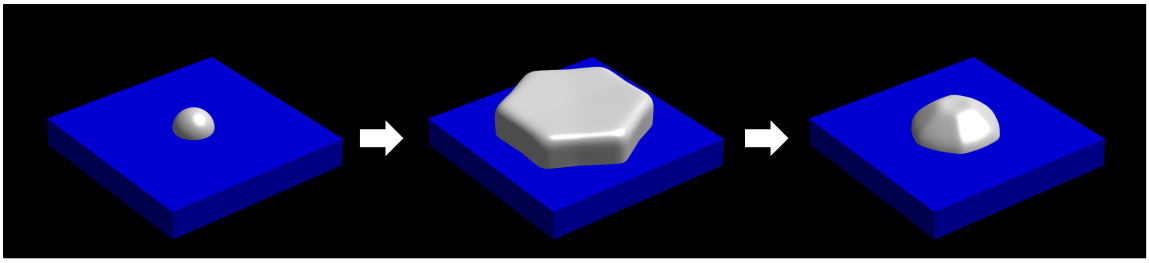

Figure 6.10: The evolution of the Mg deposit from an initial hemispherical nucleus (left), to its maximum size after 1.5 s of deposition (center), to its morphology following 1.2 s of dissolution, simulated using the symmetric model (right).

of $\tilde{k}_{dis}(\theta_1, \theta_2)$ are assumed to be equal to those for deposition, shown in Fig. 6.3. Using the standard facet selection criteria,[231] the dominant faces during dissolution are the fast-dissolving faces. Therefore, the dominant facets during dissolution are different than those during deposition and are located on the former edges of the hexagonal plate. Figure 6.10 shows the result of a simulation with 1.5 s of deposition followed by 1.2 s of dissolution, at a current density of ± 5 mA/cm^2. The deposit slowly transitions away from the hexagonal plate morphology, with clearly defined 45° faces appearing after 1.0 s of dissolution. By the end of the simulation, the deposit has evolved into a flat-topped hexagonal pyramid.

In contrast, under the reciprocal model described in Section 6.2.2, the slowest growing planes are the fastest dissolving planes, with the components of the anisotropy function for dissolution given in Fig. 6.11. Because the dominant faces during dissolution are the fast dissolving faces, the dominant faces under the reciprocal orientation-dependence model are the same during dissolution as they are during deposition. The morphology resulting from a simulation of a deposition-dissolution cycle using the reciprocal orientation-dependence model is shown in Fig. 6.12. As

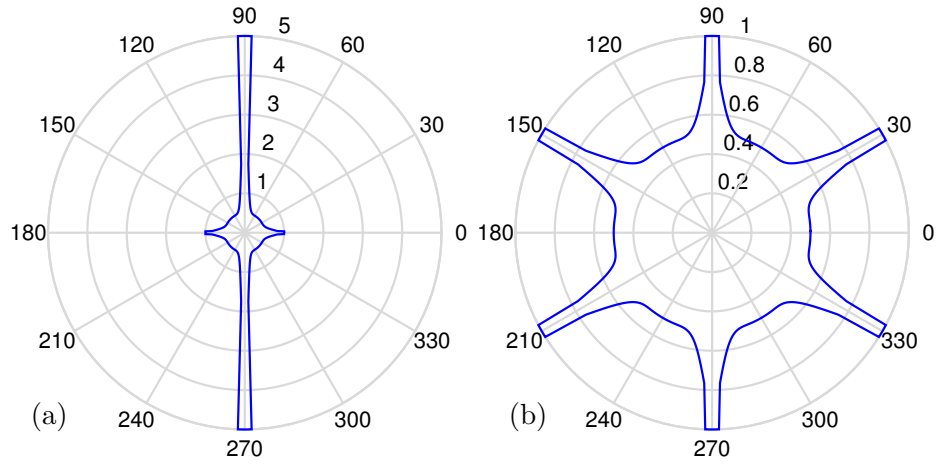

Figure 6.11: Polar plots of the components of $\tilde{k}_{dis}$ in the (a) θ_1 and (b) θ_2 directions during dissolution for the reciprocal model.

expected, the hexagonal plate morphology is maintained during dissolution. The lateral dimensions of the deposit are largely unchanged during dissolution, with nearly all of the volume change being due to a decrease in the height of the deposit. This observation is in stark contrast to what is observed during deposition, where most of the change is in the width of the deposit.

The predictions of the morphology of the hexagonal plate deposits during dissolution can be compared to the experimental morphology to determine whether the reaction is best described by the symmetric or reciprocal model. An experiment imaging the Mg deposits after partial dissolution would easily be able to discriminate between the hexagonal plate and hexagonal pyramid morphologies predicted by our simulations. The combination of this experiment and our model's continuum-scale predictions would yield insight into which of the atomistic mechanisms discussed in Section 6.2.2 are likely sources of the orientation dependence of the reaction.

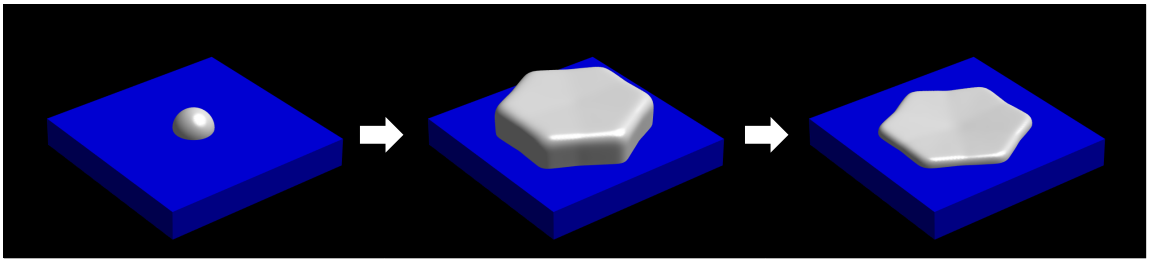

Figure 6.12: The evolution of the Mg deposit from an initial hemispherical nucleus (left), to its maximum size after 1.5 s of deposition (center), to its morphology following 1.2 s of dissolution according to the reciprocal model (right).

6.5 Conclusions

We have presented a new model of electrodeposition and electrodissolution that utilizes Butler-Volmer reaction kinetics, describes facet evolution, tracks the evolution of the electrolyte concentration, and calculates the potential distribution in the electrolyte. The model was implemented using the phase field and smoothed boundary methods, enabling practical 3D simulations of electrodeposition and dissolution with length scales of hundreds of nanometers and time scales of seconds.

Experimental imaging of Mg deposits after short periods of deposition indicates that most of the deposits are broad hexagonal plates with their broad facets either parallel or approximately perpendicular to the substrate. Simulations exhibiting both of these characteristic morphologies were presented.

The morphology of the deposits during growth was demonstrated to depend on the applied current density. At low current densities, the deposits grew in accordance with the kinetic Wulff construction. As the applied current density increases, the deposits become narrower and taller and, at 10 mA/cm^2, develop slanted side facets.

Comparisons with simulation results of well-supported and well-stirred electrolytes indicate that this morphological change is due to the depletion of the electrolyte near the side facets, rather than focusing of the electric field.

Simulations of two deposit spacings, 100 nm and 175 nm, demonstrated a strong dependence of the range of the electrolyte concentration along the electrode surface on both the applied current and the deposit spacing. These findings support Matsui's hypothesis[35] that electrolyte depletion near the deposits inhibits the growth of existing deposits during the early stages of deposition, thereby promoting the nucleation of new deposits.

Two models for the relationship between the orientation dependence of the deposition and dissolution reaction rate constants, the symmetric and reciprocal models, were presented along with likely physical mechanisms underpinning each model. The symmetric model predicts that 45° side facets form during dissolution, leading to a flat-topped hexagonal pyramid morphology. Alternatively, the reciprocal model predicts that the side facets of in-plane hexagonal plates will remain perpendicular to the substrate during dissolution and the deposit retains its hexagonal plate morphology. These simulated morphologies provide testable predictions that can be examined by future experiments.

Improving Mg anode performance is a critical step in the development and commercialization of rechargeable Mg batteries. The features of the model presented here provide the ability to link macroscopic quantities (e.g., the applied current density) to local quantities on the nanometer scale (e.g., the electrolyte concentration at a given point on the electrode surface). Because the evolution of these local quantities

determines the electrochemical behavior of the system, improved understanding of the mechanisms governing these phenomena provides new routes for optimizing the performance of Mg batteries.

CHAPTER VII

Summary, Future Work, and Contribution

7.1 Summary

In this dissertation, we investigated electrochemical nanostructure evolution utilizing continuum, diffuse interface approaches. Two test cases were examined: the growth of anodic alumina nanopores and the electrodeposition/electrodissolution of magnesium. Chapter III described a new model of anodization and provided 1D simulations of anodic alumina films. In this model a thin layer of space charge, termed the compact charge region, couples the bulk ionic transport with the reactions at the oxide/electrolyte interface. This compact charge region explains the origin of charges embedded in the oxide that have been observed experimentally. A new mechanism for bulk ionic transport was proposed, the counter-site defect mechanism, which ascribes the ionic flux to the motion of a coupled Al^{3+} ion and an O^{2-} vacancy, and is consistent with experimental observations. This model was parameterized using experimental data from the literature. The simulations provided predictions of the magnitude of the embedded charge at the oxide/electrolyte interface as a function of

the applied current and the electrolyte pH. Simulations approximating the oxide along the center of a nanopore as a 1D barrier film show that the steady-state thickness of the film is insensitive to the electrolyte pH and that pore growth rate decreases with increasing pH. Both of these results agree with experimental observations.

Chapter IV extended this model of anodization to multiple dimensions to investigate the growth of nanoporous anodic alumina. The numerical implementation of this model was presented utilizing the smoothed boundary and level set methods, which enable simulations of nanopore evolution on a regular, fixed grid. Axisymmetric pseudo-3D simulations of the growth of an individual pore were performed to determine the preferred steady-state pore geometry for a range of applied potentials and electrolyte pH values. The preferred pore geometry was determined by identification of the cell size corresponding to the fastest growing stable pore. Simulations comparing pseudo-3D and 2D calculations show that 2D calculations substantially underpredict the pore cell size and pore diameter, and thus should not be used for quantitative predictions. The simulated preferred geometries were in general agreement with experimentally observed geometries, both as a function of applied potential and electrolyte pH, although the simulations systematically overpredicted the pore diameter. Unlike previous models, which incorrectly predict a strong dependence of the pore geometry on pH, the simulated geometries were insensitive to pH, as seen experimentally, while still capturing the experimental trend that the pore growth rate decreases with increasing pH. The improved pH dependence in our model is attributed to our model's treatment of the concentration of adsorbed O^{2-} and adsorbed OH^{-} species. Like other models of anodization, our model does not

predict the experimentally observed exponential increase in the pore growth rate with increasing applied potential, which was suggested to be a result of not accounting for plastic flow.

Chapter VI described the second test case: the electrodeposition and electrodissolution of magnesium for magnesium metal battery anodes. A new model of electrodeposition and electrodissolution was presented, which included Butler-Volmer reaction kinetics, a spatially dependent electric potential distribution in the electrolyte, a time-dependent electrolyte concentration, and the formation of facets on the magnesium deposit. This model was applied to study the evolution of a magnesium deposit on a noble substrate during the initial stages of deposition. The smoothed boundary method was utilized to apply boundary conditions between the electrolyte, the magnesium deposits, and the substrate. A phase-field approach was taken to track the growth or dissolution of the magnesium deposit. As in Chapter IV, these methods permit simulations of an evolving structure on a uniform fixed grid. The orientation-dependent reaction constant for deposition was parameterized from experimental images of magnesium deposits. However, experimental data on the deposit morphology during dissolution is not available. Two models relating the orientation dependence of the dissolution reaction to that of the deposition reaction were proposed, with likely underlying mechanisms listed for each model.

3D simulations of magnesium electrodeposition yield deposit morphologies consistent with experimental observations, including examples of the two primary experimental morphologies: in-plane hexagonal plates and out-of-plane hexagonal plates. The simulations predict that the deposits become narrower and taller as the current

density increases as a result of the depletion of the electrolyte at the sides of the deposits. Simulations indicated that increased spacing between deposits leads to increased depletion of the electrolyte near the deposit, supporting a dendrite suppression hypothesis proposed by Matsui.[35] A simulation of one deposition-dissolution cycle was performed using each of the models of the orientation dependence of the reaction rate. The simulations produced substantially different morphologies after one deposition-dissolution cycle, providing predictions that can be tested against experimental morphologies to determine the source of the orientation dependence for the reaction rates.

7.2 Future Work

The work presented in this dissertation motivates and enables a variety of new investigations of electrochemical morphological evolution using continuum simulations. These new research directions are discussed below. First, direct extensions of the approaches taken to simulate anodic alumina nanopore growth and the electrodeposition/electrodissolution of magnesium are discussed. Then, the application of the approaches presented in this dissertation to other electrochemical systems is discussed.

The approach to simulating the growth of anodic alumina nanopores developed in Chapters III and IV could be applied to the simulation of multiple interacting pores, either in 2D (assuming a trench morphology) or in 3D (e.g., a hexagonal nanopore array). These simulations could investigate the interactions between pores during the competitive growth process. A preliminary 2D simulation of interacting pores, using

the approach presented in Chapter IV, is shown in Fig. 7.1. Rather than starting the simulation with the geometry of a partially developed pore, this simulation begins with a sinusoidally perturbed barrier film. As seen in Fig. 7.1, three nanopores develop from the perturbed film. The growth rate of the narrowest pore is decreasing in time, while the growth rate of the two larger pores is increasing in time. From the single pore simulations in Chapter IV, the steady-state number of pores for this domain size is two, and thus we would expect one of the pores to stop growing before the system reaches steady-state growth.

The model of anodization can be extended to include other physical considerations. The addition of plastic flow to the model, following the approach in Ref. 178, would allow an examination of the hypothesis proposed in Chapter IV, that the dependence of the growth rate on the applied potential is a result of plastic flow. The model could also be extended to consider the incorporation and transport of anion impurities from the electrolyte. This extension would allow the simulation of anodized TiO_2 nanotube formation, where the presence of F^- impurities are believed to be critical in the separation of the nanotubes.[187] Simulations considering anion impurities would also permit investigations of the significant role of the acid type in the electrolyte in controlling the anodic alumina nanopore geometry observed experimentally.[186]

The model of anodization described in this dissertation can be easily modified for material systems other than anodic alumina. Other oxides may have a different stoichiometry than alumina (e.g., titania is TiO_2), requiring minor modifications of the reaction expressions and the bulk ionic flux expression. As described in Chapter II, the material systems that form nanotubes (e.g., Ti, Fe) require F^- or Cl^-

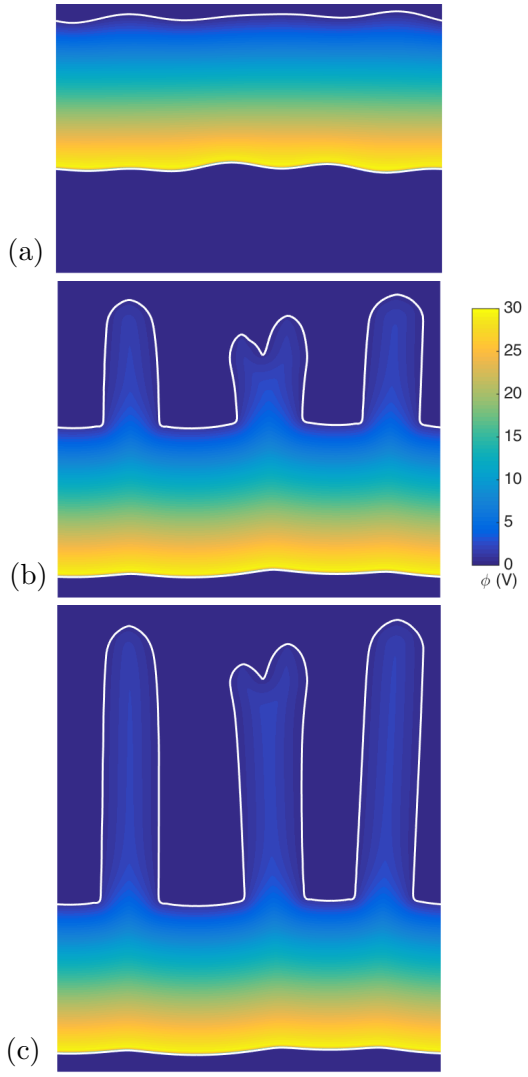

Figure 7.1: Preliminary 2D simulation of multipore evolution after (a) 0 s, (b) 40 s, and (c) 87 s of simulated time for $\phi_{app} = 30$ V and pH=1.0. The white contours mark the boundaries of the oxide ($\psi_{ox} = 0.5$) and the color represents the value of ϕ within the oxide. The computational domain is 184 nm wide.

for nanostructure formation. In these systems, the soluble species ejected into the electrolyte is a metal-fluoride or metal-chloride species (e.g., TiF_6^{2-}), rather than a

metal-hydroxide species ($AlOH^{2+}$). Therefore, the reaction model must be modified to account for the adsorption reaction for F^- or Cl^- and for the competition for anion sites in the adsorbed layer between F^-/Cl^-, the metal-fluoride/metal-chloride complex, O^{2-}, and OH^-. To model the separation of the nanotubes, the incorporation and transport of F^-/Cl^- in the bulk oxide must be considered, as discussed in the previous paragraph, along with a chemical dissolution reaction for F^--rich or Cl^--rich oxide. For the anodization of Hf and Zr, the ionic transport mechanism through the oxide must be modified to account for experimental observations that only O^{2-} is mobile in these systems.

While the Mg electrodeposition/dissolution simulation code has been parallelized with Message Passing Interface (MPI) and utilizes hundreds of computing cores, the anodization simulation code has only been parallelized using OpenMP. A typical 2D anodization simulation takes ten days on 12 computer cores. Improving the computational efficiency of the code maybe necessary for practical 3D simulations of multiple interacting pores, where large 3D computational domains must be simulated. This can be achieved in several ways. A primary source of the computational inefficiency of the simulations is the small time step size required for stable calculations of the evolution of the ion concentrations at the oxide/electrolyte interface and in the bulk oxide. At least two routes to increase the time step could be investigated. First, implicit calculations of the time evolution equations could be implemented, which typically permit the use of larger time step sizes than the explicit method used in this work. Second, certain steady-state or equilibrium assumptions could be applied to the model to remove time evolution equations from the model. For example, the

electric potential in the oxide could be calculated assuming steady-state continuity of the ionic fluxes, as in the Houser and Hebert model,[177,178] rather than Poisson's equation. However, such assumptions may violate the conservation of the number of ions in the system and should be applied with care.

Three other approaches for improving the computational efficiency of the simulations could be explored. First, a smaller computational domain could be utilized if the model equations are only solved in the region of the pore barrier. The interfacial velocity is effectively zero in the pore walls a short distance away from the base of the pore, as is the electric potential. Therefore, little accuracy would be lost if the top of the computational domain moved downward as the pore grows. Second, a computationally inexpensive 1D sharp interface calculation could provide a lookup table of the interfacial velocity and interfacial ionic fluxes at the o/e interface for the multidimensional simulation. This would eliminate the need to solve the equations for the reactions at the oxide/electrolyte interface in the multidimensional simulation. Third, an adaptive meshing approach may reduce the computational time spent on calculations outside of the oxide, while retaining high resolution near the interfaces where it is required.

The approach for simulating the electrodeposition/electrodissolution of magnesium presented in Chapter VI can be used to investigate other aspects of the evolution of magnesium deposits with any changes to the model or numerical implementation. One possibility would be to investigate the efficiency of deposition and dissolution by comparing the applied potentials needed to attain a specified current. Specifically, one could compare the efficiency for differently oriented hexagonal plates, to determine

if a certain orientation is optimal. Another possibility would be to examine the evolution of the deposit morphology after a series of cycles of deposition followed by the partial dissolution of the deposit, rather than the single cycle examined in Chapter VI. These simulations may provide insight into deleterious deposit morphologies that can develop after extended cycling.

Furthermore, the model of electrodeposition/electrodissolution can be extended to examine a wider range of phenomena and experimental conditions. First, the use of multiple phase field parameters would permit simulations where deposits with different orientations (e.g., a in-plane hexagonal plate and an out-of-plane hexagonal plate) can merge and separate during cycling. This extension would allow for simulations that reflect the complex grain structure observed experimentally. Second, including a model of deposit nucleation would enable simulations of concurrent nucleation and growth and would allow a direct test of Matsui's hypothesis relating nucleation to dendrite suppression.[35] The inclusion of a nucleation model would also permit simulations of cyclic voltammetry experiments, allowing direct comparison of the simulation to a common experimental technique. Third, a combination of first principles and kinetic Monte Carlo techniques may be able to predict the orientation-dependence of the growth rate, eliminating the need to parameterize the reaction rates from experimental images. Work has already begun on implementing these three extensions.[232,233] A fourth possible extensions is the inclusion of side reactions (chemical or electrochemical reactions that do not result in the deposition or dissolution of magnesium). These side reactions are responsible for the loss in coulombic efficiency observed experimentally. Simulations could quantify the effects of the side reactions and determine if the side

reactions are enhanced at any particular types of morphological features.

Two modifications of the numerical implementation of the electrodeposition/electrodissolution model may permit more accurate or more efficient simulations of electrodeposition/electrodissolution. First, the phase field technique used to track the interfacial motion can cause the facets to deviate slightly from the expected angles because the curvature cutoff described in Section 6.3 does not fully suppress deposition at the intersections between the facets. An improved technique for suppressing deposition in these regions may result in flatter facets with a more accurate orientation. Second, as discussed for the anodization simulations, the use of an adaptive mesh may result in increased computational efficiency.

Aside from future work directly related to the investigations in this dissertation, the modeling approaches discussed here can be applied to a variety of other electrochemical systems that exhibit morphology change, including the electrodeposition of materials other than magnesium, and corrosion. Two important applications of electrodeposition, where the nanostructure is very important, are lithium metal anodes and copper interconnects in integrated circuits. First, as discussed in Subsection 5.1, the formation of dendrites during the electrodeposition of lithium has prevented the adoption of rechargeable batteries with lithium metal anodes.[205] The model and numerical implementation of electrodeposition presented in Chapter VI is already being applied to study lithium dendrite formation, where it is used to study the critical length scale at which the electric field in the electrolyte focuses to cause the nonuniform deposition that leads to dendrite formation.[232] Similar investigations could be performed for other materials relevant to metallic battery anodes, such as

zinc and sodium anodes. Second, the morphology of electrodeposited copper in interconnects must be carefully controlled to ensure that no seams or voids form.[32,234] The concentration of accelerator molecules adsorbed at the electrode/electrolyte interface plays a large role in determining the eventual copper morphology.[32] A description of the adsorbed accelerator concentration, in the manner described in Chapter IV for anodization, could be incorporated into the electrodeposition model presented in Chapter VI in order to model this system. Finally, corrosion shares features with both anodic film growth and electrodeposition.[235] Like anodization, an oxide film can be formed, but like electrodeposition, the electric fields involved are relatively low and the concentration of species in the bulk electrolyte should be considered. A hybrid approach, combination aspects of both the anodic film growth and electrodeposition models may be appropriate for modeling corrosion.

7.3 Contributions

This dissertation focuses on the modeling and simulation of nanostructural evolution in electrochemical systems, specifically examining the growth of anodic oxide films and the electrodeposition/electrodissolution of magnesium. The work presented in this dissertation provides unique contributions to the understanding of these systems by means of improved models, numerical implementations of these models, and physical insights gained through simulations.

For anodic oxide growth, we combined previously proposed reaction-centric and bulk-transport-centric modeling approaches through the consideration of a compact charge region at the oxide/electrolyte interface. We showed that this region ex-

plains the presence of embedded charge in the oxide/electrolyte interface following anodization, and provided experimentally verifiable predictions of the embedded charge with respect to the applied potential and the electrolyte pH. Furthermore, through multidimensional simulations of pore growth, we demonstrated that the consideration of adsorbed species, which mediate the interaction between the electrolyte pH and interfacial motion, is crucial to capture the experimentally observed pH dependence. In both of these cases, the inclusion of physical mechanisms neglected in prior models was shown to be necessary to explain the origin of experimentally observed phenomena.

For the electrodeposition and electrodissolution of magnesium, we presented a new modeling approach that describes the morphological evolution of faceted deposits as well as phenomena in the electrolyte. We showed that this approach allows us to link macroscopic quantities, such as the applied current density, to local quantities on the nanometer scale, such as the electrolyte concentration along the electrode surface. This link permits the investigation of nanoscale phenomena that are difficult to examine experimentally. We also conducted simulations to obtain the morphology of a deposit after one deposition-dissolution cycle for two types of orientation dependence of the dissolution reaction. These simulations provide testable predictions to provide insight into the mechanisms controlling the deposition/dissolution reactions.

The models and simulation codes developed through this work provide a platform for future investigations of electrochemical systems with evolving morphologies. This work is a step toward the development of truly quantitatively predictive simulations that can be applied to understand, control, and optimize the behavior of

electrochemical systems.

BIBLIOGRAPHY

BIBLIOGRAPHY

[1] Corrosion Cost and Preventative Strategies in the United States. 2002; McLean, VA: U.S. Deparment of Transportation, Federal Highway Administration.

[2] Newman, J.; Thomas-Alyea, K. E. *Electrochemical Systems*, 3rd ed.; John Wiley and Sons: Hoboken, NJ, 2004.

[3] Stetter, J.; Li, J. *Chem. Rev.* **2008**, *108*, 352–366.

[4] Ellis, B.; Makahnouk, W.; Makimura, K., Y. Toghill; Nazar, L. *Nat. Mater.* **2007**, *6*, 749–753.

[5] Paulose, M.; Shankar, K.; Yoriya, S.; Prakasam, H.; Varghese, O.; Mor, G.; LaTempa, T.; Fitzgerald, A.; Grimes, C. *J. Phys. Chem. B* **2006**, *110*, 16179–16184.

[6] Wilson, J.; Kobsiriphat, W.; Mendoza, R.; Chen, H.-Y.; Hiller, J.; Miller, D.; Thornton, K.; Voorhees, P.; Adler, S.; Barnett, S. *Nat. Mater.* **2006**, *5*, 541–544.

[7] Fransson, L.; Eriksson, T.; Edstrom, K.; Gustafsson, T.; Thomas, J. *J. Power Sources* **2001**, *101*, 1–9.

[8] Smith, M.; Garcia, R.; Horn, Q. *J. Electrochem. Soc.* **2009**, *156*, A896–A904.

[9] Orvananos, B.; Ferguson, T.; Yu, H.; Bazant, M.; Thornton, K. *J. Electrochem. Soc.* **2014**, *161*, A535.

[10] Modeling Across Scales: A Roadmapping Study for Connecting Materials Models and Simulations Across Length and Time Scales. 2015; Warrendale, PA: The Minerals, Metals, and Materials Society.

[11] Curtarolo, S.; Hart, G.; Nardelli, M.; Mingo, N.; Sanvito, S.; Levy, O. *Nat. Mater.* **2013**, *12*, 191–201.

[12] Cheng, L.; Assary, R.; Qu, X.; Jain, A.; Ong, S.; Rajput, N.; Persson, K.; Curtiss, L. *J. Phys. Chem. Lett.* **2015**, *6*, 283–291.

[13] Davis, S.; Gutierrez, G. *Journal of Physics - Condensed Matter* **2011**, *23*, 495401.

[14] Ouyang, C.; Zhong, Z.; Lei, M. *Electrochem. Commun.* **2007**, *9*, 1107–1112.

[15] Van der Ven, A.; Bhattacharya, J.; Belak, A. *Acc. Chem. Res.* **2012**, *46*, 1216–1225.

[16] Leung, K.; Budzien, J. *Phys. Chem. Chem. Phys.* **2010**, *12*, 6583–6586.

[17] Leveque, R. J.; Li, Z. *SIAM J. Numer. Anal.* **1994**, *31*, 1019–1044.

[18] Peskin, C. *J. Comp. Phys.* **1972**, *10*, 252–271.

[19] Li, Z.; Ito, K. *The Immersed Interface Method*; Society for Industrial and Applied Mathematics: Philadelphia, PA, 2006.

[20] Bueno-Orovio, A.; Perez-Garcia, V. *Numer. Methods Partial Diff. Eqns.* **2005**, *22*, 435–448.

[21] Yu, H.; Chen, H.; Thornton, K. *Modelling Simul. Mater. Sci. and Eng.* **2012**,

[22] Provatas, N.; Elder, K. *Phase-Field Methods in Materials Science and Engineering*; John Wiley and Sons: Hoboken, NJ, 2010.

[23] Sethian, J. *Level Set Methods and Fast Marching Methods*, 2nd ed.; Cambridge University Press: Cambridge, UK, 2008.

[24] Orvananos, B.; Malik, R.; Yu, H.; Abdellahi, A.; Grey, C. P.; Ceder, G.; Thornton, K. *Electrochim. Acta* **2014**, *137*, 245–257.

[25] Ely, D. R.; Jana, A.; García, R. E. *Journal of Power Sources* **2014**,

[26] Guyer, J.; Boettinger, W.; Warren, J.; McFadden, G. *Physical Review E* **2004**, *69*.

[27] Guyer, J.; Boettinger, W.; Warren, J.; McFadden, G. *Physical Review E* **2004**, *69*.

[28] Shibuta, Y.; Okajima, Y.; Suzuki, T. *Sci. Tech. Adv. Mater.* **2007**, *8*, 511–518.

[29] Orvananos, B.; Yu, H.-C.; Abdellahi, A.; Malik, R.; Grey, C.; Ceder, G.; Thornton, K. *J. Electrochem. Soc.* **2015**, *162*, A965–A973.

[30] Cogswell, D.; Bazant, M. *ACS Nano* **2012**, *6*, 2215–2225.

[31] Chen, L.; Fan, F.; Hong, L.; Chen, J.; Ji, Y.; Zhang, S.; Zhu, T.; Chen, L. *J. Electrochem. Soc.* **2014**, *161*, 3374–3376.

[32] Wheeler, D.; Josell, D.; Moffat, T. P. *Journal of The Electrochemical Society* **2003**, *150*.

[33] Kenney, J.; Hwang, G. *Appl. Phys. Lett.* **2004**, *84*, 3374–3376.

[34] Yoo, H. D.; Shterenberg, I.; Gofer, Y.; Gershinsky, G.; Pour, N.; Aurbach, D. *Energy & Environmental Science* **2013**, *6*.

[35] Matsui, M. *Journal of Power Sources* **2011**, *196*.

[36] Diggle, J.; Downie, T.; Goulding, C. *Chem. Rev.* **1969**, *69*, 365–405.

[37] Young, L. *Anodic Oxide Films*; Academic Press: London, 1961.

[38] Masuda, H.; Fukuda, K. *Science* **1995**, *268*, 1466–1468.

[39] Rani, S.; Roy, S.; Paulose, M.; Varghese, O.; Mor, G.; Kim, S.; Yoriya, S.; Latempa, T. J.; Grimes, C. *Phys. Chem. Chem. Phys.* **2010**, *12*, 2780–2800.

[40] Yasakau, K.; Salak, A.; Zheludkevich, M.; Ferreira, M. *J. Phys. Chem. C* **2010**, *114*, 8474–8484.

[41] Masuda, H.; Hasegwa, F.; Ono, S. *J. Electrochem. Soc.* **1997**, *144*, L127–L130.

[42] Lee, K.; Yang, Y.; Yang, M.; Schmuki, P. *Chemistry* **2012**, *18*, 9521–9524.

[43] Lee, K.; Schmuki, P. *Electrochem. Commun.* **2011**, *13*, 542–545.

[44] Tsuchiya, H.; Macak, J.; Sieber, I.; Taveira, L.; Ghicov, A.; Sirotna, K.; Schmuki, P. *Electrochem. Commun.* **2005**, *7*, 295–298.

[45] Shin, H.; Dong, J.; Liu, M. *Adv. Mater.* **2004**, *16*, 237–240.

[46] Berger, S.; Hahn, R.; Roy, P.; P., S. *Phys. Status Solidi B* **2010**, *247*, 2424–2435.

[47] Keller, F.; Hunter, M.; Robinson, D. *J. Electrochem. Soc.* **1953**, *100*, 411–419.

[48] O'Sullivan, J.; Wood, G. *Proc. R. Soc. A* **1970**, *317*, 511–543.

[49] Masuda, H.; Satoh, M. *Jpn. J. Appl. Phys., Part 2* **1996**, *35*, L126–L129.

[50] Masuda, H.; Yamada, H.; Satoh, M.; Asoh, H.; Nakao, M.; Tamamura, T. *Appl. Phys. Lett.* **1997**, *71*, 2770–2772.

[51] Cheng, C.; Ngan, A. *J. Phys. Chem. C* **2103**, *117*, 12183–12190.

[52] Friedman, A.; Brittain, D.; Menon, L. *J. Chem. Phys.* **2007**, *127*, 154717.

[53] Nielsch, K.; Choi, J.; Schwirn, K.; Wehrspohn, R.; Gosele, U. *Nano. Lett.* **2002**, *2*, 677–680.

[54] Chen, W.; Wu, J.; Xia, X. *ACS Nano* **2008**, *2*, 959–965.

[55] Ebihara, K.; Takahashi, H.; Nagayama, M. *J. Met. Finish. Soc. Jpn.* **1983**, *34*, 548–553.

[56] Li, F.; Zhang, L.; Metzger, R. *Chem. Mater.* **1998**, *10*, 2470–2480.

[57] Nagayama, M.; Tamura, K.; Takahashi, H. *Corros. Sci.* **1970**, *10*, 617–627.

[58] Macak, J.; Tsuchiya, H.; Ghicov, A.; Yasua, R., K. an Hahn; Bauer, S.; Schmuki, P. *Curr. Opin. Solid State Mater. Sci.* **2007**, *11*, 3–18.

[59] Ghicov, A.; Schmuki, P. *Chem. Commun.* **2009**, 2791–2808.

[60] Zwilling, V.; Darque-Ceretti, E.; Boutry-Forveille, A.; David, D.; Perrin, M.; Aucouturier, M. *Suf. Interface Anal.* **1999**, *27*, 629–637.

[61] Ismail, Z., S. Ahmad; Berenov, A.; Lockman, Z. *Corros. Sci.* **2011**, *53*, 1156–1164.

[62] Tsuchiya, H.; Schmuki, P. *Electrochem. Commun.* **2005**, *7*, 49–52.

[63] Rangaraju, R.; Panday, A.; Raja, K.; Misra, M. *J. Phys. D.: Appl. Phys.* **2009**, *42*, 135303.

[64] Richter, C.; Wu, Z.; Panaitescu, E.; Willey, R.; Menon, L. *Adv. Mater.* **2007**, *19*, 946–948.

[65] Mohapatra, S.; Misra, M.; Mahajan, V.; Raja, K. *J. Phys. Chem. C* **2007**, *111*, 8677–8685.

[66] Yahia, L., S.A.A. amd Hamadou; Kadri, A.; Benbrahim, N.; Sutter, E. *J. Electrochem. Soc. 159*, K85–K92.

[67] Macak, J.; Hildebrand, H.; Marten-Jahns, U.; Schmuki, P. *J. Electroanal. Chem. Interfacial Electrochem.* **2008**, *621*, 254–266.

[68] Paulose, M.; Prakasam, H.; Varghese, O.; Peng, L.; Popat, K.; Mor, G.; Desai, T.; Grimes, C. *J. Phys. Chem. C* **2007**, *111*, 14992–14997.

[69] Meng, G.; Jung, Y.; Cao, A.; Vajtai, R.; Ajayan, P. *Proc. Natl. Acad. Sci. U.S.A.* **2005**, *102*, 7074–7078.

[70] Albu, S.; D., K.; Schmuki, P. *Angew. Chem. Int. Ed. Engl.* **2008**, *47*, 1916–1919.

[71] Oh, J.; Thompson, C. *J. Electrochem. Soc.* **2011**, *158*, C71.

[72] Lee, W.; Gosele, U.; Nielsch, K. *Nat. Mater.* **2006**, *5*, 741–747.

[73] Losic, D.; Losic, D. *Langmuir* **2009**, *25*, 5426–5431.

[74] Valand, T.; Heusler, K. *J. Electroanal. Chem.* **1983**, *149*, 71–82.

[75] Thompson, G. *Thin Solid Films* **1997**, *297*, 192–201.

[76] Davies, J.; Domeij, B.; Pringle, J.; Brown, F. *J. Electrochem. Soc.* **1965**, *112*, 675–680.

[77] Habazaki, H.; Shimizu, K.; Nagata, S.; Skeldon, P.; Thompson, G.; Wood, G. *Corros. Sci.* **2002**, *46*, 1047–1055.

[78] Lu, Q.; Skeldon, P.; Thompson, G.; Masheder, D.; Habazaki, H.; Shimizu, K. *Corros. Sci.* **2004**, *46*, 2817–2824.

[79] Khalil, N.; Leach, J. *Electrochim. Acta* **1986**, *31*, 1379–1285.

[80] Amsel, G.; Samuel, D. *J. Phys. Chem. Solids* **1962**, *23*, 1707–1718.

[81] Pringle, J. *Journal of the Electrochemical Society* **1973**, *120*, 398–407.

[82] Perriere, J.; Siejka, J.; Rigo, S. *Corros. Sci.* **1980**, *20*, 91–102.

[83] Verwey, E. *Physica* **1935**, *2*, 1059–1063.

[84] Cabrera, N.; Mott, N. F. *Reports on Progress in Physics* **1949**, *12*, 163–184.

[85] Dewald, J. *J. Electrochem. Soc.* **1955**, *102*, 1–6.

[86] Bernard, W.; Cook, J. *Journal of the Electrochemical Society* **1959**, *106*, 643–646.

[87] Harkness, A.; Young, L. *Canadian Journal of Chemistry* **1966**, *44*, 2409–2413.

[88] DeWitt, S.; Thornton, K. *Langmuir* **2014**, *30*, 5314–5325.

[89] Wang, M.; Hebert, K. *Journal of the Electrochemical Society* **1999**, *146*, 3741–3749.

[90] Fromhold, A. *J. Electrochem. Soc.* **1980**, *127*, 411–425.

[91] Sato, N.; Cohen, M. *Journal of The Electrochemical Society* **1964**, *111*, 512–519.

[92] Vermilyea, D. *J. Electrochem. Soc.* **1963**, *110*, 345–346.

[93] Capraz, O.; Hebert, K.; Shrotriya, P. *J. Electrochem. Soc.* **2013**, *160*, D501–D506.

[94] Overmeere, Q.; Blaffart, F.; Proost, J. *Electrochem. Commun.* **2010**, *12*, 1174–1176.

[95] Capraz, O.; Shrotriya, P.; Skeldon, P.; Thompson, G.; Hebert, K. *Electrochim. Acta* **2015**, *159*, 16–22.

[96] Garcia-Vergara, S.; Skeldon, P.; Thompson, G.; Habazaki, H. *Electrochimica Acta* **2006**, *52*, 681–687.

[97] Houser, J. E.; Hebert, K. R. *J. Electrochem. Soc.* **2006**, *153*, 566–573.

[98] Fromhold, A.; Cook, E. *Phys. Rev.* **1968**, *175*, 877–897.

[99] Hickmott, T. *J. Appl. Phys.* **2007**, *102*, 93706.

[100] Lambert, J.; Guthmann, C.; Ortega, C.; M, S. *J. Appl. Phys.* **2002**, *91*, 9161–9169.

[101] Hoar, T.; Mott, N. *J. Phys. Chem. Solids* **1959**, *9*, 97–99.

[102] Parkhutik, V.; Shershulsky, V. *J. Appl. Phys. D* **1992**, *25*, 1258–1263.

[103] Thamida, S.; Chang, H. *Chaos* **2002**, *12*, 240–251.

[104] Cheng, C.; Ngan, A. *Electrochim. Acta* **2011**, *56*.

[105] Yasuda, K.; Macak, J.; Berger, S.; Ghicov, A.; Schmuki, P. *J. Electrochem. Soc.* **2007**, *154*, C472–C478.

[106] Singh, G. K.; Golovin, A. A.; Aranson, I. S.; Vinokur, V. M. *Europhysics Letters* **2005**, *70*, 836–842.

[107] Singh, G.; Golovin, A.; Aranson, I. *Phys. Rev. B* **2006**, *73*, 205422.

[108] Jessensky, O.; Muller, F.; Gosele, U. *Appl. Phys. Lett.* **1998**, *72*, 1173–1175.

[109] Sulka, G.; Stroobants, S.; Moshchalkov, V.; Borghs, G.; Celis, J. *J. Electrochem. Soc.* **2004**, *151*, B260–B264.

[110] Garcia-Vergara, S.; Skeldon, P.; Thompson, G.; Habazaki, H. *Electrochim. Acta* **2006**, *52*, 681–687.

[111] Stanton, G.; Golovin, A. *Math. Modell. Nat. Phenom.* **2008**, *3*, 73–91.

[112] Gong, D.; Grimes, C.; Varghese, O.; Hu, W.; Singh, R.; Chen, Z.; Dickey, E. *J. Mater. Res.* **2011**, *16*, 3331–3334.

[113] Houser, J.; Hebert, K. *Nat. Mater.* **2009**, *8*, 415–420.

[114] Hebert, K. *Electrochemical Engineering Across Scales*; John Wiley & Sons: Hoboken, NK, 2015; Vol. 15; Chapter 4, pp 107–144.

[115] Mathew, S.; Yella, A.; Gao, P.; Humphry-Baker, R.; Curchod, B.; Ashari-Astani, N.; Tavernelli, I.; Rothlisberger, U.; Nazeeruddin, M.; Gratzel, M. *Nat. Chem.* **2014**, *6*, 242–247.

[116] Nelson, J. *Phys. Rev. B* **1999**, *59*, 15374–15380.

[117] Mor, G.; Shankar, K.; Paulose, M.; Varghese, O.; Grimes, C. *Nano Lett.* **2006**, *6*, 215–218.

[118] Mohammadpour, F.; Moradi, M.; Lee, K.; Cha, G.; So, S.; Kahnt, A.; Guldi, D. M.; Altomare, M.; Schmuki, P. *Chem. Commun.* **2015**, *51*, 1631–1634.

[119] Zhu, K.; Neale, N.; Miedaner, A.; Frank, A. *Nano Lett.* **2007**, *7*, 69–74.

[120] Richter, C.; Schmuttenmaer, C. *Nat. Nanotechnol.* **2010**, *5*, 769–772.

[121] Kang, T.; Smith, B., A.P. Taylor; Durstock, M. *Nano Lett.* **2009**, *9*, 601–606.

[122] Jacobsson, T.; Fjallstrom, V.; Edoff, M.; Edvinsson, T. *Energy. Environ. Sci.* **2014**, *7*, 2056–2070.

[123] Murphy, A.; Barnes, P.; Randeniya, L.; Plumb, I.; Grey, I.; Horne, M.; Glasscock, J. *Int. J. Hydrogen Energy* **2006**, *31*, 1999–2017.

[124] Mao, A.; Park, N.; Han, G.; Park, J. *Nanotechnology* **2011**, *22*, 175703.

[125] Prakasam, H. E.; Varghese, O. K.; Paulose, M.; Mor, G. K.; Grimes, C. A. *Nanotechnology* **2006**, *17*.

[126] Mushove, T.; Breault, T.; Thompson, L. *Ind. Eng. Chem. Res.* **2015**, *54*, 4285–4292.

[127] Mor, G.; Kim, S.; Paulose, M.; Varghese, O.; Shankar, K.; Basham, J.; Grimes, C. *Nano Lett.* **2009**, *9*, 4250–4257.

[128] Mor, G.; Shankar, K.; Paulose, M.; Varghese, O. K.; Grimes, C. A. *Appl. Phys. Lett.* **2007**, *91*, 152111.

[129] Chen, D.; Zhao, W.; Russel, T. *ACS Nano* **2012**, *6*, 1479–1485.

[130] Ortiz, G. F.; Hanzu, I.; Djenizian, T.; Lavela, P.; Tirado, J. L.; Knauth, P. *Chemistry of Materials* **2009**, *21*, 63–67.

[131] Wang, Y.; Liu, B.; Li, Q.; Cartmell, S.; Ferrara, S.; Deng, Z. D.; Xiao, J. *J. Power Sources* **2015**, *286*, 330–345.

[132] Wagemaker, M.; Kearly, G.; Van Well, A.; Mutka, H.; Mulder, F. *J. Am. Chem. Soc.* **2003**, *125*, 840–848.

[133] Liu, D.; Xiao, P.; Zhang, Y.; Garcia, B.; Zhang, Q.; Guo, Q.; Champion, R.; Cao, G. *J. Phys. Chem. C* **2008**, *112*, 11175–11180.

[134] Xiong, H.; Yildirim, H.; Shevchenko, E.; Prakapenka, V.; Koo, B.; Slater, M.; Balasubramanian, M.; Sankaranarayanan, S.; Greeley, J.; Tepavcevic, S.; Dimitrijevic, N.; Podsiadlo, P.; Johnson, C.; Rajh, T. *J. Phys. Chem. C* **2012**, *116*, 3181–3187.

[135] Zhu, Q.; Hu, H.; Li, G.; Zhu, C.; Yu, Y. *Electrochim. Acta* **2015**, *156*, 252–260.

[136] Lamberti, A.; Garino, N.; Sacco, A.; Bianco, S.; Manfredi, D.; Gerbaldi, C. *Electrochim. Acta* **2013**, *102*, 233–239.

[137] Wei, Z.; Liu, Z.; Jiang, R.; Bian, C.; Huang, T.; Yu, A. *J. Solid State Electrochem.* **2009**, *14*, 1045–1050.

[138] Madian, M.; Giebeler, L.; Klose, M.; Jaumann, T.; Uhlemann, M.; Gebert, A.; Oswald, S.; Ismail, N.; Eychmuller, A.; Eckert, J. *ACS Sustainable Chem. Eng.* **2015**, *3*, 909–919.

[139] Ortiz, G.; Hanzu, I.; Lavela, P.; Tirado, J. L.; Knauth, P.; Djenizian, T. *J. Mater. Chem.* **2010**, *20*, 4041–4046.

[140] Wang, W.; Tian, M.; Abdulagatov, A.; George, S.; Lee, Y.; Yang, R. *Nano Lett.* **2012**, *12*, 655–660.

[141] Cheah, S. K.; Perre, E.; Rooth, M.; Fondell, M.; Harsta, A.; Nyholm, L.; Boman, M.; Gustafsson, T.; Lu, J.; Simon, P.; Edstrom, K. *Nano Lett.* **2009**, *9*, 3230–3233.

[142] Xie, K.; Lu, Z.; Huang, H.; Lu, W.; Lai, Y.; Li, J.; Zhou, L.; Liu, Y. *J. Mater. Chem.* **2012**, *22*, 5560–5567.

[143] Taberna, P.; Mitra, S.; Poizot, P.; Simon, P.; Tarascon, J. *Nat. Mater.* **2006**, *5*, 567–573.

[144] Yang, Y.; Fan, X.; Casillas, G.; Peng, Z.; Ruan, G.; Wang, G.; Yacaman, M.; Tour, J. *ACS Nano* **2014**, *8*, 3939–3946.

[145] Cheng, H.; Lu, Z.; Ma, R.; Dong, Y.; Wang, H.; Xi, L.; Zheng, L.; Tsang, C.; Li, H.; Chung, C.; Zapien, J.; Li, Y. *J. Mater. Chem* **2012**, *22*, 22692–22698.

[146] Kim, J.; Zhu, K.; Yan, Y.; Perkins, C.; Frank, A. *Nano Lett.* **2010**, *10*, 4099–4104.

[147] Hu, C.; Chang, K.; Lin, M.; Wu, Y. *Nano Lett.* **2006**, *6*, 2690–2695.

[148] Zhao, G.-Y.; Li, H.-L. *Microporous Mesoporous Mater.* **2008**, *110*, 590–594.

[149] Zhang, L.; Zhao, X. *Chem. Soc. Rev.* **2009**, *38*, 2520–2531.

[150] Lu, X.; Wang, G.; Zhai, T.; Yu, M.; Gan, J.; Tong, Y.; Li, Y. *Nano Lett.* **2012**, *12*, 1690–1696.

[151] Xie, K.; Li, J.; Lai, Y.; Zhang, Z.; Liu, Y.; Zhang, G.; Huang, H. *Nanoscale* **2011**, *3*, 2202–2207.

[152] Bo, G.; Xiaogang, Z.; Changzhou, Y.; Juan, L.; Long, Y. *Electrochim. Acta* **2006**, *52*, 1028–1032.

[153] Xu, J.; Gao, L.; Cao, J.; Wang, W.; Chen, Z. *Electrochim. Acta* **2010**, *56*, 732–736.

[154] Hu, X.; Jiang, J.; Zhang, F.; Ling, Z. *Solid State Ionics 268*, 316–320.

[155] Xing, H.; Long, J. J.; Hui, F. Z.; Zhiyuan, L. *J. Electrochem. Soc.* **2013**, *160*, A1425–A1429.

[156] Xie, Y.; Huang, C.; Zhou, L.; Liu, Y.; Huang, H. *Compos. Sci. Technol.* **2009**, *69*, 2108–2114.

[157] Xia, H.; Feng, J.; Wang, H.; Lai, M.; Lu, L. *J. Power Sources* **2010**, *195*, 4410–4413.

[158] Yasakau, K. A.; Salak, A. N.; Zheludkevich, M. L.; Ferreira, M. G. S. *The Journal of Physical Chemistry C* **2010**, *114*, 8474–8484.

[159] Lambert, J.; Guthmann, C.; Ortega, C.; M, S. *Journal of Applied Physics* **2002**, *91*, 9161–9169.

[160] Battaglia, V.; Newman, J. *Journal of the Electrochemical Society* **1995**, *142*, 1423–1430.

[161] Parkhutik, V.; Shershulsky, V. *Journal of Applied Physics D: Applied Physics* **1992**, *25*, 1258–1263.

[162] Bazant, M.; Chu, K.; Bayly, B. *SIAM Journal on Applied Mathematics* **2005**, *65*, 1463–1484.

[163] Bard, A. J.; Faulkner, L. R. *Electrochemical Methods*, 2nd ed.; John Wiley and Sons: Hoboken, NJ, 2001.

[164] Guentherschuleze, A.; Betz, H. *Zeitschrift fur Physik* **1934**, *92*, 367–374.

[165] Pringle, J. *Journal of the Electrochemical Society* **1973**, *120*, 1391–1400.

[166] Chao, C.; Lin, L.; Macdonald, D. *Journal of the Electrochemical Society* **1981**, *128*, 1187–1194.

[167] Fromhold, A. In *Oxides and Oxide Films*; Diggle, J., Ashtok, K., Eds.; Marcel Dekker: New York, NY, 1976; Vol. 3.

[168] Davies, J.; Domeij, B.; Pringle, J.; Brown, F. *Journal of the Electrochemical Society* **1965**, *112*, 675–680.

[169] Brown, F.; Mackintosh, W. D. *Journal of The Electrochemical Society* **1973**, *120*, 1096–1102.

[170] Thompson, G. E.; Xu, Y.; Skeldon, P.; Shimizu, K.; Han, S. H.; Wood, G. C. *Philosophical Magazine Part B* **1987**, *55*, 651–667.

[171] Xu, Y.; Thompson, G.; Wood, G.; Bethune, B. *Corrosion Science* **1987**, *27*, 95–102.

[172] Shimizu, K.; Brown, G.; Habazaki, H.; Kobayashi, K.; Skeldon, P.; Thompson, G.; Wood, G. *Electrochimica Acta* **1999**, *44*, 2297–2306.

[173] Fromhold, A. *Journal of The Electrochemical Society* **1980**, *127*, 411–425.

[174] Valand, T.; Heusler, K. *Journal of Electroanalytical Chemistry* **1983**, *149*, 71–82.

[175] Siejka, J.; Ortega, C. *J. Electrochem. Soc.* **1977**, *124*, 883–891.

[176] Bockris, J. O.; White, R. E.; Conway, B. E. *Modern Aspects of Electrochemistry*; Plenum: New York, NY, 1989; Vol. 20; Chapter 6, pp 401–503.

[177] Houser, J. E.; Hebert, K. R. *Journal of the Electrochemical Society* **2006**, *153*, 566–573.

[178] Houser, J.; Hebert, K. *Nature Materials* **2009**, *8*, 415–420.

[179] Hebert, K. R.; Houser, J. E. *Journal of The Electrochemical Society* **2009**, *156*, 275–281.

[180] Singh, G.; Golovin, A.; Aranson, I. *Physical Review B* **2006**, *73*, 205422.

[181] Frers, S.; Stefenel, M.; Mayer, C.; Chierchie, T. *Journal of Applied Electrochemistry* **1990**, *20*, 996–999.

[182] Oka, Y.; Takahashi, T.; Okada, K.; Iwai, S. *Journal of Non-Crystalline Solids* **1979**, *30*, 349–357.

[183] Tewari, P.; McLean, A. *Journal of Colloid and Interface Science* **1972**, *40*, 267–272.

[184] Eng, P. J.; Trainor, T. P.; Brown, G. E.; Waychunas, G. A.; Newville, M.; Sutton, S. R.; Rivers, M. L. *Science* **2000**, *288*, 1029–1033.

[185] Ebihara, K.; Takahashi, H.; Nagayama, M. *Journal of the Metal Finishing Society of Japan* **1983**, *34*, 548–553.

[186] Friedman, A.; Brittain, D.; Menon, L. *The Journal of Chemical Physics* **2007**, *127*, 154717.

[187] Ghicov, A.; Schmuki, P. *Chemical Communications* **2009**, 2791–2808.

[188] Bradhurst, D. H.; Llewelyn Leach, J. S. *Journal of The Electrochemical Society* **1966**, *113*, 1245–1249.

[189] Cherki, C.; Siejka, J. *J. Electrochem. Soc.* **1973**, *120*, 784–791.

[190] Baron-Wiechec, A.; Ganem, J. J.; Garcia-Vergara, S. J.; Skeldon, P.; Thompson, G. E.; Vickridge, I. C. *J. Electrochem. Soc* **2010**, *157*, C399–C407.

[191] Thamida, S.; Chang, H. *Chaos* **2002**, *12*, 240–251.

[192] Orvananos, B.; Malik, R.; Yu, H.; Abdellahi, A.; Grey, C. P.; Ceder, G.; Thornton, K. *Electrochim. Acta* **2014**, *137*, 245–257.

[193] Aagesen, L.; Lee, L.; Ku, P.; Thornton, K. *J. Cryst. Growth* **2012**, *361*.

[194] Aagesen, L.; Coltrin, M.; Han, J.; Thornton, K. *J. Appl. Phys.* **2015**, *117*, 194302.

[195] Wheeler, D.; Josell, D.; Moffat, T. P. *J. Electrochem. Soc.* **2003**, *150*.

[196] Yu, H.-C.; Van der Ven, A.; Thornton, K. *Metall. Mater. Trans. A* **2012**, *43*, 3481–3500.

[197] Park, C.-L.; Voorhees, P.; Thornton, K. *Comput. Mater. Sci.* **2014**, *85*, 46–58.

[198] Hofhaus, J.; Van de Velde, E. *SIAM J. Sci. Comput.* **1996**, *17*, 454–478.

[199] Osher, S.; Fedkiw, R. *Level Set Methods and Dynamics Implicit Surfaces*; Springer: New York, NY, 2003.

[200] Cermelli, P.; Fried, E.; Gurtin, M. *J. Fluid Mech.* **2005**, *554*, 339–351.

[201] Malladi, R.; Sethian, J.; Venmuri, B. *IEEE Trans. Pattern Anal. Machine Intelligence* **1995**, *17*, 158–175.

[202] Nash, G. E.; Glicksman, M. E. *Acta Metall.* **1974**,

[203] Aurbach, D.; Lu, Z.; Schechter, A.; Gofer, Y.; Gizbar, H.; Turgeman, R.; Cohen, Y.; Moshkovich, M.; Levi, E. *Nature* **2000**, *407*, 724–727.

[204] Muldoon, J.; Bucur, C. B.; Oliver, A. G.; Sugimoto, T.; Matsui, M.; Kim, H. S.; Allred, G. D.; Zajicek, J.; Kotani, Y. *Energy & Environmental Science* **2012**, *5*.

[205] Tarascon, J.; Armand, M. *Nature* **2001**,

[206] Kim, H.; Jeong, G.; Kim, Y. U.; Kim, J. H.; Park, C. M.; Sohn, H. J. *Chemical Society reviews* **2013**, *42*, 9011–9034.

[207] Mizuno, F.; Singh, N.; Arthur, T. S.; Fanson, P. T.; Ramanathan, M.; Benmayza, A.; Prakash, J.; Liu, Y.; Glans, P.; Guo, J. *Frontiers in Energy Research* **2014**,

[208] Yagi, S.; Tanaka, A.; Ichitsubo, T.; Matsubara, E. *ECS Electrochemistry Letters* **2012**, *1*.

[209] Guo, Y.; Yang, J.; Y, N.; Wang, J. **2010**,

[210] Aurbach, D.; Schechter, A.; Moshkovich, M.; Cohen, Y. *Journal of The Electrochemical Society* **2001**, *148*.

[211] Amir, N.; Vestfrid, Y.; Chusid, O.; Gofer, Y.; Aurbach, D. *Journal of Power Sources* **2007**, *174*.

[212] Ju, Q.; Shi, Y.; Kan, J. *Synthetic Metals* **2013**, *178*.

[213] NuLi, Y.; Yang, J.; Wu, R. *Electrochemistry Communications* **2005**, *7*.

[214] Jäackle, M.; Groß, A. *J. Chem. Phys.* **2014**, *141*, 174710.

[215] Ling, C.; Banerjee, D.; Matsui, M. *Electrochim. Acta* **2012**, *76*, 270.

[216] DeWitt, S.; Hahn, N.; Zavadil, K.; Thornton, K. *in preparation* **2015**,

[217] Mizrahi, O.; Amir, N.; Pollak, E.; Chusid, O.; Marks, V.; Gottlieb, H.; Larush, L.; Zinigrad, E.; Aurbach, D. *J. Electrochem. Soc.* **2008**, *155*, A103.

[218] Aagesen, L.; Lee, L.; Ku, P.; Thornton, K. *Journal of Crystal Growth* **2012**, *361*.

[219] Lee, L.; Aagesen, L.; Thornton, K.; Ku, P.-C. *Phys. Status Solidi* **2014**, *211*, 531.

[220] Frank, F. *Growth and Perfection of Crystals*; Wiley: New York, NY, 1958; p 411.

[221] Wise, S.; Lowengrub, J.; Kim, J.; Johnson, W. *Superlattices and Microstructures* **2004**, *36*, 293.

[222] Wise, S.; Lowengrub, J.; Kim, J.; Thornton, K.; Voorhees, P.; Johnson, W. *Appl. Phys. Lett.* **2005**, *87*, 133102.

[223] Eggleston, J.; Voorhees, P. *Appl. Phys. Lett.* **2002**, *80*, 306.

[224] Sun, Y.; Beckerman, C. *J. Comput. Phys.* **2006**, *230*, 626.

[225] Cahn, J. W.; Hilliard, J. E. *The Journal of Chemical Physics* **1958**, *28*, 258.

[226] Benmayza, A.; Ramanathan, M.; Arthur, T. S.; Matsui, M.; Mizuno, F.; Guo, J.; Glans, P.; Prakash, J. *The Journal of Physical Chemistry C* **2013**,

[227] Genders, J.; Pletcher, D. *Journal of Electroanalytical Chemistry and Interfacial Electrochemistry* **1986**, *199*.

[228] *CRC Handbook of Chemistry and Physics*, 95th ed.; CRC Press: Boca Raton, FL, 2014.

[229] Porter, D.; Easterling, K. *Phase Transformations in Metals and Alloys*, 2nd ed.; Chapman and Hall: London, UK, 1992.

[230] Teukolsky, S.; Vetterling, W.; Flannery, B. *Numerical Recipes: The Art of Scientific Computing*, 3rd ed.; Cambridge University Press: Cambridge, UK, 2007.

[231] Dandekar, P.; Kuvadia, Z. B.; Doherty, M. F. *Materials Research* **2013**,

[232] Enrique, R.; DeWitt, S.; Thornton, K. *in preparation* **2015**,

[233] Kazemiabnavi, K., S. Nagy; DeWitt, S.; Siegel, D.; Thornton, K. *in preparation* **2015**,

[234] Rohan, J.; Thompson, D. *Nanostructure Science and Technology: Copper Electrodeposition for Nanofabrication of Electronics Devices*; Springer: New York, NY, 2014; Vol. 171; Chapter 5, pp 99–114.

[235] Plieth, W. *Electrochemistry for Materials Science*; Elsevier: Amsterdam, The Netherlands, 2008.